

2017-01-01

# Mechanically activated magnesiothermic combustion synThesis of zirconium and hafnium diborides

Sergio Cordova

University of Texas at El Paso, scordova4@miners.utep.edu

Follow this and additional works at: [https://digitalcommons.utep.edu/open\\_etd](https://digitalcommons.utep.edu/open_etd)

 Part of the [Materials Science and Engineering Commons](#), [Mechanical Engineering Commons](#), and the [Mechanics of Materials Commons](#)

---

## Recommended Citation

Cordova, Sergio, "Mechanically activated magnesiothermic combustion synThesis of zirconium and hafnium diborides" (2017). *Open Access Theses & Dissertations*. 429.  
[https://digitalcommons.utep.edu/open\\_etd/429](https://digitalcommons.utep.edu/open_etd/429)

This is brought to you for free and open access by DigitalCommons@UTEP. It has been accepted for inclusion in Open Access Theses & Dissertations by an authorized administrator of DigitalCommons@UTEP. For more information, please contact [lweber@utep.edu](mailto:lweber@utep.edu).

MECHANICALLY ACTIVATED MAGNESIOTHERMIC COMBUSTION  
SYNTHESIS OF ZIRCONIUM AND HAFNIUM DIBORIDES

SERGIO CORDOVA

Master's Program in Mechanical Engineering

APPROVED:

---

Evgeny Shafirovich, Ph.D., Chair

---

Arturo Bronson, Ph.D.

---

Guikuan Yue, Ph.D.

---

Charles Ambler, Ph.D.  
Dean of the Graduate School

Copyright ©

by

Sergio Cordova

2017

MECHANICALLY ACTIVATED MAGNESIOTHERMIC COMBUSTION  
SYNTHESIS OF ZIRCONIUM AND HAFNIUM DIBORIDES

by

SERGIO CORDOVA, B.S.

THESIS

Presented to the Faculty of the Graduate School of

The University of Texas at El Paso

in Partial Fulfillment

of the Requirements

for the Degree of

Master of Science

Department of Mechanical Engineering

THE UNIVERSITY OF TEXAS AT EL PASO

May 2017

## Acknowledgements

First, I would like to specially thank my advisor, Dr. Evgeny Shafirovich, for giving me the opportunity to be involved in his research activities and for providing mentoring, both personally and academically.

Also, I would like to acknowledge:

- My thesis committee members for spending time to read this document.
- My teammates Alan Esparza, Armando Delgado, Arturo Catalan, Leonardo Gutierrez, and Robert Ferguson for their help.
- My family for their unconditional support.
- The National Energy Technology Laboratory of the U.S. Department of Energy for funding this research under award DE-FE0026333.

## Abstract

Magnetohydrodynamic (MHD) generation of electric power has the potential to increase the thermal efficiency of fossil-fuel burning power plants. Electrode materials in MHD generators must possess a high melting point, high electrical and thermal conductivities, chemical stability, and resistance to thermal shock, oxidation, and plasma sparks/arcs. Ultra-high temperature ceramics based on diborides of zirconium and hafnium ( $\text{ZrB}_2$  and  $\text{HfB}_2$ ) are promising materials for this application. Self-propagating high-temperature synthesis (SHS) is an attractive method for their large-scale fabrication, but SHS of  $\text{ZrB}_2$  and  $\text{HfB}_2$  from elemental Zr, Hf, and B is not economically viable because of the high cost of the raw materials. Magnesiothermic SHS from less expensive oxides  $\text{ZrO}_2$  and  $\text{B}_2\text{O}_3$  is a more attractive route, but these mixtures are difficult to ignite because of their low exothermicity. One promising approach to enabling combustion of low-exothermic mixtures is mechanical activation-assisted self-propagating high-temperature synthesis (MASHS), which involves a short-duration, high-energy milling step before the combustion process. In the present work, magnesium,  $\text{ZrO}_2$ , and  $\text{B}_2\text{O}_3$  were milled with sodium chloride (NaCl) and magnesium oxide (MgO) additives in a planetary mill, compacted into pellets, and ignited in an argon environment. The reaction mechanisms in these mixtures were studied by using thermogravimetric analysis and differential scanning calorimetry. Combustion experiments with  $\text{HfO}_2$ -based mixtures were also conducted. After the MASHS process, MgO and NaCl were removed from the products by acid leaching. The effects of excess Mg and the additives (i.e., MgO and NaCl) on the combustion characteristics and products were investigated. It has been shown that NaCl prevents loss of the mixture during milling, lowers the combustion temperature, and decreases the particle size of the products, while the excess magnesium improves the oxide-to-boride conversion.

# Table of Contents

Acknowledgements .....	iv
Abstract .....	v
Table of Contents .....	vi
List of Figures .....	viii
Chapter 1: Introduction .....	1
1.1. Electrodes of Magnetohydrodynamic (MHD) Generators .....	1
1.2. Self-Propagating High-Temperature Synthesis (SHS) .....	2
1.3. Pressureless Sintering .....	3
1.4. Objectives .....	4
Chapter 2: Literature Review on Diborides of Zirconium and Hafnium .....	6
2.1. Bonding and Crystal Structure .....	6
2.2. Fabrication of Diborides .....	7
2.2.1. Synthesis from Elements .....	7
2.2.2. Boron Carbide Reduction .....	8
2.2.3. Borothermic Reduction .....	9
2.2.4. Carbothermic Reduction .....	10
2.2.5. Metallothermic Reduction .....	10
2.2.5.1. Aluminothermic Reduction .....	11
2.2.5.2. Magnesiothermic Reduction .....	13
2.2.6. Summary of fabrication methods .....	20
Chapter 3: Experimental Procedures and Facilities .....	22
3.1. Powder Processing .....	22
3.1.1. Mixing .....	22
3.1.2. Mechanical Activation .....	23
3.2. Preparation of Pellets .....	24
3.3. Combustion Experiments .....	25
3.4. Leaching .....	26
3.5. Thermoanalytical Studies .....	26
3.6. Characterization of Materials .....	27

3.6.1. Laser Diffraction Particle Size Analysis .....	27
3.6.2. Powder X-Ray Diffraction Analysis .....	28
3.6.3. Scanning Electron Microscopy .....	29
Chapter 4: Results and Discussion.....	30
4.1. Thermodynamic Calculations .....	30
4.2. Mechanical Activation .....	41
4.2.1. Particle Size Distribution of As-received Powders.....	41
4.2.2. Effect of Milling on Composition.....	44
4.2.3. Effect of Magnesium Oxide.....	45
4.2.4. Effect of Sodium Chloride .....	47
4.3. Combustion Experiments.....	49
4.3.1. Magnesiothermic MASHS of Zirconium Diboride .....	49
4.3.1.1. Effect of Magnesium Oxide.....	52
4.3.1.2. Effect of Sodium Chloride .....	55
4.3.1.3. Effect of Excess Magnesium .....	60
4.3.1.4. Effect of Leaching on the Products.....	62
4.3.2. Magnesiothermic MASHS of Hafnium Diboride .....	65
4.3.3. Magnesiothermic MASHS of Zirconium Diboride and Hafnium Diboride Composites.....	66
4.4. Reaction Mechanisms .....	67
Chapter 5: Conclusions .....	71
References.....	73

Vita 78



## List of Figures

Figure 1.2.1: Self-propagating high-temperature synthesis.....	2
Figure 2.1.1: Crystal structure of group-IV transition metals diborides (Hexagonal $P6/mmm$ $AlB_2$ ) [8].....	6
Figure 2.2.1: XRD pattern of the products obtained by boron carbide reduction of $ZrO_2$ in the stoichiometric (2:1:3 molar ratio) $ZrO_2/B_4C/C$ mixture [39]. ....	9
Figure 2.2.2: XRD patterns of $ZrB_2-Al_2O_3$ , $HfB_2-Al_2O_3$ , and $(Zr_{0.5}Hf_{0.5})B_2-Al_2O_3$ composites obtained by aluminothermic MSR. Note: the identification letters Z, ZH, and H correspond to $ZrB_2-Al_2O_3$ , $(Zr_{0.5}Hf_{0.5})B_2-Al_2O_3$ , and $HfB_2-Al_2O_3$ composites, respectively [50] .....	12
Figure 2.2.3: XRD patterns obtained by magnesiothermic mechanical alloying of $ZrB_2$ at different milling times, after heating, and after leaching [51]. ....	14
Figure 2.2.4: XRD patterns of the products obtained by magnesiothermic MSR of $ZrB_2$ . The figure show the patterns of the initial mixture, after ignition (6 min), after the mechanical alloying step (3 hours), and after leaching [19] .....	15
Figure 2.2.5: DSC curve of stoichiometric unmilled stoichiometric $ZrO_2/B_2O_3/Mg$ mixture [47]. ....	16
Figure 2.2.6: XRD patterns obtained by magnesiothermic VCS of $ZrB_2$ . The figure shows the patterns of the mixture obtained by VCS (a), the leached mixture after VCS (b), and the leached mixture after the second VCS step (c) [20]. ....	18
Figure 2.2.7: DSC curve of milled stoichiometric $ZrO_2/B_2O_3/Mg$ mixture [55].....	19
Figure 3.1.2: Milling equipment: (a) planetary mill (Fritsch Pulverisette 7 Premium Line) and (b) grinding bowl with purging valves. ....	24
Figure 3.2.1: Pressing equipment: (a) die set and (b) uniaxial hydraulic press.....	25
Figure 3.5.1: Thermoanalytical instruments: (a) Netzsch DSC 404 F1 Pegasus and (b) Netzsch TGA 209 F1 Iris.....	27
Figure 3.6.1: Particle size analyzer (Microtrac Bluewave).....	28
Figure 3.6.2: X-ray diffractometer (Bruker D8 Discover XRD). ....	28
Figure 3.6.3: Scanning electron microscope (SEM, Hitachi S-4800).....	29
Figure 4.1.1: Adiabatic flame temperature and equilibrium product composition vs NaCl concentration in $ZrO_2-B_2O_3-Mg-NaCl$ system. $B_nO_m$ and $Na_nCl$ are used for gas mixtures $B_2O_3/B_2O_2/BO$ and $NaCl/Na_2Cl_2/Na_3Cl_3$ , respectively. ....	31
Figure 4.1.2: Adiabatic flame temperature and equilibrium product composition vs NaCl concentration in $HfO_2-B_2O_3-Mg-NaCl$ system. $B_nO_m$ and $Na_nCl$ are used for gas mixtures $B_2O_3/B_2O_2/BO$ and $NaCl/Na_2Cl_2/Na_3Cl_3$ , respectively. ....	32
Figure 4.1.3: Adiabatic flame temperature and conversion of $ZrO_2$ to $ZrB_2$ (or $HfO_2$ to $HfB_2$ ) vs Mg concentration in $ZrO_2-B_2O_3-Mg$ (or $HfO_2-B_2O_3-Mg$ ) system. ....	33
Figure 4.1.4: Adiabatic flame temperature and equilibrium product composition vs NaCl concentration in $ZrO_2-B_2O_3-Mg-NaCl$ system. $B_nO_m$ and $Na_nCl$ are used for gas mixtures $B_2O_3/B_2O_2/BO$ and $NaCl/Na_2Cl_2/Na_3Cl_3$ , respectively. ....	35
Figure 4.1.5: Adiabatic flame temperature and equilibrium product composition vs NaCl concentration in $HfO_2-B_2O_3-Mg-NaCl$ system. $B_nO_m$ and $Na_nCl$ are used for gas mixtures $B_2O_3/B_2O_2/BO$ and $NaCl/Na_2Cl_2/Na_3Cl_3$ , respectively. ....	36
Figure 4.1.6: Adiabatic flame temperature and percent conversion of $ZrO_2$ to $ZrB_2$ (or $HfO_2$ to $HfB_2$ ) vs NaCl concentration in $ZrO_2-B_2O_3-Mg-NaCl$ (or $HfO_2-B_2O_3-Mg-NaCl$ ) system.....	37

Figure 4.1.7: Adiabatic flame temperature and equilibrium product composition vs MgO concentration in $\text{ZrO}_2\text{--B}_2\text{O}_3\text{--Mg--MgO}$ system. $\text{B}_n\text{O}_m$ is used for a mixture of $\text{B}_2\text{O}_3/\text{B}_2\text{O}_2/\text{BO}$ gases. ....	38
Figure 4.1.8: Adiabatic flame temperature and equilibrium product composition vs MgO concentration in $\text{HfO}_2\text{--B}_2\text{O}_3\text{--Mg--MgO}$ system. $\text{B}_n\text{O}_m$ is used for a mixture of $\text{B}_2\text{O}_3/\text{B}_2\text{O}_2/\text{BO}$ gases. ....	39
Figure 4.1.9: Adiabatic flame temperature and percent conversion of $\text{ZrO}_2$ to $\text{ZrB}_2$ (or $\text{HfO}_2$ to $\text{HfB}_2$ ) vs Mg concentration in $\text{ZrO}_2\text{--B}_2\text{O}_3\text{--Mg--MgO}$ (or $\text{HfO}_2\text{--B}_2\text{O}_3\text{--Mg--MgO}$ ) system. ....	40
Figure 4.2.1: Particle size distribution of zirconium (IV) oxide ( $\text{ZrO}_2$ , -325 mesh, 99.7% pure, Alfa Aesar). ....	42
Figure 4.2.2: Particle size distribution of boron trioxide ( $\text{B}_2\text{O}_3$ , 99.8% pure, Sigma-Aldrich). ....	42
Figure 4.2.3: Particle size distribution of magnesium (Mg, -325 mesh, 99.8% pure, Sigma-Aldrich). ....	43
Figure 4.2.4: Particle size distribution of magnesium oxide ( $\text{MgO}$ , -325 mesh, $\geq 99\%$ pure, Sigma-Aldrich). ....	43
Figure 4.2.5: Particle size distribution of sodium chloride ( $\text{NaCl}$ , 99% pure, Sigma-Aldrich). ....	44
Figure 4.2.6: XRD patterns of stoichiometric $\text{ZrO}_2\text{--B}_2\text{O}_3\text{--Mg}$ mixture (a) before milling and (b) after milling for 1 minute. ....	45
Figure 4.2.7: Percentage of mixture that is lost to the grinding media vs. MgO concentration. ..	46
Figure 4.2.8: Particle size distribution of $\text{ZrO}_2/\text{B}_2\text{O}_3/\text{Mg}$ mixture with 40wt% MgO after milling for 1 min. ....	46
Figure 4.2.9: Particle size distribution of $\text{ZrO}_2/\text{B}_2\text{O}_3/\text{Mg}$ mixture with 40wt% MgO after milling for 10 min. ....	47
Figure 4.2.10: Percentage of stoichiometric $\text{ZrO}_2/\text{B}_2\text{O}_3/\text{Mg}$ mixture that is lost to the grinding media vs. NaCl concentration. ....	48
Figure 4.2.11: Particle size distribution of $\text{ZrO}_2/\text{B}_2\text{O}_3/\text{Mg}$ mixture with 40wt% NaCl after milling for 1 min. ....	48
Figure 4.2.12: Particle size distribution of $\text{ZrO}_2/\text{B}_2\text{O}_3/\text{Mg}$ mixture with 40wt% NaCl after milling for 1 min. ....	49
Figure 4.3.1: Combustion propagation over a pellet of stoichiometric $\text{ZrO}_2\text{--B}_2\text{O}_3\text{--Mg}$ mixture. Time zero was selected 4 s before the end of the combustion process. ....	50
Figure 4.3.2: Thermocouple recording for stoichiometric $\text{ZrO}_2/\text{B}_2\text{O}_3/\text{Mg}$ mixture. Time zero was selected arbitrarily. ....	50
Figure 4.3.3: XRD patterns of stoichiometric $\text{ZrO}_2/\text{B}_2\text{O}_3/\text{Mg}$ mixture (a) after milling for 1 min, (b) after combustion, and (c) after leaching. ....	51
Figure 4.3.4: Combustion propagation over a pellet of stoichiometric $\text{ZrO}_2/\text{B}_2\text{O}_3/\text{Mg/MgO}$ mixtures. The top images are for 30 wt% MgO and 1 min milling, the bottom images are for 40 wt% MgO and 10 min milling. Time zero was selected 4 s before the end of the combustion process. ....	52
Figure 4.3.5: XRD patterns of stoichiometric $\text{ZrO}_2/\text{B}_2\text{O}_3/\text{Mg}$ mixture with 40wt% MgO (a) after milling for 10 min, (b) after combustion, and (c) after leaching. ....	54
Figure 4.3.6: Intensity ratios of the m- $\text{ZrO}_2$ and c- $\text{ZrO}_2$ XRD peaks (planes (111) and (111)) to the $\text{ZrB}_2$ peak (plane 101) vs. MgO concentration in the initial mixture with the stoichiometric ( $\text{ZrO}_2:\text{B}_2\text{O}_3:\text{Mg} = 1:1:5$ ) composition. ....	55
Figure 4.3.7: Combustion propagation over a pellet of stoichiometric $\text{ZrO}_2/\text{B}_2\text{O}_3/\text{Mg/NaCl}$ mixture with 47wt% NaCl. Time zero was selected arbitrarily. ....	56

Figure 4.3.8: Thermocouples recordings for stoichiometric $\text{ZrO}_2/\text{B}_2\text{O}_3/\text{Mg}/\text{NaCl}$ mixture with 47 wt% NaCl. Time zero was selected arbitrarily. ....	57
Figure 4.3.9: Combustion front velocity vs. NaCl concentration in the initial mixture. ....	57
Figure 4.3.10: XRD pattern of stoichiometric $\text{ZrO}_2/\text{B}_2\text{O}_3/\text{Mg}$ mixture with 40wt% NaCl after combustion. ....	58
Figure 4.3.11: Intensity ratios of the m- $\text{ZrO}_2$ and c- $\text{ZrO}_2$ XRD peaks (planes (111) and (111)) to the $\text{ZrB}_2$ peak (plane 101) and maximum recorded temperature vs. NaCl concentration in the initial mixture with the stoichiometric ( $\text{ZrO}_2:\text{B}_2\text{O}_3:\text{Mg} = 1:1:5$ ) composition. ....	59
Figure 4.3.12: Scanning electron microscopy images of the leached combustion products of stoichiometric $\text{ZrO}_2/\text{B}_2\text{O}_3/\text{Mg}$ mixture (a) with no NaCl and (b) with 30 wt% NaCl. ....	60
Figure 4.3.13: Intensity ratios of the m- $\text{ZrO}_2$ and c- $\text{ZrO}_2$ XRD peaks (planes (111) and (111)) to the $\text{ZrB}_2$ peak (plane 101) and maximum recorded temperature vs. NaCl concentration in the initial mixture with the $\text{ZrO}_2:\text{B}_2\text{O}_3:\text{Mg} = 1:1:5$ and $\text{ZrO}_2:\text{B}_2\text{O}_3:\text{Mg} = 1:1:6$ compositions. ....	61
Figure 4.3.14: Scanning electron microscopy images of the combustion products of stoichiometric $\text{ZrO}_2/\text{B}_2\text{O}_3/\text{Mg}$ mixture with 20% excess Mg and 30 wt% NaCl. ....	62
Figure 4.3.15: XRD pattern of stoichiometric $\text{ZrO}_2/\text{B}_2\text{O}_3/\text{Mg}$ mixture with 30wt% NaCl after leaching. ....	63
Figure 4.3.16: Intensity ratios of the m- $\text{ZrO}_2$ and c- $\text{ZrO}_2$ XRD peaks (planes (111) and (111)) to the $\text{ZrB}_2$ peak (plane 101) and maximum recorded temperature vs. NaCl concentration in the initial mixture with the stoichiometric ( $\text{ZrO}_2:\text{B}_2\text{O}_3:\text{Mg} = 1:1:5$ ) composition, before and after leaching. ....	64
Figure 4.3.17: Intensity ratios of the m- $\text{ZrO}_2$ and c- $\text{ZrO}_2$ XRD peaks (planes (111) and (111)) to the $\text{ZrB}_2$ peak (plane 101) and maximum recorded temperature vs. NaCl concentration in the initial mixture with the $\text{ZrO}_2:\text{B}_2\text{O}_3:\text{Mg} = 1:1:6$ composition, before and after leaching. ....	65
Figure 4.3.18: XRD pattern of stoichiometric $\text{HfO}_2/\text{B}_2\text{O}_3/\text{Mg}$ mixture with 30 wt% NaCl after combustion. ....	66
Figure 4.3.19: XRD pattern of $\text{ZrO}_2/\text{HfO}_2/\text{B}_2\text{O}_3/\text{Mg}$ mixture with 30 wt% NaCl after combustion. ....	67
Figure 4.4.1: DSC and TG curves of stoichiometric $\text{ZrO}_2\text{-B}_2\text{O}_3\text{-Mg}$ . ....	68
Figure 4.4.2: DSC and TG curves of stoichiometric $\text{ZrO}_2\text{-B}_2\text{O}_3\text{-Mg}$ with 45 wt% NaCl. ....	69
Figure 4.4.3: XRD patterns of the milled mixture and of the products obtained after quenching the DSC test of $\text{ZrO}_2\text{-B}_2\text{O}_3\text{-Mg}$ with 45 wt% of NaCl at different temperatures. ....	70

# Chapter 1: Introduction

## 1.1. Electrodes of Magnetohydrodynamic (MHD) Generators

Direct power extraction (DPE) *via* magnetohydrodynamic (MHD) generation is of great interest because of potentially high thermal efficiency. In conventional power-generating cycles, a gas turbine converts the enthalpy of a high-temperature gas into mechanical energy, which is then converted to electrical energy in a generator. In MHD generators, high-temperature, electrically conductive gas (plasma) flows through a magnetic field, generating electricity, i.e. the enthalpy of the gas is directly converted into electrical energy [1]. Another advantage of MHD generators is higher operating temperatures than in gas turbines. In gas turbines, the maximum operating temperature is limited by the mechanical strength of the material at high temperatures (around 1200 °C), but in MHD generators the maximum temperature is constrained by the compatibility of electrodes with high temperature and high heat flux environments [1] [2]. However, R&D of MHD generators have encountered many challenges. One of them is the lack of materials for MHD electrodes.

Fully functional electrodes in MHD channels should possess a sufficiently high electrical conductivity and provide smooth transfer of electric current to and from the plasma. Also, they require an adequate thermal conductivity and should be thermally stable under operating conditions. In addition, they should withstand a thermal shock, recognized as a significant problem during previous R&D in the area of MHD generators [3] [4]. Zirconium diboride ( $\text{ZrB}_2$ ) and hafnium diboride ( $\text{HfB}_2$ ) are promising ceramic materials for ultra-high temperature applications such as thermal protection of spacecraft/hypersonics and MHD electrodes [5] [6] because of their high melting points (over 3200 °C), chemical stability, high electrical and thermal conductivities, and high oxidation resistance [7] [8]. Unfortunately, the current fabrication methods of  $\text{ZrB}_2$  and  $\text{HfB}_2$  are complex, energy-consuming, and expensive.

## 1.2. Self-Propagating High-Temperature Synthesis (SHS)

Self-propagating high-temperature synthesis (SHS) is a promising approach for the fabrication of advanced intermetallics and ceramics [9] [10] [11] [12]. This method takes advantage of the energy release of high-exothermic mixtures to synthesize materials with a low-energy input. Other advantages of SHS are simple equipment, high purity of products, and tailored microstructure [11] [12] [13]. Figure 1.2.1 shows the process of SHS. In the first stage, the initial mixture is ignited locally by an external energy source, in this case a hot wire. Then the combustion front propagates along the pellet forming a new product. In the last stage, the final product cools down to room temperature.

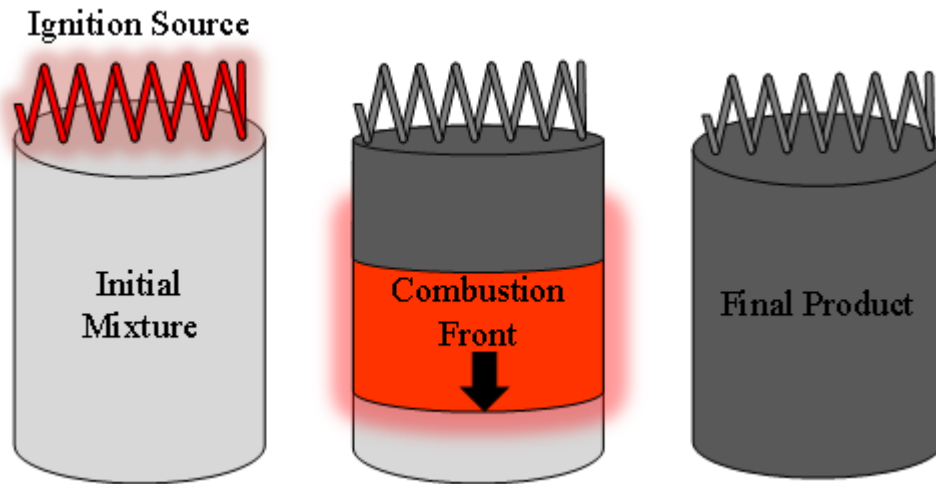


Figure 1.2.1: Self-propagating high-temperature synthesis.

SHS of  $\text{ZrB}_2$  and  $\text{HfB}_2$  from elemental Zr, Hf, and B has been conducted as long as decades ago [14]. More recently, the addition of NaCl to Zr and B has enabled the fabrication of nanoscale  $\text{ZrB}_2$  powder by SHS [15]. However, SHS from elements is not considered for commercial production because of the high cost of zirconium, hafnium, and boron [16].

A more economical route is metallothermic reduction of  $\text{ZrO}_2$  and  $\text{B}_2\text{O}_3$  using magnesium (Mg) as the reduction agent. To yield pure  $\text{ZrB}_2$  by this process, the combustion byproduct  $\text{MgO}$  can be leached in diluted  $\text{HCl}$ . Magnesiothermic reduction can be conducted in the SHS mode, but incomplete conversion of  $\text{ZrO}_2$  and  $\text{B}_2\text{O}_3$  (or  $\text{H}_3\text{BO}_3$ ) to  $\text{ZrB}_2$  is a major problem [17] [18] [19]. To increase the conversion, a mixture of Mg,  $\text{ZrO}_2$ , and  $\text{H}_3\text{BO}_3$  was ignited inside a furnace; next, the combustion products were mixed with additional amounts of Mg and  $\text{H}_3\text{BO}_3$  and ignited again [20]. The conversion increased (though not to 100%), but the method involved two combustion processes and two mixing procedures, which increased complexity.

Another problem with magnesiothermic SHS of  $\text{ZrB}_2$  is related to the low exothermicity of the initial mixture, which makes the ignition difficult. This problem can be overcome using mechanical activation, i.e. a short-duration, high-energy ball milling step before the combustion process [21] [22] [23]. If milling is long, it can even initiate combustion. Recently,  $\text{ZrB}_2$  was obtained from oxides by a mechanically induced self-sustained magnesiothermic reduction [19]. However, it is difficult to scale-up the combustion process inside the milling vial and to ensure safety of this process. It appears to be more practical to conduct only short-duration milling, which facilitates ignition in a subsequent SHS process (the so-called mechanical activation-assisted SHS, or MASHS).

### **1.3. Pressureless Sintering**

Usually, SHS products are porous and fragile. To fabricate useful structural materials, the SHS products should be densified. Because of the strong covalent bonding and the presence of  $\text{ZrO}_2$  and  $\text{B}_2\text{O}_3$  oxide layer, pure  $\text{ZrB}_2$  and  $\text{HfB}_2$  are usually densified by hot pressing at 2100-2300 °C [24]. By using sintering additives the hot-pressing temperature can be significantly reduced [25] [26] [27]. Another method is spark plasma sintering (SPS), where densification can be conducted at a lower temperature and the product is often denser than in hot pressing [25] [27] [28]. However, in both methods only simple geometries can be obtained.

One approach to manufacturing complex geometries is pressureless sintering (PS), but, as mentioned above, sintering of  $\text{ZrB}_2$  and  $\text{HfB}_2$  requires rather high temperatures and pressures. Reducing the particle size and the total oxygen content enhances the sintering of  $\text{ZrB}_2$  [29] [8] [16]. A promising method for the pressureless sintering of  $\text{ZrB}_2$  and  $\text{HfB}_2$  is the addition of reducing agents. The additives reduced the oxide ( $\text{ZrO}_2$ ) layer on  $\text{ZrB}_2$ , enabling sintering at lower temperatures and to higher densities. Some of the additives that have been studied are  $\text{SiC}$ ,  $\text{MoSi}_2$ ,  $\text{B}_4\text{C}$ ,  $\text{B}$ ,  $\text{C}$ ,  $\text{Fe}$ , and  $\text{Cr}$  [28] [30] [31] [32]. SHS products usually contain a high defect concentration, which improves sintering [16]. Furthermore, it has been demonstrated that by conducting SHS of  $\text{ZrB}_2$  with  $\text{NaCl}$  as an inert diluent, the particle size of the products is drastically reduced [15] [33].

#### 1.4. Objectives

The overarching goal of the present work is to develop a method for low-cost manufacturing of zirconium and hafnium diborides that possess all the required properties needed to function as sustainable MHD electrodes. More specifically, the work is focused on the determination of optimal conditions for mechanical activation-assisted magnesiothermic combustion synthesis of  $\text{ZrB}_2$  and  $\text{HfB}_2$  from relatively inexpensive oxides of  $\text{Zr}$ ,  $\text{Hf}$ , and  $\text{B}$ . Note that sintering of the obtained products is beyond the scope of the present work.

A major problem in the magnesiothermic SHS of  $\text{ZrB}_2$  and  $\text{HfB}_2$  is the loss of magnesium during combustion due to a higher the combustion temperature than the boiling point of  $\text{Mg}$ , which leads to incomplete conversion. The objective of the present work is to investigate the possibility of improving the conversion by adding extra  $\text{Mg}$  or inert compounds  $\text{NaCl}$  and  $\text{MgO}$ , which decrease the combustion temperature. However,  $\text{ZrO}_2/\text{B}_2\text{O}_3/\text{Mg}$  and  $\text{HfO}_2/\text{B}_2\text{O}_3/\text{Mg}$  mixtures with additives are less exothermic and mechanical activation is required to ignite them. The  $\text{NaCl}$  and  $\text{MgO}$  additives help activate (mill) the mixtures with high contents of  $\text{Mg}$ , i.e. they may play a dual role in the entire MASHS procedure. In addition, sodium chloride may decrease the product

particle size [15] [34], which leads to better properties. After combustion, both additives can be easily separated from the products – MgO by acid leaching and NaCl by dissolution in water.

The list below describes the steps that were followed to study the effects of adding NaCl, MgO, and extra Mg on the conversion of oxides to borides.

1. A thermodynamic analysis of the combustion process was conducted for  $\text{ZrO}_2/\text{B}_2\text{O}_3/\text{Mg}$  and  $\text{HfO}_2/\text{B}_2\text{O}_3/\text{Mg}$  mixtures with each of the three additives.
2. The milling parameters were optimized to facilitate the ignition of mixtures at various compositions.
3. The effect of MgO and NaCl on the milling process was studied.
4. Combustion experiments were conducted at various MgO, NaCl, and Mg concentrations in the mixtures.
5. The effects of additives on conversion were studied using X-ray diffraction analysis.



## Chapter 2: Literature Review on Diborides of Zirconium and Hafnium

The objective of this chapter is to present and discuss the published literature on diborides of zirconium and hafnium. The first section will discuss the types of chemical bonding that form the diborides of group-IV metals. In the second section, the synthesis methods of  $\text{ZrB}_2$  and  $\text{HfB}_2$  will be extensively explored, including the advantages and disadvantages of the different fabrication methods.

### 2.1. Bonding and Crystal Structure

Atomic bonding in diborides of group-IV transition metals is divided in three categories based on the crystal structure; the first is metal-boron covalent bonds, the second is the boron-boron covalent bonds, and the third is metal-metal metallic bonds. In the crystal structure, the atoms are arranged in a hexagonal  $P6/mmm$  structure of the type  $\text{AlB}_2$  [8] [35] [36]. Figure 2.1.1 illustrates the projection of the  $\text{AlB}_2$  structure. It is observed that the hexagonal structure is ordered in alternating layers of closed packed metal and boron atoms.

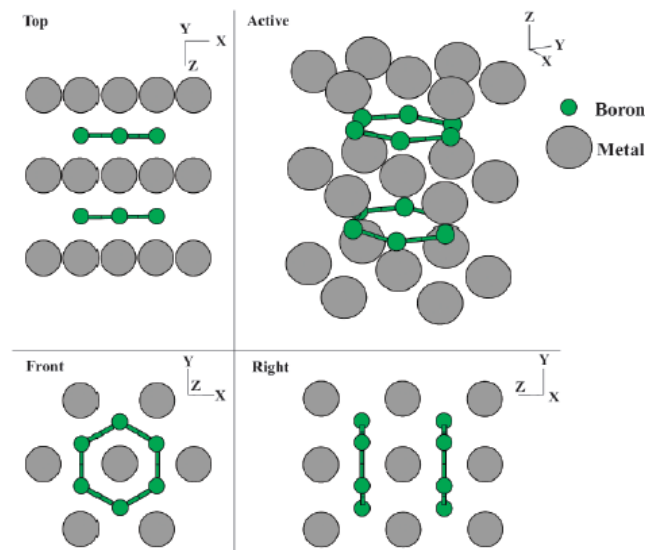


Figure 2.1.1: Crystal structure of group-IV transition metals diborides (Hexagonal  $P6/mmm$   $\text{AlB}_2$ ) [8].

The bonding and crystal structure in zirconium and hafnium diborides provide a unique combination of properties such as high melting temperature, chemical stability, high thermal conductivity, and low electrical resistivity. The chemical stability and high melting temperature are associated with the boron-boron and metal-boron covalent bonds [37]. Metallic bonding in the structure is the cause for high electrical and thermal conductivities [38].

## 2.2. Fabrication of Diborides

Diborides of group-IV metals can be fabricated by various approaches. In the present section, the available literature on the fabrication of  $\text{ZrB}_2$  and  $\text{HfB}_2$  will be discussed. The first subsection includes a discussion of combustion synthesis of  $\text{ZrB}_2$  and  $\text{HfB}_2$  from elemental powders. The following subsections will present three reduction processes for the fabrication of  $\text{ZrB}_2$  (boron carbide, borothermic, and carbothermic reductions). Finally, the last subsection will present the available literature on synthesis of zirconium and hafnium diborides with a metallothermic step.

### 2.2.1. Synthesis from Elements

Self-propagating high-temperature synthesis (SHS) of diborides of zirconium and hafnium from elements (Zr, Hf, and B) was demonstrated decades ago by Borovinskaya et al. [14]. The elemental powders react according to the following reactions:



In [6], the combustion characteristics of these systems were extensively studied. It was found that the wave front velocity of Zr-B system initially increases with an increase in the pellet diameter to then reach a constant value.

More recently, Çamurlu and Maglia fabricated nanoscale ZrB<sub>2</sub> powder by elemental SHS with NaCl as an inert diluent [15]. The NaCl content was varied from 10 to 50 wt%. The optimal NaCl concentration was determined to be 30 wt% NaCl; at that concentration, the obtained particle size was 200 nm.

### 2.2.2. Boron Carbide Reduction

Boron carbide reduction of ZrO<sub>2</sub> to fabricate ZrB<sub>2</sub> is an endothermic process. The chemical reaction route is:



Soner et al. fabricated ZrB<sub>2</sub> following the above chemical equation [39]. The initial ZrO<sub>2</sub>, B<sub>4</sub>C, and C powders were mixed and compacted into pellets. The synthesis was carried out in an induction furnace at temperatures varied from 1200 °C to 1875 °C for 2 hours. Figure 2.2.1 shows the XRD pattern of the products obtained during thermogravimetric analysis (TGA) of the stoichiometric (2:1:3 molar ratio) ZrO<sub>2</sub>/B<sub>4</sub>C/C mixture. It is seen that ZrB<sub>2</sub> is the main phase, but ZrB, graphite, and ZrO<sub>2</sub> are present as impurities. The authors concluded that the stoichiometry was disproportioned by boron loss in the form of B<sub>2</sub>O<sub>3</sub> leading to incomplete conversion. This was confirmed by thermodynamic calculations. To compensate the boron lost, the authors readjusted the mixture proportion (2:1.1:2.7 mole ratio), leading to the synthesis of pure ZrB<sub>2</sub>.

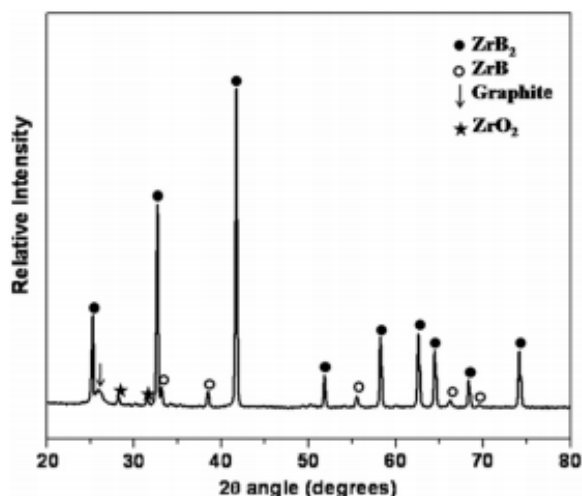


Figure 2.2.1: XRD pattern of the products obtained by boron carbide reduction of  $\text{ZrO}_2$  in the stoichiometric (2:1:3 molar ratio)  $\text{ZrO}_2/\text{B}_4\text{C}/\text{C}$  mixture [39].

### 2.2.3. Borothermic Reduction

Another approach to fabricate diborides of group-IV metals is the reduction of oxides by boron. The chemical reaction route to fabricate  $\text{ZrB}_2$  by borothermic reduction is shown by the following equation:



Millet and Hwang fabricated  $\text{ZrB}_2$  and  $\text{TiB}_2$  by mechanically activated borothermic reduction of oxides [40]. In this study, zirconium oxide and boron were mixed at the proportion  $\text{ZrO}_2:\text{B} = 1:4$  and milled for 70 hours. After milling, the mixture was heated in a DTA up to  $1100^\circ\text{C}$ .  $\text{ZrB}_2$  was obtained as the main product with c- $\text{ZrO}_2$  and m- $\text{ZrO}_2$  impurities.

#### 2.2.4. Carbothermic Reduction

Zirconium diboride has been fabricated by carbothermic reduction of oxides of zirconium and boron [41]. The powders were ball-milled in the proportion described by the following equation:



After milling, the mixture was heated in a furnace at 1800 °C for 1 hour. The XRD pattern of the products shows that  $\text{ZrB}_2$  is formed, but  $\text{ZrO}_2$  is present as an impurity. One possible explanation of the incomplete conversion could be vaporization of  $\text{B}_2\text{O}_3$  due to its high vapor pressure at the process temperature.

#### 2.2.5. Metallothermic Reduction

Many materials (including BN, W, TiC, WC,  $\text{B}_4\text{C}$ , and Mo) can be fabricated by combustion synthesis with metallothermic reduction of oxides or salts [42] [43] [44] [45] [46]. Some of the metallic reducing agents that have been previously used are Zn, Al, and Mg. Borides of group-IV metals have been previously obtained by metallothermic reduction. In the present subsection, metallothermic combustion synthesis of diborides will be discussed.

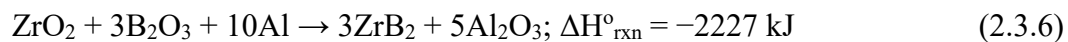
In the metallothermic reduction route for the synthesis of diborides of zirconium and hafnium, oxides of zirconium and hafnium ( $\text{ZrO}_2$  and  $\text{HfO}_2$ ) are usually used as the sources of zirconium and hafnium, respectively, but also zircon ( $\text{ZrSiO}_4$ ) is utilized [47]. For the boron source, four different compounds have been tested: boron oxide ( $\text{B}_2\text{O}_3$ ), boric acid ( $\text{H}_3\text{BO}_3$ ), metaboric acid ( $\text{HBO}_2$ ), and borax ( $\text{Na}_2\text{B}_4\text{O}_7$ ). In the articles that are discussed in this section, two metallic reduction agents are used: aluminum and magnesium. It is important to note that aluminum oxide ( $\text{Al}_2\text{O}_3$ ), which is a product of aluminothermic reduction, is not removable from the final products. In contrast, magnesium oxide ( $\text{MgO}$ ) can be removed by mild acid leaching,

leading to synthesis of pure ZrB<sub>2</sub>. Aluminothermic and magnesiothermic reduction routes will be individually discussed in the following subsections.

#### 2.2.5.1. Aluminothermic Reduction

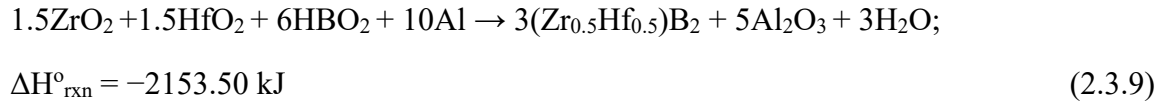
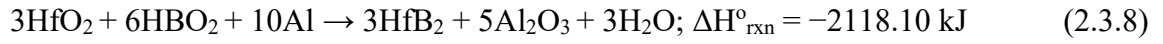
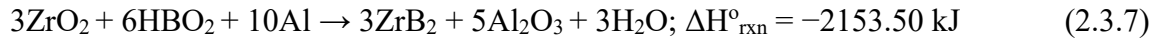
In this approach for metallothermic reduction, the fabrication of ZrB<sub>2</sub>-Al<sub>2</sub>O<sub>3</sub> and HfB<sub>2</sub>-Al<sub>2</sub>O<sub>3</sub> composites by aluminothermic reduction of oxides and acids will be discussed.

Abbasi et al. studied aluminothermic, mechanical activation-assisted SHS (MASHS) of ZrB<sub>2</sub>-Al<sub>2</sub>O<sub>3</sub> composites [48]. In this study, ZrO<sub>2</sub> and B<sub>2</sub>O<sub>3</sub> were used as the sources of Zr and B, respectively. Therefore, the theoretical full combustion reaction is described by:



The initial powder mixture was mechanically activated in a planetary ball mill using steel grinding media. The milled mixtures were compacted into cylindrical pellets. The pellet was ignited inside a reacting chamber using an electrically heated tungsten wire. The results showed that no reaction occurred during milling, but atomic absorption spectroscopy of the milled mixtures showed iron (Fe) contamination. XRD of the products showed that the two major phases obtained were Al<sub>2</sub>O<sub>3</sub> and ZrB<sub>2</sub>, though ZrO<sub>2</sub> was present as a contaminant.

Deris et al. studied the effect of milling on aluminothermic MASHS of ZrB<sub>2</sub>-Al<sub>2</sub>O<sub>3</sub> composites using differential scanning calorimetry (DSC) [49]. The DSC curves showed that milling decreased the ignition temperature from 1.112 °C to 643 °C, which is below the melting point of Al (660 °C). Sayagués et al. produced ZrB<sub>2</sub>-Al<sub>2</sub>O<sub>3</sub>, HfB<sub>2</sub>-Al<sub>2</sub>O<sub>3</sub>, and solid solution (Zr<sub>0.5</sub>Hf<sub>0.5</sub>)B<sub>2</sub>-Al<sub>2</sub>O<sub>3</sub> composites by aluminothermic mechanically-induced self-sustained reaction (MSR) process [50]. In this study, HBO<sub>2</sub> was used as the boron source and the exothermic chemical reactions were described by the following equations:



The XRD results shown in Fig. 2.2.2 show small traces of oxides in the products. Also, it is shown that a single-phase solid solution of the two diborides  $(\text{Zr}_{0.5}\text{Hf}_{0.5})\text{B}_2$  was synthesized.

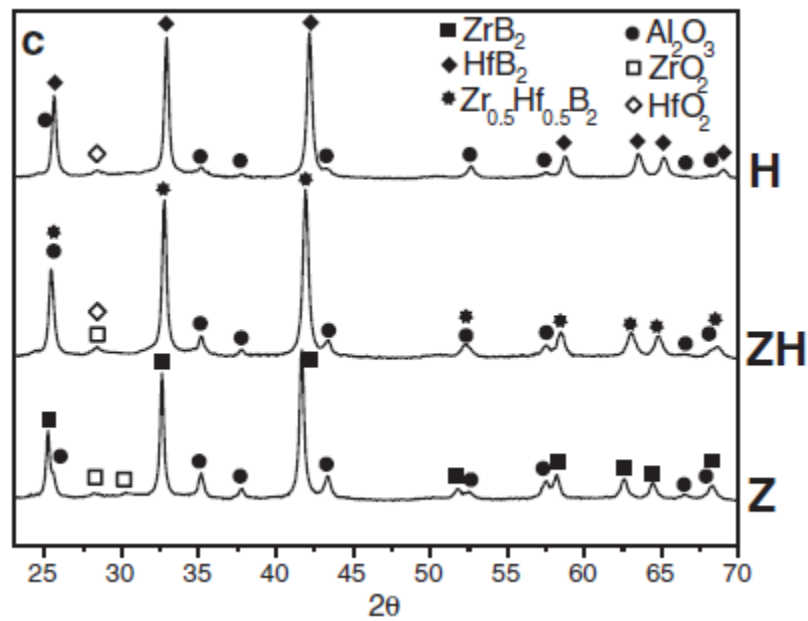


Figure 2.2.2: XRD patterns of  $\text{ZrB}_2\text{-Al}_2\text{O}_3$ ,  $\text{HfB}_2\text{-Al}_2\text{O}_3$ , and  $(\text{Zr}_{0.5}\text{Hf}_{0.5})\text{B}_2\text{-Al}_2\text{O}_3$  composites obtained by aluminothermic MSR. Note: the identification letters Z, ZH, and H correspond to  $\text{ZrB}_2\text{-Al}_2\text{O}_3$ ,  $(\text{Zr}_{0.5}\text{Hf}_{0.5})\text{B}_2\text{-Al}_2\text{O}_3$ , and  $\text{HfB}_2\text{-Al}_2\text{O}_3$  composites, respectively [50].

#### 2.2.5.2. Magnesiothermic Reduction

The relatively easy removal of MgO by mild acid leaching makes magnesiothermic reduction more attractive than aluminothermic reduction. For this reason, magnesiothermic reduction has been studied extensively. This review of metallothermic reduction includes the literature on different pathways for fabricating  $\text{ZrB}_2$  with a magnesiothermic step. Note that magnesiothermic-based approaches to fabrication of  $\text{HfB}_2$  were not found in the literature.

Setoudeh and Welham studied the synthesis of  $\text{ZrB}_2$  by mechanically alloying  $\text{ZrO}_2/\text{B}_2\text{O}_3/5\text{Mg}$  powder mixture in a ball mill [51]. Steel balls were used (diameter: 25.4 mm, the balls-mixture mass ratio: 43:1). The mixture was milled at 165 rpm for 15 hours in an argon atmosphere. After mechanical alloying, the mixture was heated at 1200 °C. Figure 2.2.3 shows the XRD pattern of the mixture after milling for different times (2, 8, and 12 hours), after heating to 1200 °C, and after leaching. It is seen that after milling for 2 hours,  $\text{ZrO}_2$  is transformed into a high-temperature tetragonal phase, caused by a smaller crystallite size after milling, and a small amount of  $\text{ZrB}_2$  starts to appear. At 8 and 15 hours, the amount of  $\text{ZrB}_2$  becomes the most prominent phase. After heating, the t- $\text{ZrO}_2$  is further reduced, but there is not much difference. The authors indicate that exothermic reactions occurred during milling, but the temperature rise inside the milling bowl was only 3 °C, indicating that the reaction was not a combustion process. It is recommended that the addition of excess  $\text{B}_2\text{O}_3$  and Mg may aid in achieving full reduction of  $\text{ZrO}_2$ . The authors did not study the contamination caused by the iron grinding media, which was shown to occur in another study [48].



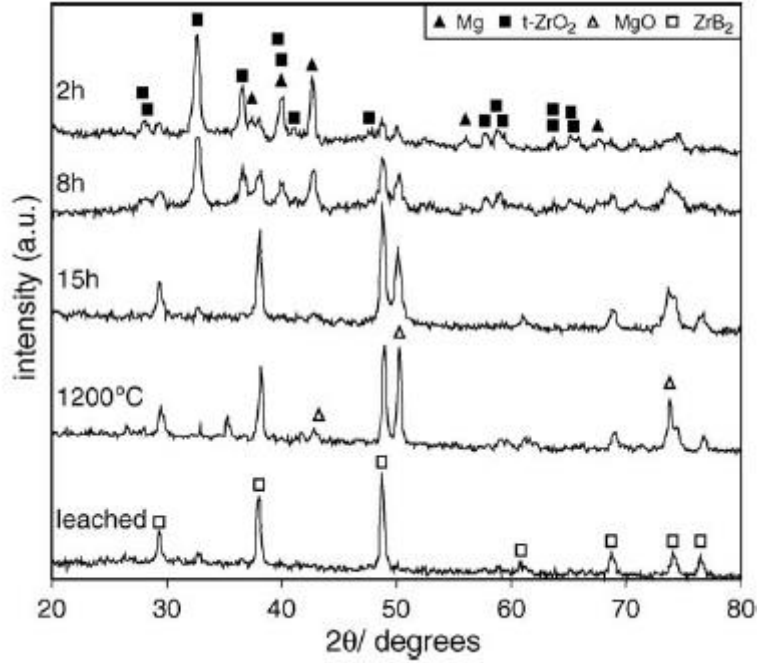


Figure 2.2.3: XRD patterns obtained by magnesiothermic mechanical alloying of ZrB<sub>2</sub> at different milling times, after heating, and after leaching [51].

The effect of excess Mg and B<sub>2</sub>O<sub>3</sub> in magnesiothermic mechanical alloying was independently investigated by Akgün et al. [17]. The addition of 10% excess Mg and B<sub>2</sub>O<sub>3</sub> improved the conversion of ZrO<sub>2</sub> to ZrB<sub>2</sub>. However, contrary to the results reported by Setoudeh and Welham [51], ZrO<sub>2</sub> in the products was present as a monoclinic phase.

The magnesiothermic MSR of ZrB<sub>2</sub> using ZrO<sub>2</sub>, B<sub>2</sub>O<sub>3</sub>, and Mg as the precursor was studied by Jalaly et al. [19]. The complete reaction is described by the following equation:



In this study, 15-mm steel balls were used with a ball-mixture mass ratio of 30:1. The milling was conducted at 600 rpm in a 5 bar Ar atmosphere. It was showed that ignition occurred

after about 6 minutes of continuous milling. After ignition, the mixture was mechanically alloyed for 3 hours at the same rotation speed. Figure 2.2.4 shows the XRD pattern of the mixture before the MRS process, after ignition, after the mechanical alloying step, and after leaching in a 1M HCl solution. It is seen that after ignition (6 min) most of the oxides are converted to  $\text{ZrB}_2$ . However, two phases of  $\text{ZrO}_2$  (monoclinic and tetragonal) are present as impurities. Mechanical alloying for 3 hours helped to completely reduce the oxides.

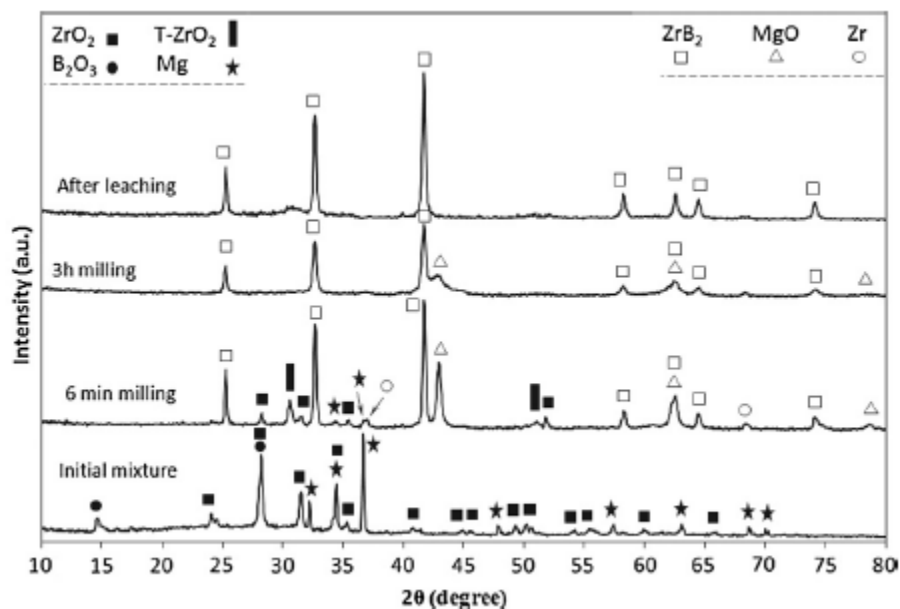


Figure 2.2.4: XRD patterns of the products obtained by magnesiothermic MSR of  $\text{ZrB}_2$ . The figure show the patterns of the initial mixture, after ignition (6 min), after the mechanical alloying step (3 hours), and after leaching [19] .

Differential scanning calorimetry of unmilled stoichiometric mixture was conducted at a heating rate of  $10\text{ }^{\circ}\text{C}/\text{min}$  up to  $1400\text{ }^{\circ}\text{C}$  [19]. Figure 2.2.5 shows that the DSC curve has two exothermic and three endothermic peaks. The first exothermic peak (around  $640\text{ }^{\circ}\text{C}$ ) occurs before

melting of Mg (650 °C) and the second exothermic peak takes place at 850°C, indicating that the combustion is a two-step process. The authors attributed the first two endothermic peaks (100 °C and 180 °C) to vaporization of water, with the second peak being caused by water that was chemically bonded to B<sub>2</sub>O<sub>3</sub>. From quenching experiments at 750 °C and 1000 °C, the authors concluded that the first exothermic peak was caused by Mg/B<sub>2</sub>O<sub>3</sub> reaction and the second exothermic peak by Mg/ZrO<sub>2</sub> reaction.

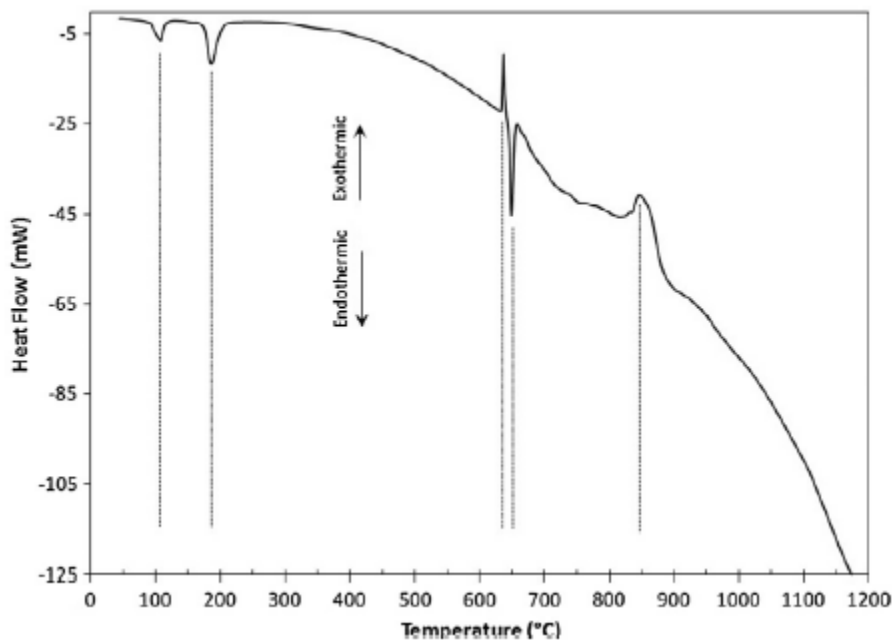
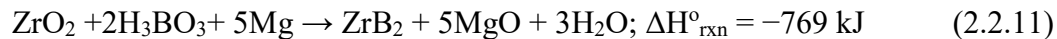


Figure 2.2.5: DSC curve of stoichiometric unmilled stoichiometric ZrO<sub>2</sub>/B<sub>2</sub>O<sub>3</sub>/Mg mixture [47].

The same authors also studied the magnesiothermic synthesis of ZrB<sub>2</sub>/SiC/ZrC mixtures [47] [52]. In these two studies, ZrSiO<sub>4</sub>/B<sub>2</sub>O<sub>3</sub>/C/Mg mixtures at stoichiometric proportions ignited inside the milling bowl, leading to the fabrication of ZrB<sub>2</sub>-SiC-ZrC composites with no oxides impurities.

Khanra et al. conducted magnesiothermic volume combustion synthesis of ZrB<sub>2</sub> [33]. Note that the authors identified the used method as SHS, but, in both studies, the mixtures were globally heated inside a furnace until ignition occurred, which classifies the used method as thermal

explosion, also called volume combustion synthesis (VCS). The boric acid was used as the boron source. The complete chemical reaction is described by:



The authors estimated  $\text{ZrB}_2$  crystallite size at different NaCl concentrations using the Scherrer formula [33]. It was reported that the crystallite size decreased from 25 nm at 0 wt% NaCl to 13 nm at 20 wt% NaCl. In [24],  $\text{ZrO}_2$  impurities were not reported though a small peak of monoclinic  $\text{ZrO}_2$  is visible at  $2\theta = 28^\circ$ . However, in their second VCS work, Khanra et al. did report  $\text{ZrO}_2$  impurities after VCS of the stoichiometric mixture [20]. To improve the conversion of oxides to borides, pre-calculated amounts of Mg and  $\text{B}_2\text{O}_3$  were added to the leached products and a second VCS process was conducted inside the furnace. Figure 2.2.6 shows the XRD patterns of the mixtures obtained by the first VCS process, after leaching the products of the first VCS process, and after leaching the products of the second VCS process. It is seen that conducting a second VCS step slightly increases the conversion of oxides to borides. However, it adds complexity and increases the processing time. Nishiyama et al. also conducted magnesiothermic VCS of  $\text{ZrB}_2$ , but with  $\text{B}_2\text{O}_3$  instead of  $\text{H}_3\text{BO}_2$  as a precursor [53]. Similarly to [20] [33], the obtained products consisted of  $\text{ZrB}_2$  with  $\text{ZrO}_2$  impurities.

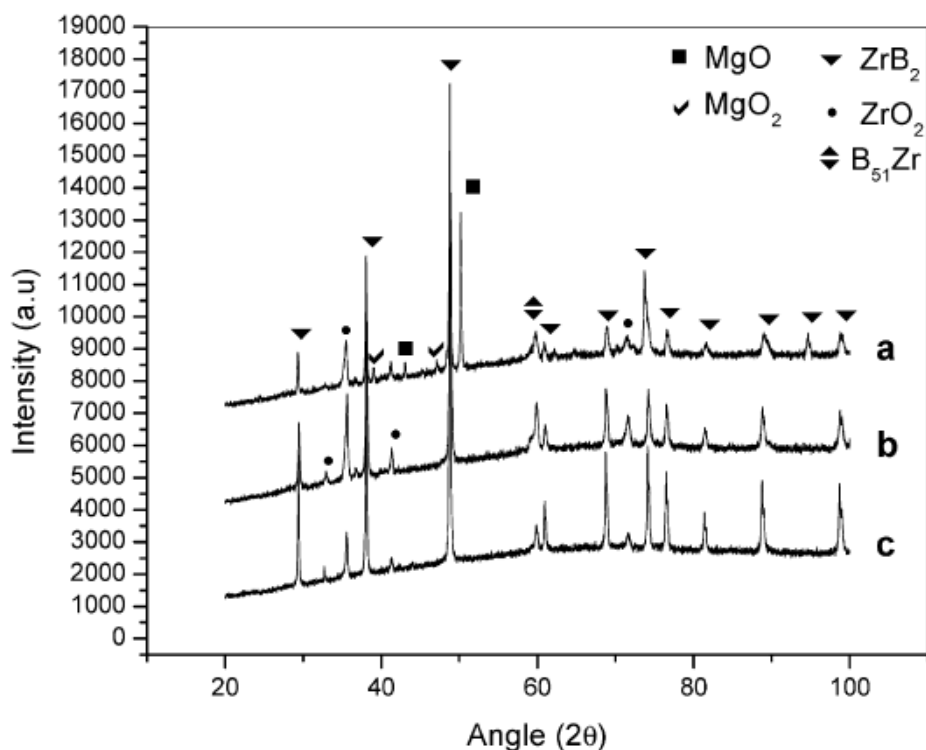


Figure 2.2.6: XRD patterns obtained by magnesiothermic VCS of  $\text{ZrB}_2$ . The figure shows the patterns of the mixture obtained by VCS (a), the leached mixture after VCS (b), and the leached mixture after the second VCS step (c) [20].

Mishra et al. investigated the magnesiothermic SHS of  $\text{ZrB}_2$  following Eq. 2.2.10 [41]. In the reported XRD patterns,  $\text{ZrO}_2$  is not present or identified by the authors. However, there are unlabeled peaks in the XRD pattern.

The reaction mechanisms of the combustion of  $\text{ZrO}_2/\text{H}_3\text{BO}_2/\text{Mg}$  mixture were investigated with DSC and TGA by Khanra [54]. The reported results showed that  $\text{H}_3\text{BO}_2$  melts and dissociates at 139 and 169°C, respectively. One exothermic peak was reported at 853°C.

Zheng et al. conducted DSC and TGA of  $\text{ZrO}_2/\text{B}_2\text{O}_3/\text{Mg}$  milled mixture at 20 °C/min [55]. The DSC and TGA curves, shown in Fig. 2.2.7, reveal a significant weight loss (around 15%) and an endothermic peak around 100 °C attributed to water evaporation. An exothermic peak is reported at 745°C after melting of Mg (650 °C). Also, weight gain is reported at 745 °C, which is apparently an experimental error.

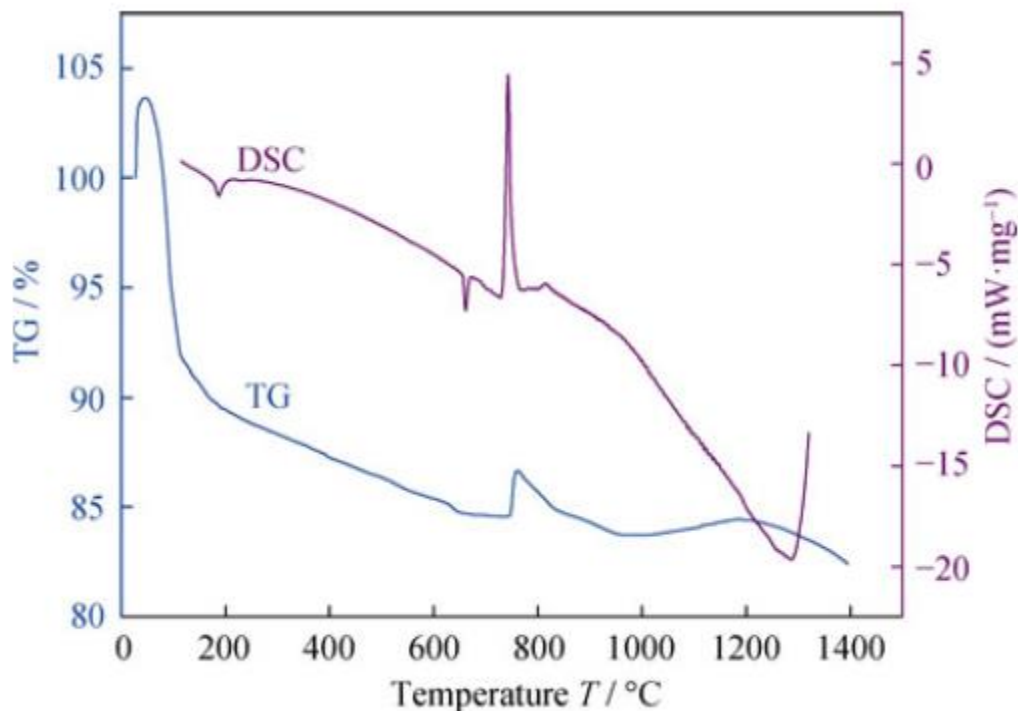
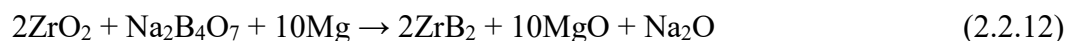


Figure 2.2.7: DSC curve of milled stoichiometric  $\text{ZrO}_2/\text{B}_2\text{O}_3/\text{Mg}$  mixture [55].

The effect of HCl concentration on the leaching of  $\text{ZrB}_2/\text{MgO}$  mixtures was reported by Akkas et al. [18]. It was found that after acid leaching,  $\text{ZrO}_2$  appeared in the products, i.e.  $\text{ZrB}_2$  was oxidized.

Raschman and Fedoročová studied the reaction kinetics of MgO leaching [56]. It was reported that increasing the leaching temperature significantly improves the dissolving rate of MgO. Full dissolution was reached with the three tested temperatures (45, 60, and 75°C).

Zhang et al. synthesized  $\text{ZrB}_2$  *via* molten-salt magnesiothermic reduction of  $\text{ZrO}_2$  and  $\text{Na}_2\text{B}_4\text{O}_7$  [57]. The chemical reaction that describes this route is shown below:



The powders were mixed in stoichiometric proportions with 10 to 30 wt% excess Mg and/or  $\text{Na}_2\text{B}_4\text{O}_7$ . The synthesis was conducted inside a furnace filled with argon at 800-1200°C

for 3 hours. Impurities of  $\text{ZrO}_2$  and  $\text{Mg}_3\text{B}_2\text{O}_6$  were found in the experiments conducted at stoichiometric proportions, but full conversion was achieved for mixtures with 30 wt% excess  $\text{Na}_2\text{B}_4\text{O}_7$ .

In conclusion, synthesis of  $\text{ZrB}_2$  with a magnesiothermic reduction step is the most promising metallothermic approach, because  $\text{MgO}$  can be easily removed from the products by mild acid leaching. However, incomplete conversion of oxides (or acids) to borides is a major problem in this approach.

### 2.2.6. Summary of fabrication methods

Various methods for synthesis of  $\text{ZrB}_2$  and  $\text{HfB}_2$  were reviewed in this section. The following list summarizes the advantages and drawbacks of each method.

1. Synthesis from elements: by taking advantage of the high-exothermicity of  $\text{Zr/B}$  and  $\text{Hf/B}$  mixtures,  $\text{ZrB}_2$  and  $\text{HfB}_2$  can be fabricated by SHS without mechanical activation. High-purity products can be obtained by this route, but the high costs of  $\text{Zr}$ ,  $\text{Hf}$ , and  $\text{B}$  make this method economically unviable.
2. Boron carbide reduction: this method requires a high-temperature furnace (up to  $1850^\circ\text{C}$ ). Pure  $\text{ZrB}_2$  can be obtained by adding excess  $\text{B}_4\text{C}$  and  $\text{C}$ . This method is attractive for the fabrication because of the relatively low cost of the reactants, but it requires a high-temperature furnace and a large energy input.
3. Borothermic reduction:  $\text{ZrB}_2$  (with  $\text{ZrO}_2$  impurities) was successfully synthesized, but the long processing time (70 h) and loss of almost half the boron makes this method unattractive.
4. Carbothermic reduction: this technique is conducted under the same conditions as boron carbide reduction, but because of the high processing temperature ( $1800^\circ\text{C}$ ), boron is lost *via*  $\text{B}_2\text{O}_3$  vaporization, leading to incomplete conversion.
5. Aluminothermic reduction: borides of zirconium and hafnium can be successfully obtained by aluminothermic combustion synthesis. However, the aluminum oxide

product cannot be separated from the borides, making this process less attractive when the goal is fabrication of pure borides.

6. Magnesiothermic reduction: the synthesis of  $\text{ZrB}_2$  was successfully demonstrated in various studies, but impurities of  $\text{ZrO}_2$  were found in the products. The simple approach, short-processing time, and relatively cheap raw materials make this method extremely attractive provided that an effective method for decreasing  $\text{ZrO}_2$  impurities is found.

In conclusion, all the reviewed methods have advantages and disadvantages. Most techniques are complex and require long processing times as well as expensive raw materials. A more promising approach, magnesiothermic combustion synthesis of  $\text{ZrB}_2$ , has been extensively studied. However, it is not fully understood why the oxides were not fully reduced in this method. In the present work, a better understanding of processes occurring during magnesiothermic combustion synthesis of diborides will be obtained via thermodynamic analysis and experimental studies that involve mechanical activation and use of inert diluents.,



## Chapter 3: Experimental Procedures and Facilities

### 3.1. Powder Processing

This section explains the process and equipment utilized to prepare the powders for combustion experiments. First, the as-received powders were mixed in an Ar environment. Then the powder mixture was mechanically activated in a high-energy ball mill. NaCl and MgO were used to facilitate the milling process.

#### 3.1.1. Mixing

Zirconium (IV) oxide ( $\text{ZrO}_2$ , -325 mesh, 99.7% pure, Alfa Aesar), hafnium (IV) oxide ( $\text{HfO}_2$ , -325 mesh, 99% pure, Alfa Aesar), boron trioxide ( $\text{B}_2\text{O}_3$ , 99.8% pure, Sigma-Aldrich), magnesium (Mg, -325 mesh, 99.8% pure, Sigma-Aldrich), magnesium oxide ( $\text{MgO}$ , -325 mesh,  $\geq 99\%$  pure, Sigma-Aldrich) and sodium chloride (NaCl, 99% pure, Sigma-Aldrich) powders were used as starting materials. The molar ratio was chosen according to the table 3.1.

Table 3.1: Compositions of the prepared mixtures.

System	$\text{ZrO}_2$	$\text{HfO}_2$	$\text{B}_2\text{O}_3$	Mg	NaCl	MgO
	mol					
$\text{ZrO}_2\text{-B}_2\text{O}_3\text{-Mg-NaCl}$	1	0	1	5 – 6	0 – 6.6	0
$\text{ZrO}_2\text{-B}_2\text{O}_3\text{-Mg-MgO}$	1	0	1	5	0	0 – 5.2
$\text{HfO}_2\text{-B}_2\text{O}_3\text{-Mg-NaCl}$	0	1	1	5	1.7	0

The powders were mixed in a three-dimensional inversion kinematic tumbler mixer (Inversina 2L, Bioengineering, Fig. 3.1.1). To avoid Mg oxidation, mixing was conducted in a

sealed container filled with ultra-high purity argon. The total mass of the prepared mixture was 15 g in all experiments.



(a)



(b)

Figure 3.1.1: Mixer (Inversina 2L, Bioengineering) with (a) closed and (b) opened protective shield.

### 3.1.2. Mechanical Activation

The mixed powders were mechanically activated in a high-energy planetary ball mill (Fritsch Pulverisette 7 Premium Line, Fig. 3.1.2.a) using zirconia-coated grinding bowls (Fig. 3.1.2.b) and zirconia grinding balls (diameter: 3 mm). The total mass of powders to mill was 15 g and the balls-mixture mass ratio was 20:3. Prior to milling, the grinding bowls were purged with ultra-high purity argon to avoid combustion/oxidation of Mg inside the bowl during milling. The milling speed was 1000 rpm and four total milling times were used: 1, 5, 10, and 30 minutes. To prevent high temperatures and reactions during milling, the process was separated in 1-min milling

periods with 60-min cooling pauses between each cycle (e.g., a total milling time of 5 min was divided in 5 cycles).



(a)



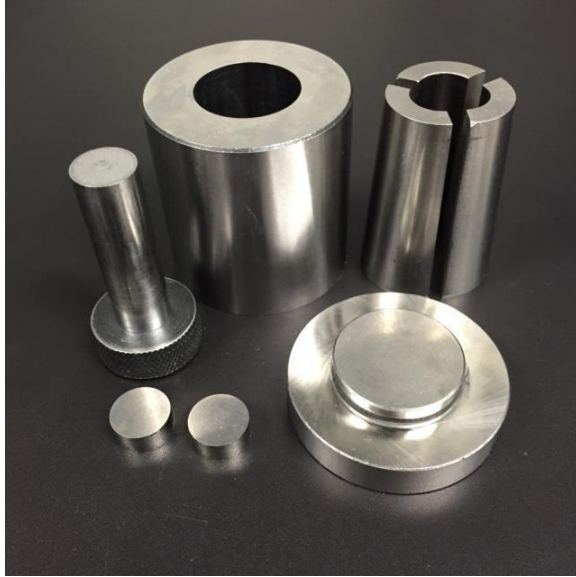
(b)

Figure 3.1.2: Milling equipment: (a) planetary mill (Fritsch Pulverisette 7 Premium Line) and (b) grinding bowl with purging valves.

### 3.2. Preparation of Pellets

The mechanically activated mixtures were compacted into 4-g cylindrical pellets (diameter: 13 mm, height: 13–23 mm) in a pressing die (Across International, Fig. 3.2.1.a) using a uniaxial hydraulic press (Carver, Fig. 3.2.1.b). The variation of height of the pellets was caused by the variation of density in the different mixtures. Pressing was conducted at 150 MPa with a holding time of 5 minutes. After compaction, two 6.5-mm deep channels for thermocouples were drilled perpendicularly to the pellet axis. The channels were positioned 10 mm apart from each other for determination of the combustion front velocity. Also, 1-g booster pellets (diameter: 13 mm) of titanium/boron mixture (1:2 molar ratio) were compacted at the same pressing parameters.

After milling, the bowl was opened inside of a glovebox (Terra Universal, Series 300) in atmosphere of 5% O<sub>2</sub> and 95%N<sub>2</sub>.



(a)



(b)

Figure 3.2.1: Pressing equipment: (a) die set and (b) uniaxial hydraulic press.

### 3.3. Combustion Experiments

The combustion process was conducted inside a windowed steel chamber (diameter 30 cm, height 40 cm, Fig. 3.3.1), connected to a compressed argon cylinder and a vacuum pump. All experiments were conducted in an argon environment at 1 atm. The pellet was placed on top of 3-mm thick thermal paper (Fiberfrax) and ignited at the top by a tungsten wire (diameter 0.43 mm, length 150 mm, Midwest Tungsten Service Inc.) heated with a DC power supply (Mastech) set at 15 V. The combustion temperature in the middle of the pellet was measured by two WRe5%/WRe26% thermocouples (type C, wire diameter: 76  $\mu$ m, Omega Engineering). Each thermocouple was located in a two-channel ceramic insulator (outer diameter: 0.8 mm, Omegatite

450, Omega Engineering) and inserted into the pellet through the channel drilled as described in Section 3.2. Digital video recording (Sony XCD-SX90CR) was used for observation.

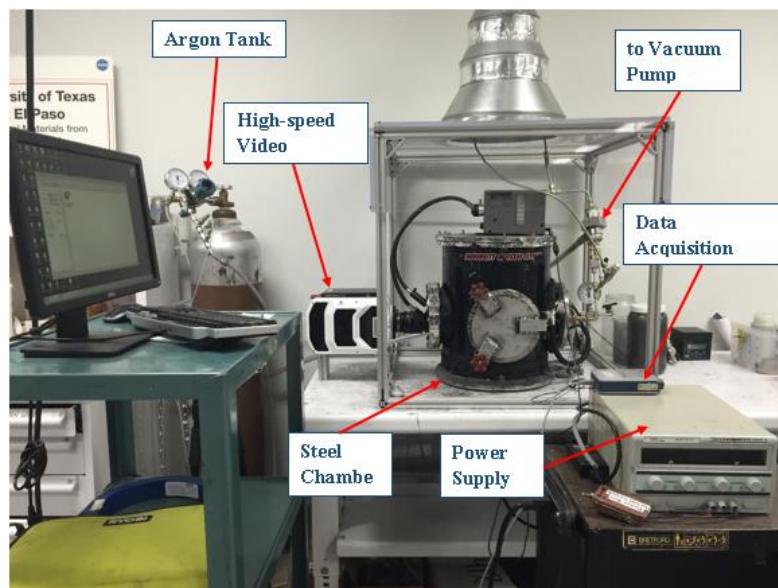


Figure 3.3.1: Hot-wire ignition setup.

### 3.4. Leaching

After combustion, MgO and NaCl in the products were leached in 200 mL of 1M HCl solution (SMART). The dissolution process was carried out in an Erlenmeyer flask with a mechanical stirrer at atmospheric pressure and room temperature for 2 hours. The remaining solid products were separated from the acid using a paper filter. Then, the solid products were washed in deionized water and dried at room temperature for 24 hours.

### 3.5. Thermoanalytical Studies

The reaction mechanisms of the mixtures were studied by thermoanalytical methods using a differential scanning calorimeter (Netzsch DSC 404 F1 Pegasus, Fig. 3.5.1.a) and a thermogravimetric analyzer (Netzsch TGA 209 F1 Iris, Fig. 3.5.1.b). The samples (5 or 10 mg)

were heated to 1000 °C in 80- $\mu$ L alumina ( $\text{Al}_2\text{O}_3$ ) crucibles. The tests were conducted in an ultra-high purity argon flow (70 ml/min) at a heating rate of 20 °C/min.

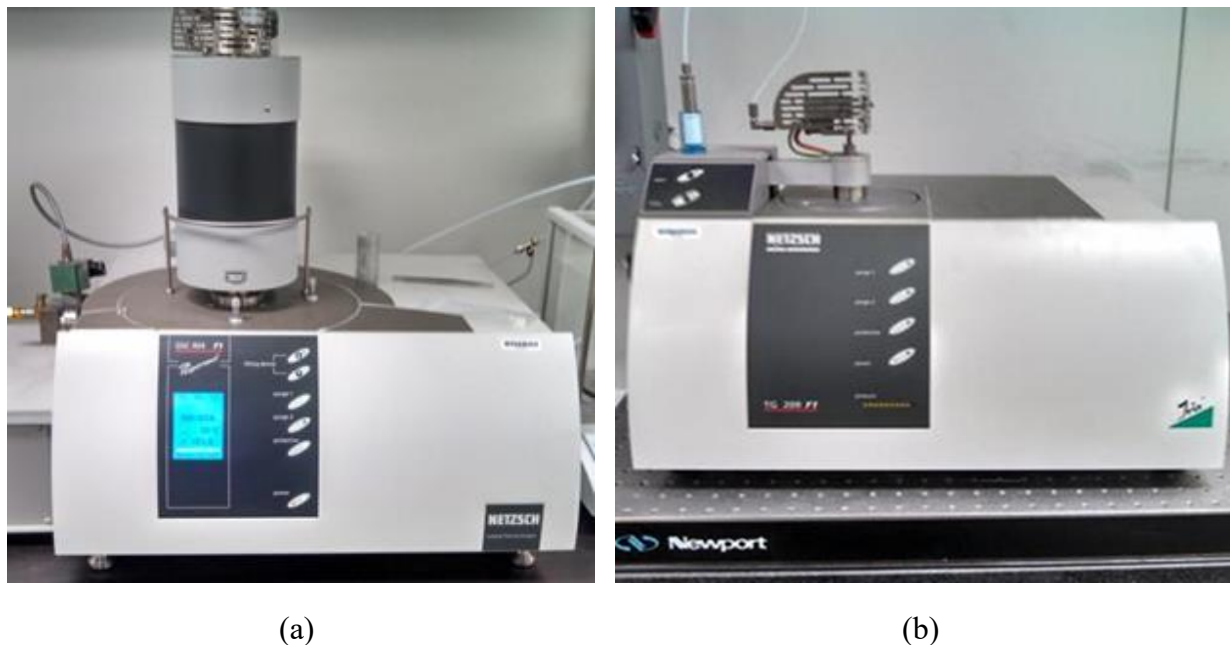


Figure 3.5.1: Thermoanalytical instruments: (a) Netzsch DSC 404 F1 Pegasus and (b) Netzsch TGA 209 F1 Iris.

### 3.6. Characterization of Materials

The characterization of the powders was performed with three techniques: laser diffraction particle size analysis, powder X-ray diffraction analysis, and scanning electron microscopy. The following subsections present the used instruments and the testing parameters.

#### 3.6.1. Laser Diffraction Particle Size Analysis

Particle size distribution of the as-received powders and milled mixtures were conducted in a laser diffraction particle size analyzer (Microtrac Bluewave, Fig. 3.6.1). To avoid oxidation or dissolution of the powders, isopropyl alcohol (VWR International) was used as the sample carrier.





Figure 3.6.1: Particle size analyzer (Microtrac Bluewave).

### 3.6.2. Powder X-Ray Diffraction Analysis

Compositions of the milled mixtures and combustion products before and after leaching were studied using powder X-ray diffraction analysis (Bruker D8 Discover XRD, Cu K-alpha 1, 0.154 nm, Fig. 3.6.2). The scan was conducted in a  $2\theta$  range of 20 to 60° with a scan speed of 5 °/min and a step size of 0.02°.



Figure 3.6.2: X-ray diffractometer (Bruker D8 Discover XRD).

### 3.6.3. Scanning Electron Microscopy

The morphology of the leached powders was studied using a scanning electron microscope (SEM, Hitachi S-4800, Fig. 3.6.3) with a secondary electrons detector. The samples were compacted into pellets (diameter: 6.5 mm) and mounted in carbon conductive tabs (diameter: 12 mm). The accelerating voltage was varied from 10 to 25 kV.



Figure 3.6.3: Scanning electron microscope (SEM, Hitachi S-4800).



## Chapter 4: Results and Discussion

### 4.1. Thermodynamic Calculations

Previous experiments have shown that fabrication of  $\text{ZrB}_2$  from  $\text{ZrO}_2$  and  $\text{B}_2\text{O}_3$  using their exothermic reactions with Mg results in an incomplete conversion of  $\text{ZrO}_2$  to  $\text{ZrB}_2$  [51] [17] [19]. This is a major problem because separation of  $\text{ZrO}_2$  from the product mixture would be a very complicated and expensive process, in contrast with easy separation of MgO by dissolution in HCl. It is expected that the addition of excess Mg (over the stoichiometric ratio) may increase the conversion extent because that additional Mg will react with the remaining  $\text{ZrO}_2$ . It has also been hypothesized that the addition of an inert material may improve the conversion because of decreasing the combustion temperature and hence reducing the loss of Mg by vaporization. All this is also fully related to the conversion of  $\text{HfO}_2$  to  $\text{HfB}_2$ . To verify these hypotheses, thermodynamic calculations have been conducted for combustion of  $\text{ZrO}_2$ - $\text{B}_2\text{O}_3$ -Mg and  $\text{HfO}_2$ - $\text{B}_2\text{O}_3$ -Mg systems with the addition of extra Mg, NaCl, or MgO.

The thermodynamic calculations for the adiabatic flame temperature and combustion products were conducted using THERMO (version 4.3) software, which is based on the Gibbs function minimization and contains a database of approximately 3000 compounds [58]. The temperature of the initial reactants was set to 298 K and the pressure was maintained constant at 1 atm in all calculations.

First, calculations were done for  $\text{ZrO}_2$ - $\text{B}_2\text{O}_3$ -Mg and  $\text{HfO}_2$ - $\text{B}_2\text{O}_3$ -Mg systems. The mole fraction of Mg in the mixture was varied from 0 to 1, while the stoichiometry is at 0.71.  $\text{ZrO}_2$ : $\text{B}_2\text{O}_3$  and  $\text{HfO}_2$ : $\text{B}_2\text{O}_3$  mole ratios were maintained at 1 in all calculations. Figures 4.1.1 and 4.1.2 show the obtained adiabatic flame temperatures and product compositions for  $\text{ZrO}_2$ - $\text{B}_2\text{O}_3$ -Mg and  $\text{HfO}_2$ - $\text{B}_2\text{O}_3$ -Mg, respectively. It is seen that in both systems, the maximum temperature is reached at stoichiometry, 2370 K for  $\text{ZrO}_2$ - $\text{B}_2\text{O}_3$ -Mg and 2380 K for  $\text{HfO}_2$ - $\text{B}_2\text{O}_3$ -Mg. However, 100% conversion of  $\text{ZrO}_2$  to  $\text{ZrB}_2$  (or  $\text{HfO}_2$  to  $\text{HfB}_2$ ) is not achieved until the mole fraction of Mg in the initial mixture increases to approximately 0.77 (or 40% excess Mg). For clarity, Figure 4.1.3

shows the conversion degree of  $\text{ZrO}_2$  to  $\text{ZrB}_2$ . The same figure also shows the conversion of  $\text{HfO}_2$  to  $\text{HfB}_2$  because all mole ratios are the same in both systems.

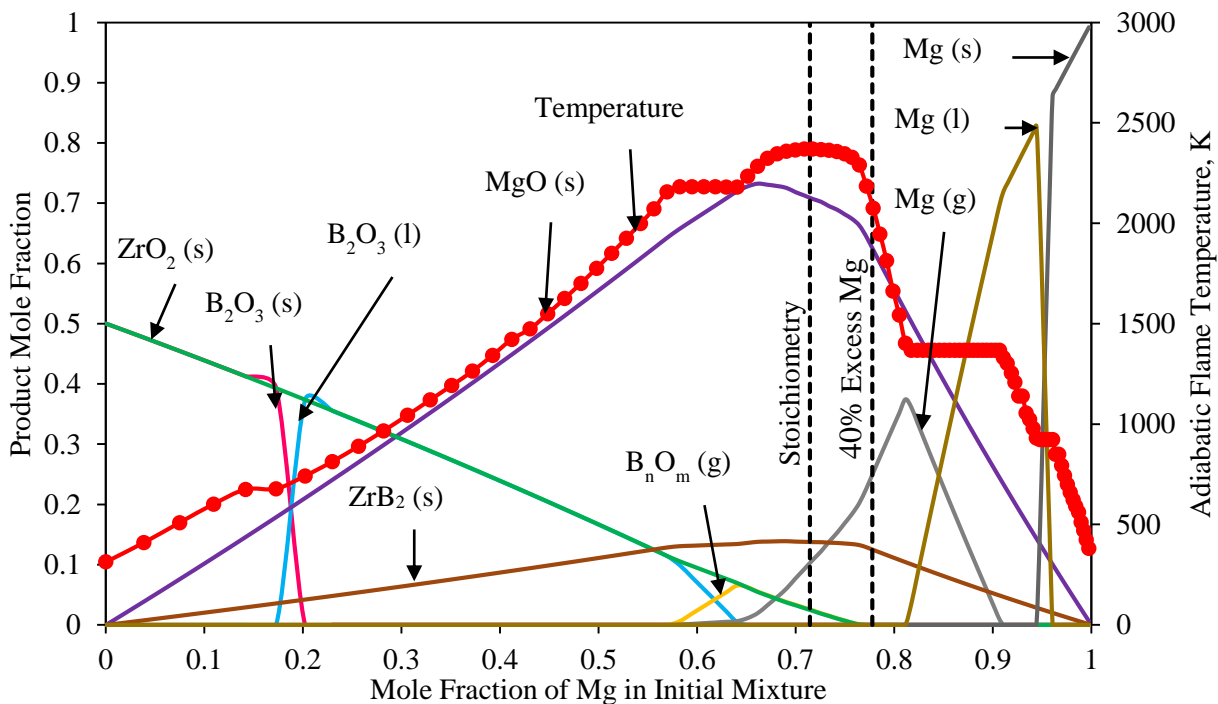


Figure 4.1.1: Adiabatic flame temperature and equilibrium product composition vs NaCl concentration in  $\text{ZrO}_2\text{--B}_2\text{O}_3\text{--Mg--NaCl}$  system.  $\text{B}_n\text{O}_m$  and  $\text{Na}_n\text{Cl}$  are used for gas mixtures  $\text{B}_2\text{O}_3/\text{B}_2\text{O}_2/\text{BO}$  and  $\text{NaCl}/\text{Na}_2\text{Cl}_2/\text{Na}_3\text{Cl}_3$ , respectively.

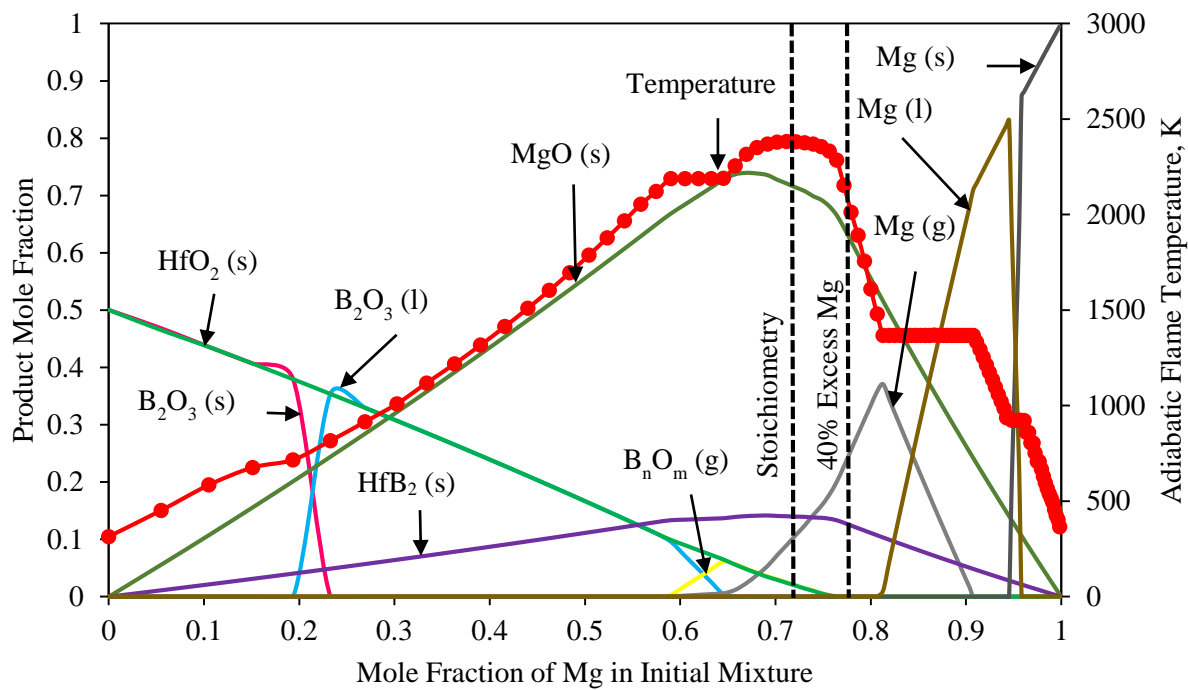


Figure 4.1.2: Adiabatic flame temperature and equilibrium product composition vs NaCl concentration in  $\text{HfO}_2\text{-B}_2\text{O}_3\text{-Mg-NaCl}$  system.  $\text{B}_n\text{O}_m$  and  $\text{Na}_n\text{Cl}$  are used for gas mixtures  $\text{B}_2\text{O}_3/\text{B}_2\text{O}_2/\text{BO}$  and  $\text{NaCl}/\text{Na}_2\text{Cl}_2/\text{Na}_3\text{Cl}_3$ , respectively.

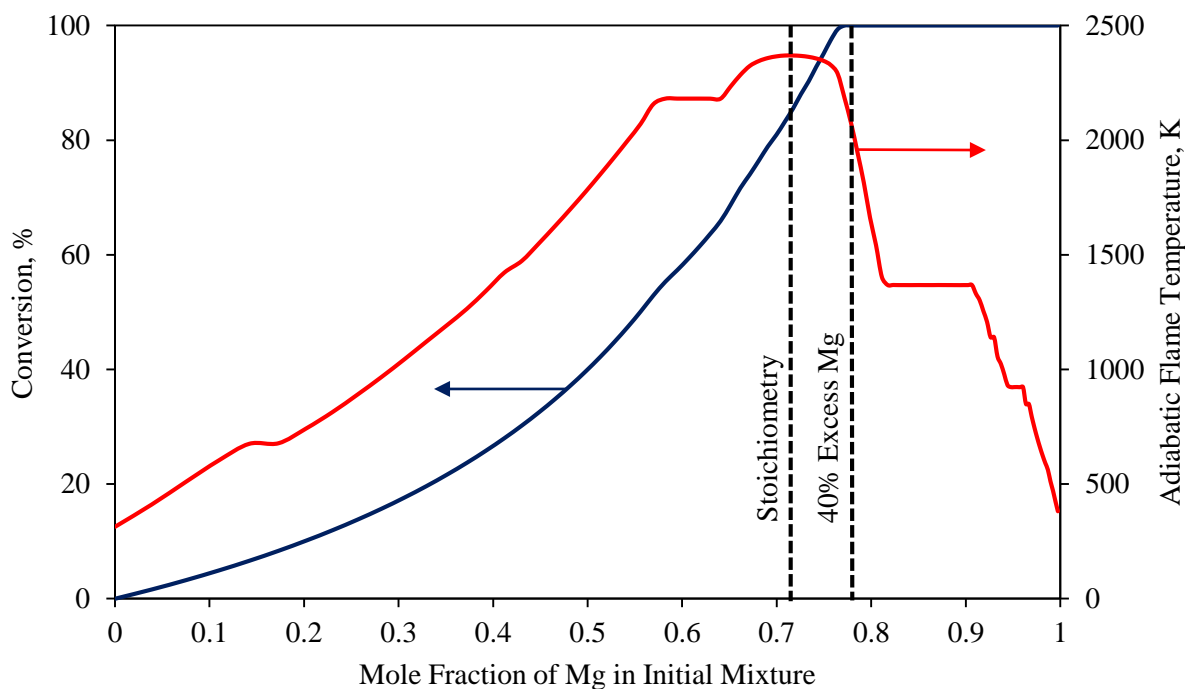


Figure 4.1.3: Adiabatic flame temperature and conversion of  $\text{ZrO}_2$  to  $\text{ZrB}_2$  (or  $\text{HfO}_2$  to  $\text{HfB}_2$ ) vs Mg concentration in  $\text{ZrO}_2\text{--B}_2\text{O}_3\text{--Mg}$  (or  $\text{HfO}_2\text{--B}_2\text{O}_3\text{--Mg}$ ) system.

In general, these results indicate that full conversion is possible having a significant excess of Mg in the initial mixture. Note that the adiabatic flame temperature at this point remains sufficiently high (2130 K) for maintaining a self-sustained combustion. However, the results also show (see Figs. 4.1.1 and 4.1.2) that, because of the relatively low boiling point of Mg (1368 K at 1 atm), a significant amount of gaseous Mg is present in the products at the combustion temperature, which may lead to the loss of Mg and an undesired pressure increase in the reaction chamber.

In addition, thermodynamic calculations at constant temperature (2360 K) were conducted for the stoichiometric mixtures. In this calculations, full conversion was attained. This result revealed that the conversion degree is temperature dependent. Thus, at stoichiometry, temperatures lower than the adiabatic temperature are needed for full conversion. Note that in the experiments, heat losses decrease the combustion temperature. By tuning the heat losses, it may be possible to

improve the conversion, while maintaining a sufficiently high temperature for the combustion wave propagation.

The combustion temperature can also be decreased by the addition of an inert material to the initial mixture. Note that it is planned to use NaCl as an additive to facilitate ball milling of the mixtures. It makes sense to consider a possibility of leaving NaCl in the milled stoichiometric  $\text{ZrO}_2/\text{B}_2\text{O}_3/\text{Mg}$  and  $\text{HfO}_2/\text{B}_2\text{O}_3/\text{Mg}$  mixtures to lower the combustion temperature and improve the conversion. This may also decrease the combustion front velocity and particle size of the formed  $\text{ZrB}_2$  and  $\text{HfB}_2$ . The decrease in the particle size is desired for improving sinterability and properties of the diborides.

To investigate the effect of NaCl on the combustion, thermodynamic calculations were conducted for  $\text{ZrO}_2\text{--B}_2\text{O}_3\text{--Mg--NaCl}$  and  $\text{HfO}_2\text{--B}_2\text{O}_3\text{--Mg--NaCl}$  systems. The ratio of  $\text{ZrO}_2\text{:B}_2\text{O}_3\text{:Mg}$  (or  $\text{HfO}_2\text{:B}_2\text{O}_3\text{:Mg}$ ) was maintained constant at stoichiometry (1:1:5), while the mole fraction of NaCl in the mixture was varied from 0 to 1. Figures 4.1.4 and 4.1.5 show the adiabatic flame temperatures and product compositions, while Figure 4.1.6 presents the conversion degree of oxides to borides as a function of the mole fraction of NaCl in the initial mixture.

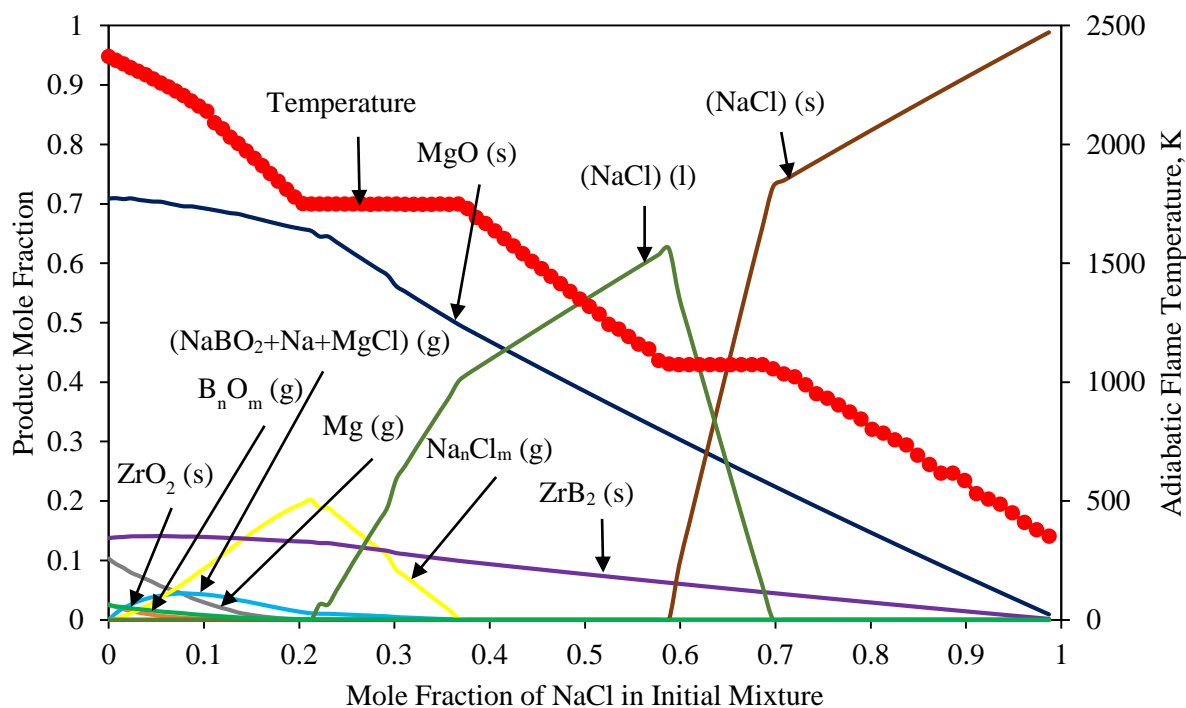


Figure 4.1.4: Adiabatic flame temperature and equilibrium product composition vs NaCl concentration in  $\text{ZrO}_2\text{-B}_2\text{O}_3\text{-Mg-NaCl}$  system.  $\text{B}_n\text{O}_m$  and  $\text{Na}_n\text{Cl}_m$  are used for gas mixtures  $\text{B}_2\text{O}_3/\text{B}_2\text{O}_2/\text{BO}$  and  $\text{NaCl}/\text{Na}_2\text{Cl}_2/\text{Na}_3\text{Cl}_3$ , respectively.

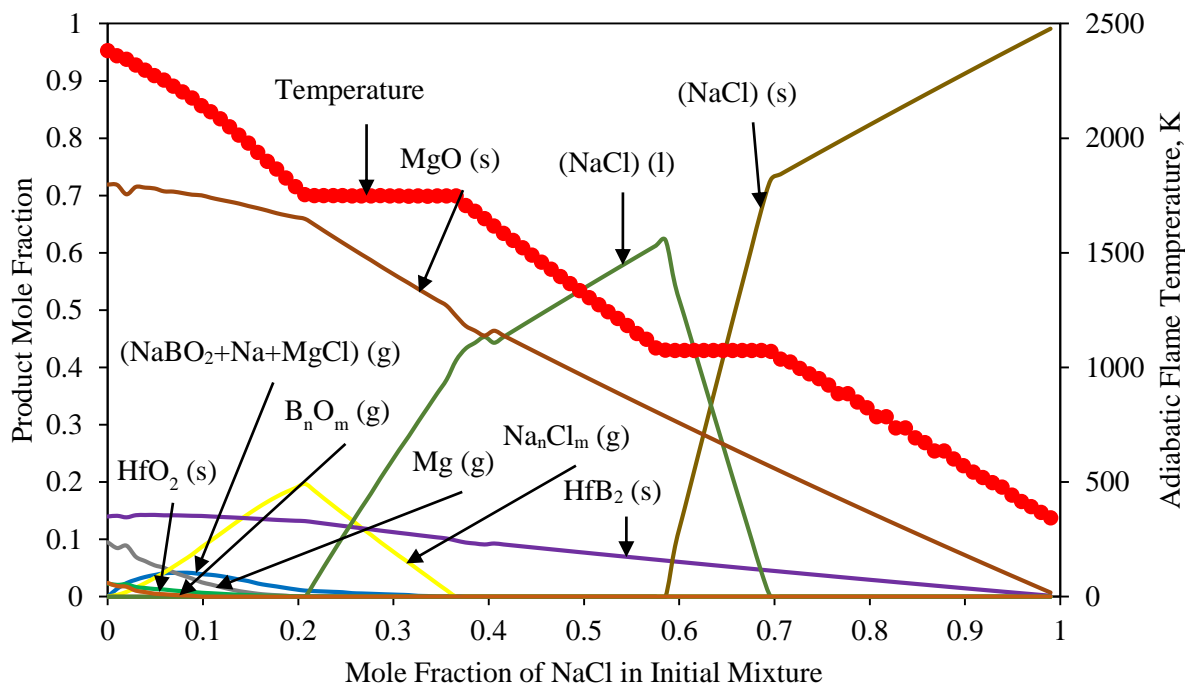


Figure 4.1.5: Adiabatic flame temperature and equilibrium product composition vs NaCl concentration in  $\text{HfO}_2\text{-B}_2\text{O}_3\text{-Mg-NaCl}$  system.  $\text{B}_n\text{O}_m$  and  $\text{Na}_n\text{Cl}_m$  are used for gas mixtures  $\text{B}_2\text{O}_3/\text{B}_2\text{O}_2/\text{BO}$  and  $\text{NaCl}/\text{Na}_2\text{Cl}_2/\text{Na}_3\text{Cl}_3$ , respectively.

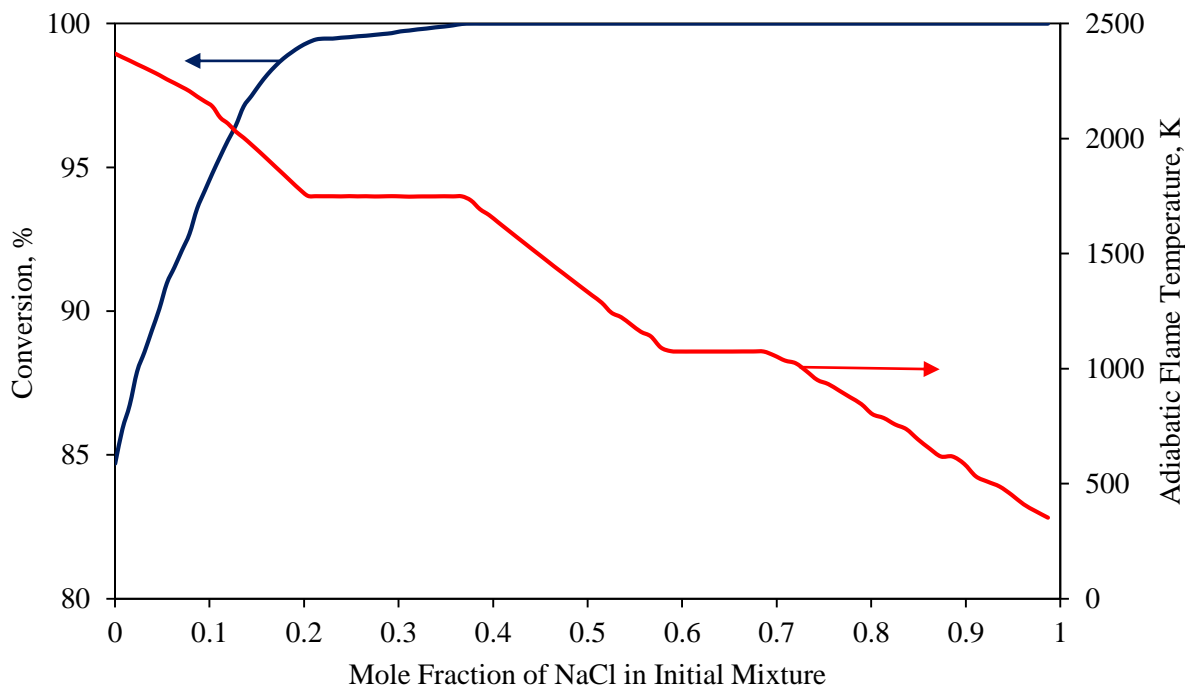


Figure 4.1.6: Adiabatic flame temperature and percent conversion of  $\text{ZrO}_2$  to  $\text{ZrB}_2$  (or  $\text{HfO}_2$  to  $\text{HfB}_2$ ) vs NaCl concentration in  $\text{ZrO}_2\text{--B}_2\text{O}_3\text{--Mg--NaCl}$  (or  $\text{HfO}_2\text{--B}_2\text{O}_3\text{--Mg--NaCl}$ ) system.

The results indicate that 100% conversion of  $\text{ZrB}_2$  (or  $\text{HfB}_2$ ) can be achieved by increasing the mole fraction of NaCl in the initial mixture to approximately 0.37. The adiabatic flame temperature at this point is around 1730 K, which is sufficiently high for combustion. In this system, the drop of combustion temperature by itself does not let to full conversion, because NaCl gas molecules dissociate and combine with Mg leading to a change in molar proportion. Note that full conversion is reached just before the boiling point of NaCl (1686 K).

In addition, MgO was considered as an additive because it is a recyclable byproduct of the magnesiothermic synthesis. Thermodynamic calculations were done for  $\text{ZrO}_2\text{--B}_2\text{O}_3\text{--Mg--MgO}$  and  $\text{HfO}_2\text{--B}_2\text{O}_3\text{--Mg--MgO}$  systems. The mole fraction of MgO was varied from 0 to 1, while  $\text{ZrO}_2/\text{B}_2\text{O}_3/\text{Mg}$  and  $\text{HfO}_2/\text{B}_2\text{O}_3/\text{Mg}$  mole ratios were maintained constant at stoichiometry. Figures 4.1.7 and 4.1.8 show the adiabatic flame temperatures and the product compositions, while Figure



4.1.9 presents the conversion degree of  $\text{ZrO}_2$  to  $\text{ZrB}_2$  (or  $\text{HfO}_2$  to  $\text{HfB}_2$ ) as a function of the mole fraction of  $\text{MgO}$  in the initial mixture.

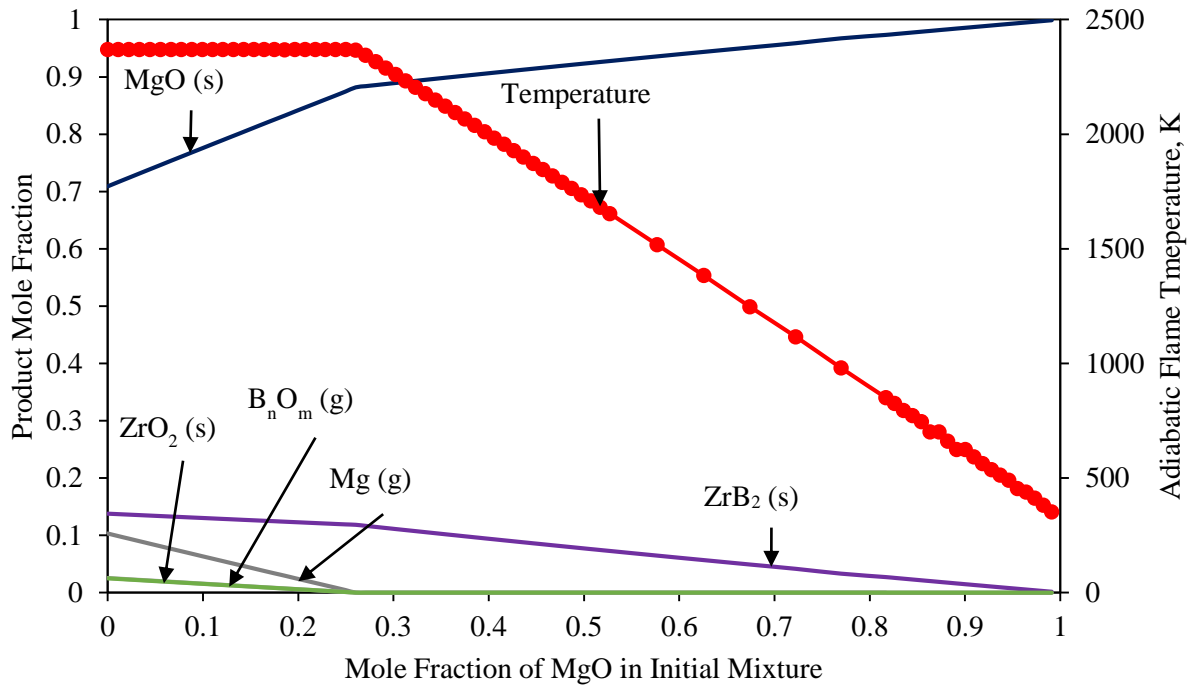


Figure 4.1.7: Adiabatic flame temperature and equilibrium product composition vs  $\text{MgO}$  concentration in  $\text{ZrO}_2\text{--B}_2\text{O}_3\text{--Mg--MgO}$  system.  $\text{B}_n\text{O}_m$  is used for a mixture of  $\text{B}_2\text{O}_3/\text{B}_2\text{O}_2/\text{BO}$  gases.

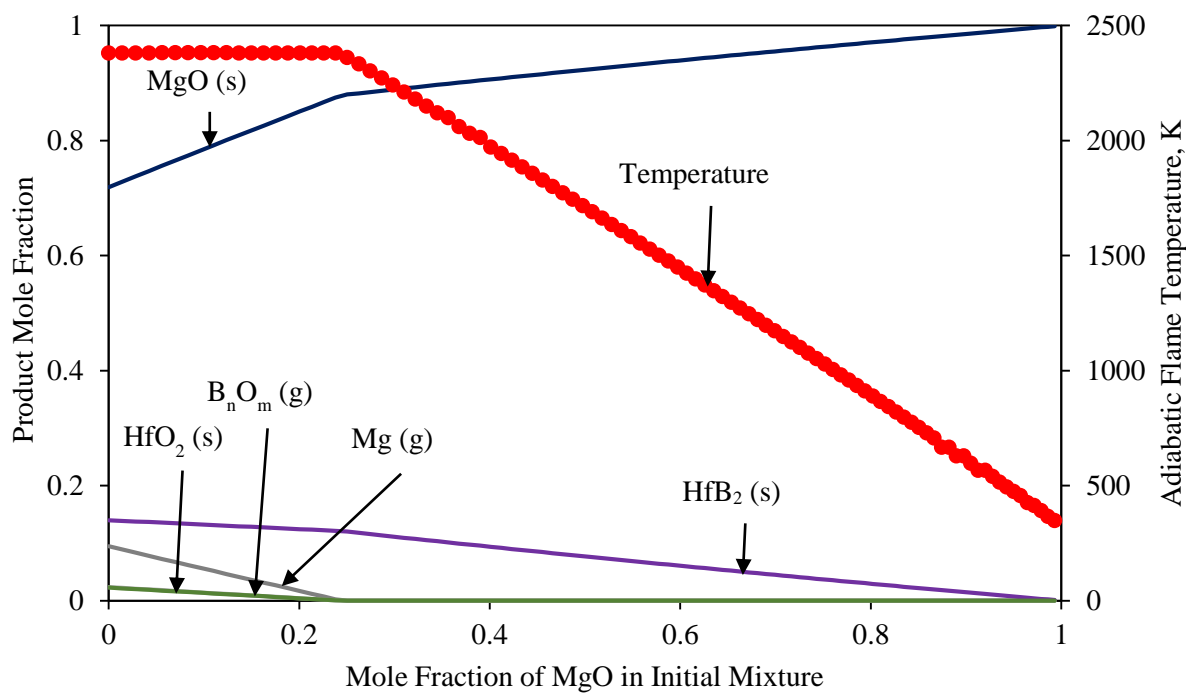


Figure 4.1.8: Adiabatic flame temperature and equilibrium product composition *vs* MgO concentration in HfO<sub>2</sub>–B<sub>2</sub>O<sub>3</sub>–Mg–MgO system. B<sub>n</sub>O<sub>m</sub> is used for a mixture of B<sub>2</sub>O<sub>3</sub>/B<sub>2</sub>O<sub>2</sub>/BO gases.

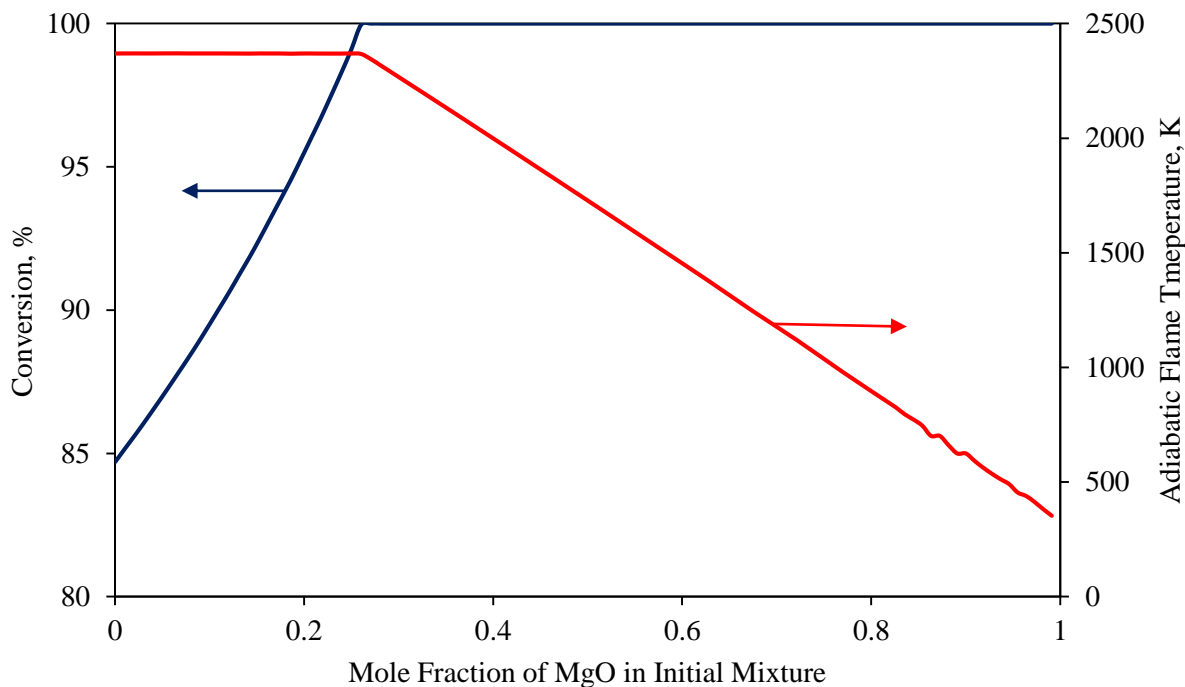


Figure 4.1.9: Adiabatic flame temperature and percent conversion of  $\text{ZrO}_2$  to  $\text{ZrB}_2$  (or  $\text{HfO}_2$  to  $\text{HfB}_2$ ) vs Mg concentration in  $\text{ZrO}_2\text{--B}_2\text{O}_3\text{--Mg--MgO}$  (or  $\text{HfO}_2\text{--B}_2\text{O}_3\text{--Mg--MgO}$ ) system.

These plots show that full conversion of oxides to borides can be achieved by increasing the mole fraction of MgO in the initial mixture to about 0.27 and that the temperature at this point is approximately 2350 K, which is close to the maximum temperature reached at stoichiometry (2380 K). The higher adiabatic flame temperatures in  $\text{ZrO}_2\text{--B}_2\text{O}_3\text{--Mg--MgO}$  and  $\text{HfO}_2\text{--B}_2\text{O}_3\text{--Mg--MgO}$  systems are partly explained by the absence of phase changes in the products (after full conversion of borides is reached), whereas in  $\text{ZrO}_2\text{--B}_2\text{O}_3\text{--Mg--NaCl}$  and  $\text{HfO}_2\text{--B}_2\text{O}_3\text{--Mg--NaCl}$  system, melting of NaCl subtracts energy from the combustion heat, thus decreasing the adiabatic flame temperature.

In summary, it was demonstrated that thermodynamically it is possible to obtain pure  $\text{ZrB}_2$ . To achieve full conversion of oxides to borides in  $\text{ZrO}_2\text{--B}_2\text{O}_3\text{--Mg}$  and  $\text{HfO}_2\text{--B}_2\text{O}_3\text{--Mg}$  systems, the molar ratio should be 1:1:7, which corresponds to 40% excess Mg. The addition of inert

diluents (NaCl and MgO) also lowers the adiabatic flame temperature and aids in the conversion of  $\text{ZrO}_2$  to  $\text{ZrB}_2$ . Note that in the experiments, a usual decrease in the combustion temperature due to heat losses may be a favorable factor for the conversion.

## **4.2. Mechanical Activation**

This section will present and discuss an analysis of the effect of high-energy ball milling on the powder. The first subsection will show particle size distribution of the powders as they come from the supplier. Then, the effect of milling on the powder composition will be discussed. The later subsections will present an analysis on the effects of the inert diluents (MgO and NaCl) on milling.

### **4.2.1. Particle Size Distribution of As-received Powders**

The powders that are used in this research have different particle size distributions. To better understand how high-energy ball milling affect the initial mixture, the particle size distributions of the powders as they come from the supplier are presented below. Figures 4.2.1 to 4.2.5 shows the particle size distributions of  $\text{ZrO}_2$ ,  $\text{B}_2\text{O}_3$ , Mg, MgO, and NaCl, respectively. The distribution of  $\text{ZrO}_2$  is shown to be bimodal with a mean volume diameter of  $15.3\ \mu\text{m}$ . In contrast, the other distributions are unimodal. The mean volume diameters of  $\text{B}_2\text{O}_3$ , Mg, MgO, and NaCl are  $144\ \mu\text{m}$ ,  $15.9\ \mu\text{m}$ ,  $4.5\ \mu\text{m}$ , and  $432.3\ \mu\text{m}$ , respectively. Importantly, these results show that NaCl particles are much larger than MgO, which may influence their effect on milling.

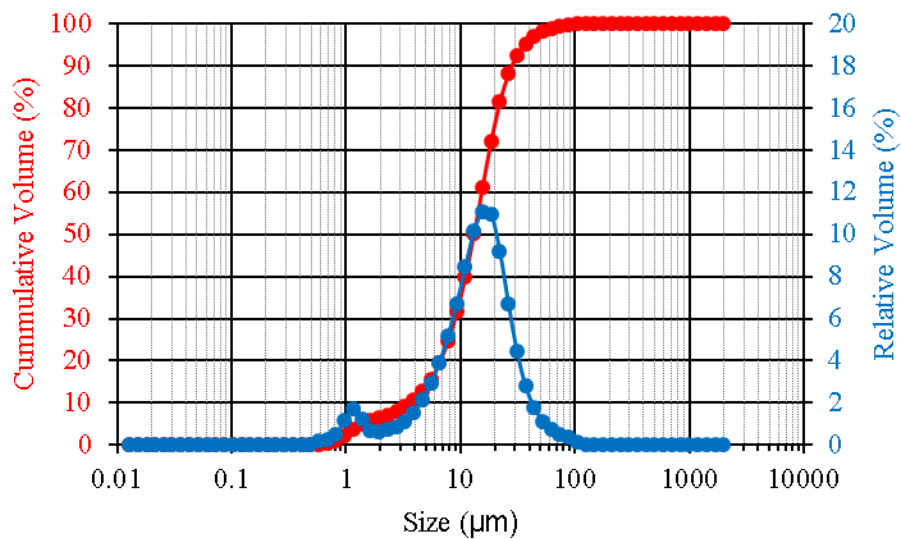


Figure 4.2.1: Particle size distribution of zirconium (IV) oxide (ZrO<sub>2</sub>, -325 mesh, 99.7% pure, Alfa Aesar).

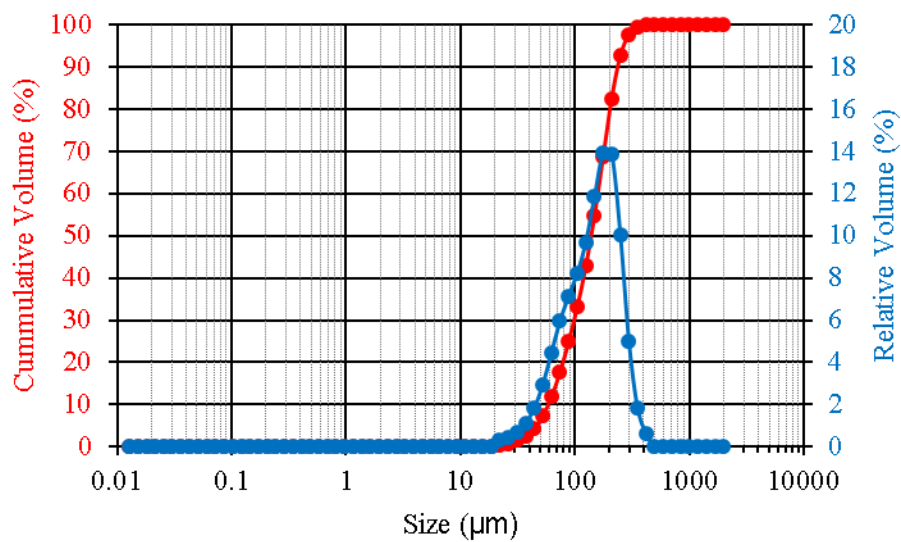


Figure 4.2.2: Particle size distribution of boron trioxide (B<sub>2</sub>O<sub>3</sub>, 99.8% pure, Sigma-Aldrich).

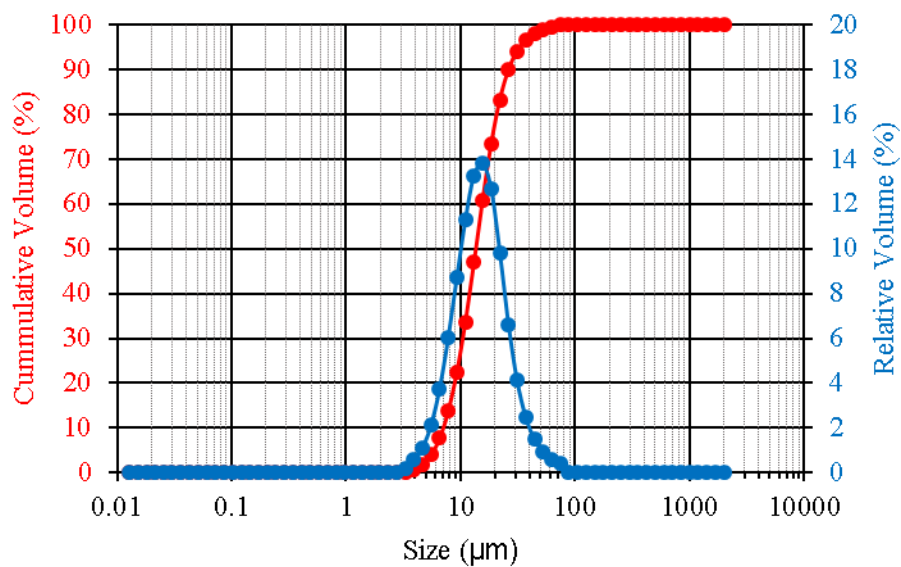


Figure 4.2.3: Particle size distribution of magnesium (Mg, -325 mesh, 99.8% pure, Sigma-Aldrich).

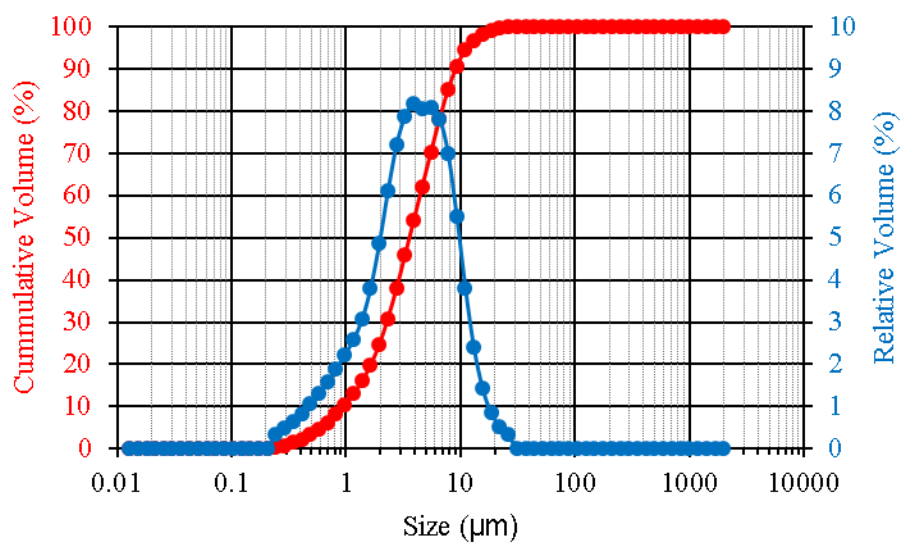


Figure 4.2.4: Particle size distribution of magnesium oxide (MgO, -325 mesh,  $\geq 99\%$  pure, Sigma-Aldrich).

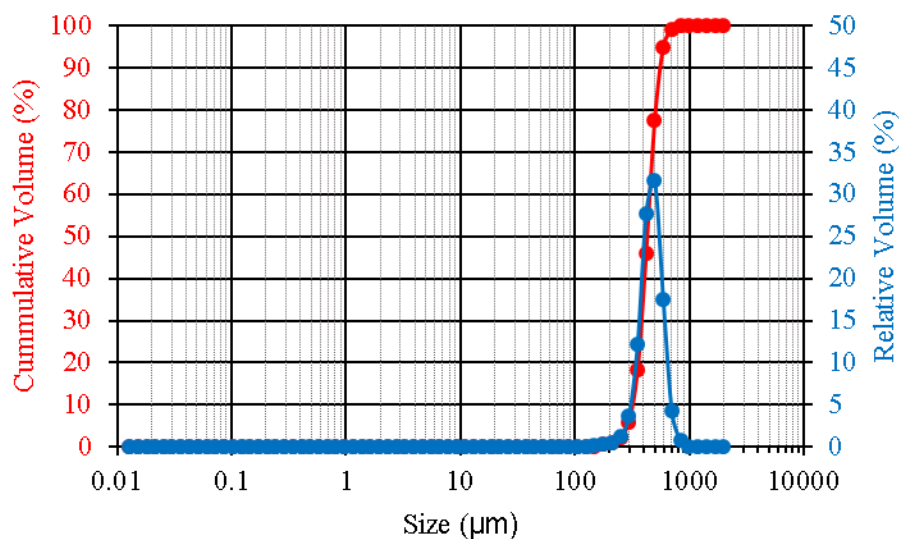


Figure 4.2.5: Particle size distribution of sodium chloride (NaCl, 99% pure, Sigma-Aldrich).

#### 4.2.2. Effect of Milling on Composition

Previous research has shown that metallotermic reduction of  $\text{ZrO}_2$  and  $\text{B}_2\text{O}_3$  can be conducted by mechanochemical processing, specifically, by either mechanical alloying or mechanically induced self-sustaining reactions [51] [17] [19]. In contrast, in mechanical activation-assisted SHS (MASHS), the milling is only conducted for a short-period of time and it is ended before any noticeable reaction can occur inside the grinding bowl. Figure 4.2.6 shows the XRD patterns of the stoichiometric  $\text{ZrO}_2\text{-B}_2\text{O}_3\text{-Mg}$  system after mixing and after high-energy ball milling for 1 minute. The XRD pattern of the milled mixture does not show any traces of  $\text{MgO}$  or  $\text{ZrB}_2$ , i.e., no apparent reaction took place during milling. The pattern shows a small shift in the intensity of magnesium crystal planes (202) and (101) located at  $2\theta = 34.4^\circ$  and  $2\theta = 36.6^\circ$ , respectively. The shift could be caused by changes in the preferential crystal orientation of magnesium after milling. Also, there is a small unidentified peak at  $2\theta = 37.3^\circ$  in the unmilled mixture that vanished after milling.

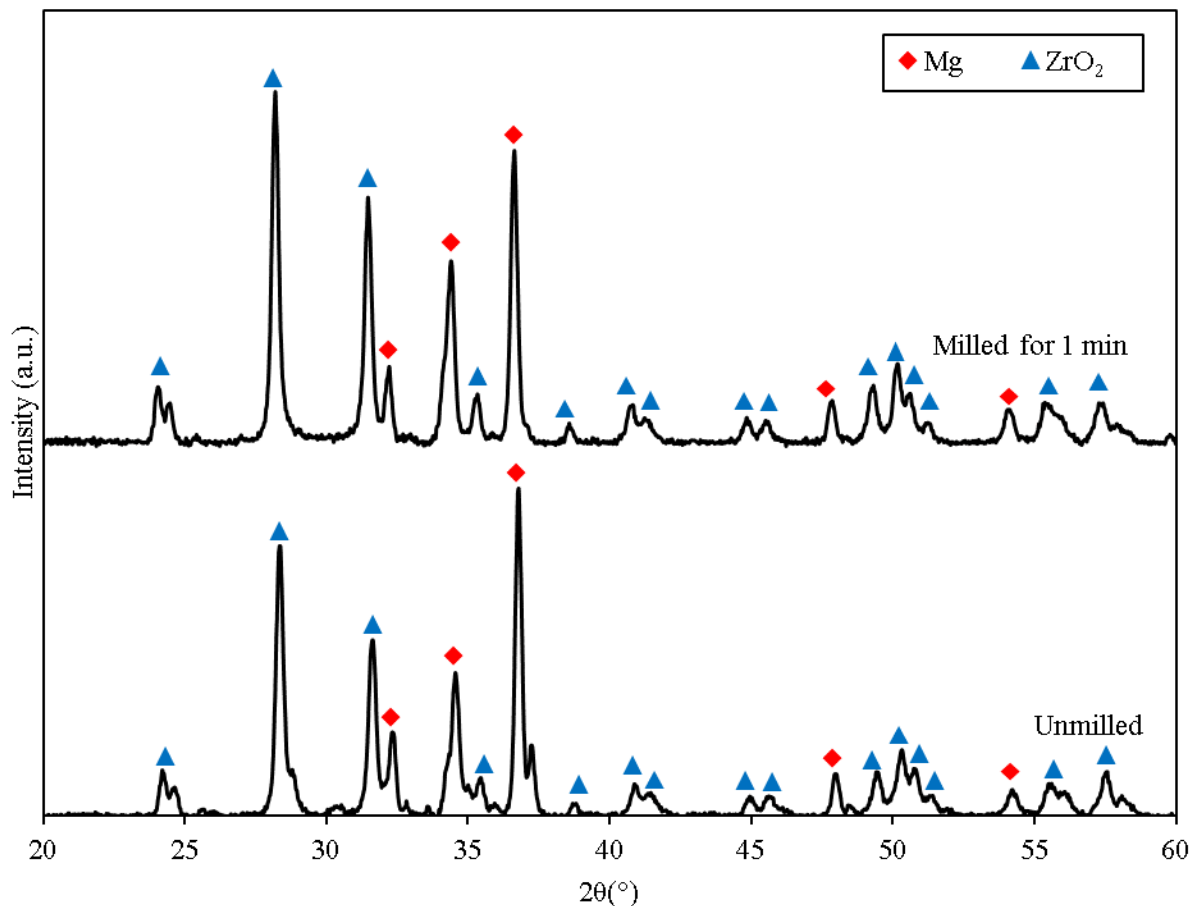


Figure 4.2.6: XRD patterns of stoichiometric  $\text{ZrO}_2\text{-B}_2\text{O}_3\text{-Mg}$  mixture (a) before milling and (b) after milling for 1 minute.

#### 4.2.3. Effect of Magnesium Oxide

After milling the mixture, the recovered mass from the grinding bowl was recorded. In all cases, a large fraction of the initial 15 g was recovered, but a portion of the material stuck to the grinding balls and the interior surface of the bowl. To understand how MgO affects the milling process, the percentage of mixture lost during 1-min milling was plotted vs. MgO concentration in Fig. 4.2.7. It is seen that with no MgO 24% of the mixture was lost, while at 25-40 wt% MgO the mass loss was in the range from 14 to 21%. In summary, magnesium oxide does not facilitate the milling of  $\text{ZrO}_2/\text{B}_2\text{O}_3/\text{Mg}$  mixtures.



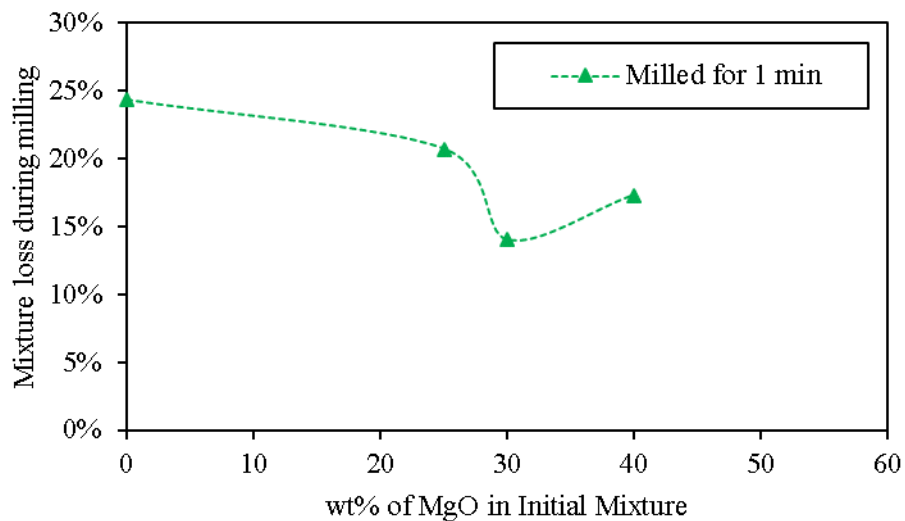


Figure 4.2.7: Percentage of mixture that is lost to the grinding media vs. MgO concentration.

Figures 4.2.8 and 4.2.9 show the particle size distributions of stoichiometric  $\text{ZrO}_2/\text{B}_2\text{O}_3/\text{Mg}/\text{MgO}$  mixtures with 40 wt% MgO, milled for 1 and 10 min, respectively. After milling, the particle size distribution became unimodal. Also, increasing the milling time from 1 to 10 min decreased the mean volume diameter from 42.1 to 20.8  $\mu\text{m}$ .

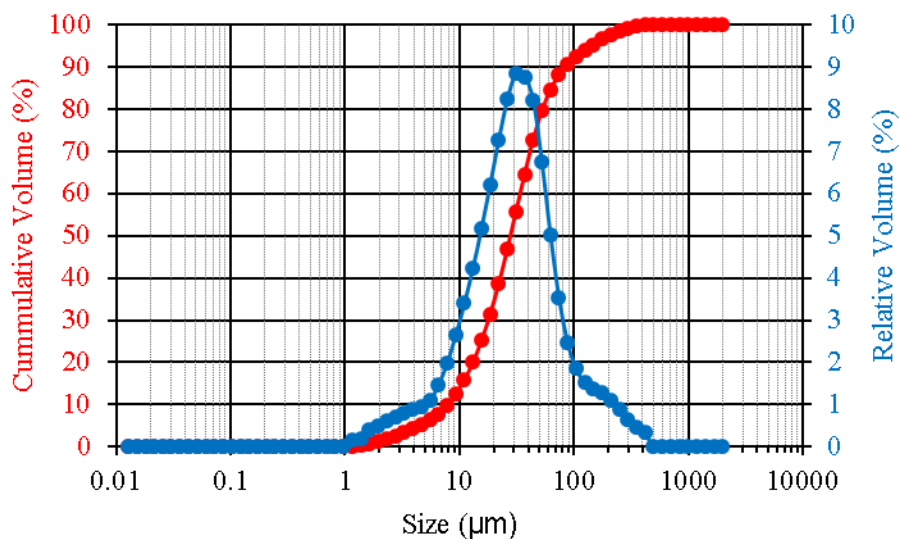


Figure 4.2.8: Particle size distribution of  $\text{ZrO}_2/\text{B}_2\text{O}_3/\text{Mg}$  mixture with 40wt% MgO after milling for 1 min.

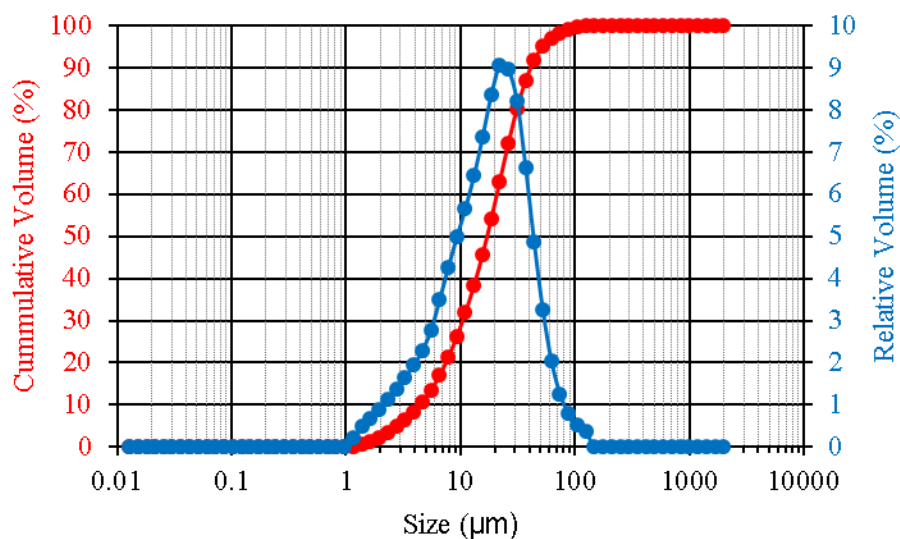


Figure 4.2.9: Particle size distribution of  $\text{ZrO}_2/\text{B}_2\text{O}_3/\text{Mg}$  mixture with 40wt% MgO after milling for 10 min.

#### 4.2.4. Effect of Sodium Chloride

Sodium chloride has been previously used to facilitate milling of soft metals [34]. Therefore, it is expected that NaCl will facilitate the milling of  $\text{ZrO}_2/\text{B}_2\text{O}_3/\text{Mg}$  mixtures. Figure 4.2.10 shows the percentage of mixture that sticks to the grinding media after milling with respect to the content of NaCl and the total milling time. Note that the loss of mixture due to sticking to the grinding media may disrupt the stoichiometry, e.g., magnesium may stick at a higher rate than  $\text{ZrO}_2$ . It is seen that by adding 5-10 wt% of NaCl the amount of lost mixture was significantly reduced, e.g., the amount lost decreased from 24.3% at 0 wt% NaCl to 4.7 % at 10% NaCl. Additionally, for longer total milling times the amount of lost mixture stagnates around 5% when the NaCl content is equal or higher than 40 wt%.

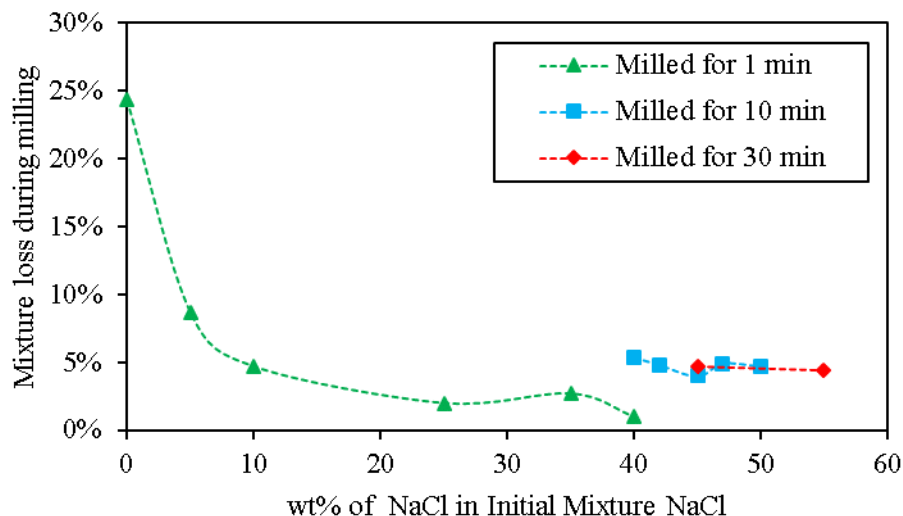


Figure 4.2.10: Percentage of stoichiometric  $\text{ZrO}_2/\text{B}_2\text{O}_3/\text{Mg}$  mixture that is lost to the grinding media vs. NaCl concentration.

The particle size distributions of  $\text{ZrO}_2/\text{B}_2\text{O}_3/\text{Mg}$  mixtures with 40 wt% NaCl milled for 1 and 10 minutes are shown in Fig. 4.2.11 and 4.2.12. For the mixture milled for 1 min, the mean volume diameter is  $30.6 \mu\text{m}$ , but the distribution shows a smaller peak around  $3 \mu\text{m}$ . For the mixture milled for 10 min, the distribution only shows one peak and the mean volume diameter is  $22.8 \mu\text{m}$ .

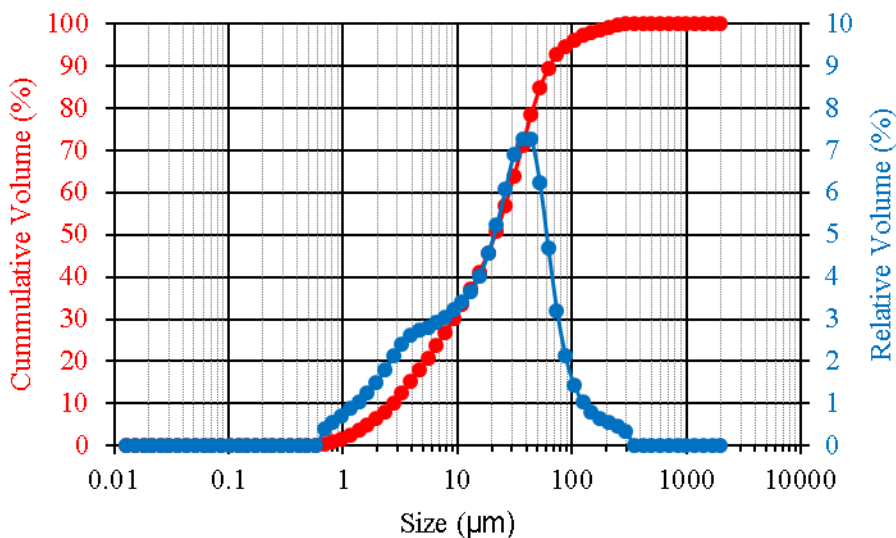


Figure 4.2.11: Particle size distribution of  $\text{ZrO}_2/\text{B}_2\text{O}_3/\text{Mg}$  mixture with 40wt% NaCl after milling for 1 min.

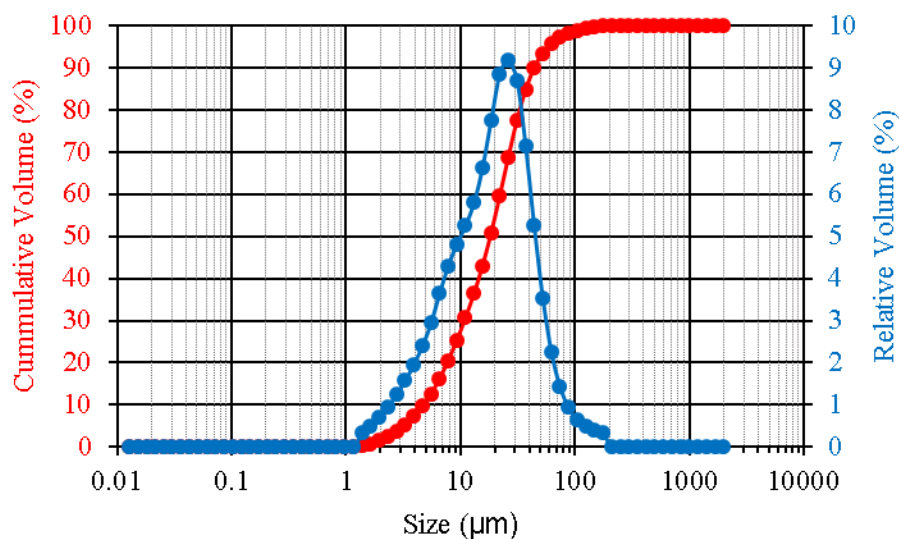


Figure 4.2.12: Particle size distribution of  $\text{ZrO}_2/\text{B}_2\text{O}_3/\text{Mg}$  mixture with 40wt% NaCl after milling for 1 min.

## 4.3. Combustion Experiments

### 4.3.1. Magnesiothermic MASHS of Zirconium Diboride

The stoichiometric  $\text{ZrO}_2/\text{B}_2\text{O}_3/\text{Mg}$  mixture was not ignitable without a preceding milling step, but milling for 1 min enabled the ignition. The combustion process of the stoichiometric  $\text{ZrO}_2/\text{B}_2\text{O}_3/\text{Mg}$  mixture, milled for 1 min, is shown in Fig.4.3.1. The first image ( $t = 0$ ) corresponds to 1.76 s after ignition of the booster pellet. In general, the combustion process was fast and vigorous, and was accompanied by the formation of a layered structure of the product. After combustion, the product was fragile and porous.

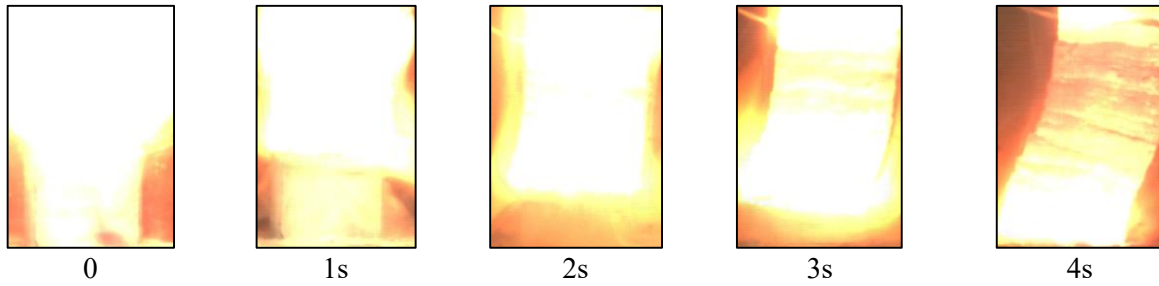


Figure 4.3.1: Combustion propagation over a pellet of stoichiometric  $\text{ZrO}_2\text{-B}_2\text{O}_3\text{-Mg}$  mixture. Time zero was selected 4 s before the end of the combustion process.

Figure 4.3.2 shows the thermocouple recordings for the combustion process shown in Fig. 4.3.1. Since the voltage–temperature characteristic of a C-type thermocouple is strongly non-linear [59], the plot shows the voltage and dashed gridlines indicate temperatures for reference. It is seen that the maximum recorded temperature at the center of the pellet is 1725 °C, which is by 372 °C lower than the adiabatic flame temperature (2097°C) for the same mixture. The temperature difference could be attributed to heat losses and incomplete combustion. The time variation of temperature exhibits a sharp temperature rise followed by a gradual decrease due to cooling.

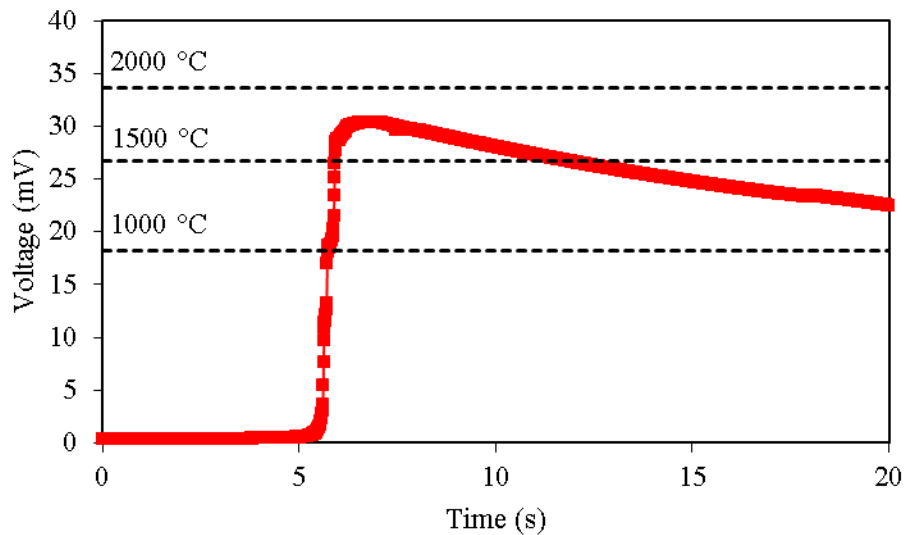


Figure 4.3.2: Thermocouple recording for stoichiometric  $\text{ZrO}_2/\text{B}_2\text{O}_3/\text{Mg}$  mixture. Time zero was selected arbitrarily.

Figure 4.3.3 shows XRD patterns (a) after milling for 1 min, (b) after combustion, and (c) after leaching of the stoichiometric  $\text{ZrO}_2/\text{B}_2\text{O}_3/\text{Mg}$  mixture. It is seen that after combustion the dominant phase is  $\text{ZrB}_2$ . Leaching removed pure  $\text{MgO}$  phase from the products, but there are two impurities: cubic zirconia ( $\text{c-ZrO}_2$ ) and  $\text{Mg}_3(\text{BO}_3)_2$ . Before combustion,  $\text{ZrO}_2$  in the mixture its stable room-temperature phase (monoclinic zirconium oxide,  $\text{m-ZrO}_2$ ), but after combustion, the high-temperature phase  $\text{c-ZrO}_2$  becomes metastable by forming a solid solution with  $\text{MgO}$  at temperatures equal or higher than  $1400^\circ\text{C}$  [60]. Magnesia stabilized zirconia contains around 10 mol%  $\text{MgO}$ , but that value can vary. Although there is unreacted  $\text{ZrO}_2$ , the XRD pattern of the combustion products does not show unreacted  $\text{Mg}$ , which is the result of higher combustion temperature ( $1725^\circ\text{C}$ ) than the boiling point of  $\text{Mg}$  ( $1095^\circ\text{C}$ ).

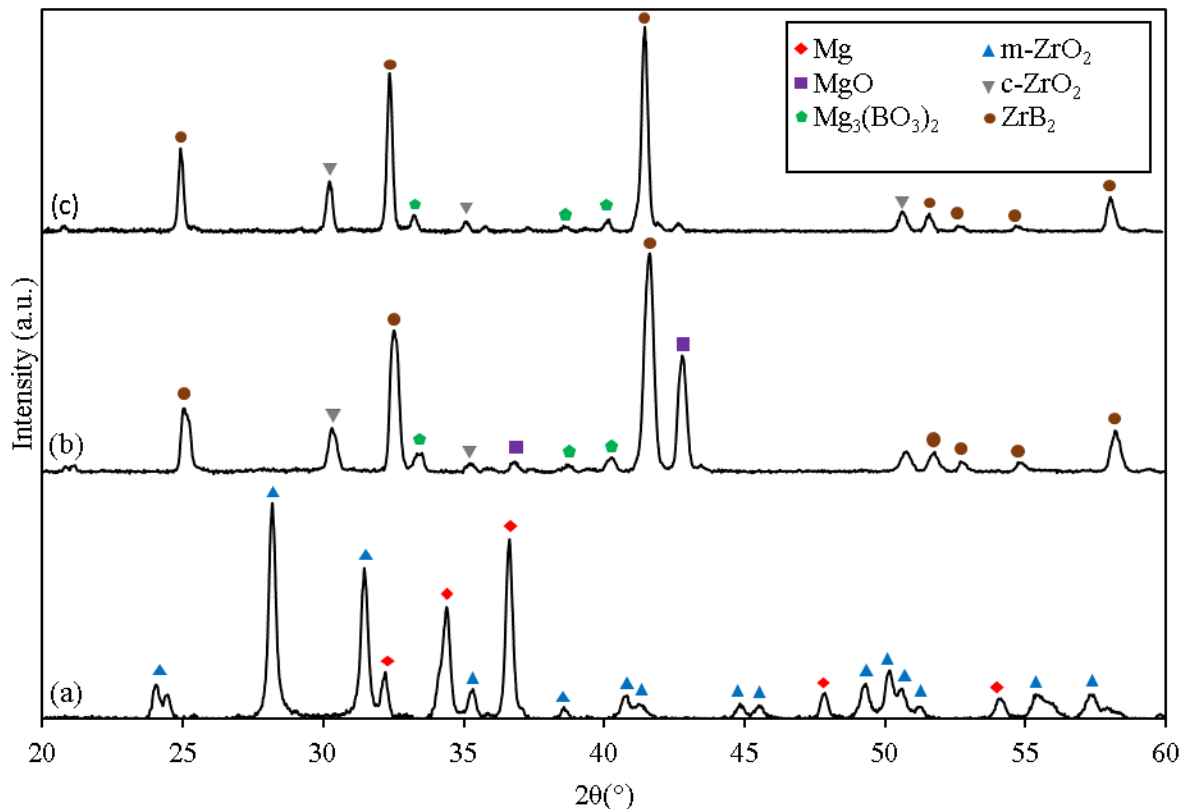


Figure 4.3.3: XRD patterns of stoichiometric  $\text{ZrO}_2/\text{B}_2\text{O}_3/\text{Mg}$  mixture (a) after milling for 1 min, (b) after combustion, and (c) after leaching.

#### 4.3.1.1. Effect of Magnesium Oxide

Combustion experiments of the stoichiometric  $\text{ZrO}_2/\text{B}_2\text{O}_3/\text{Mg}/\text{MgO}$  mixtures were conducted in MgO concentration range of 20 to 40 wt%. Two total milling times were used for the mechanical activation step: 1 and 10 min. Figure 4.3.4 shows the combustion of  $\text{ZrO}_2/\text{B}_2\text{O}_3/\text{Mg}/\text{MgO}$  mixtures. In general, it was more difficult to ignite  $\text{ZrO}_2/\text{B}_2\text{O}_3/\text{Mg}/\text{MgO}$  mixtures that were milled for 1 min than those that were milled for 10 min. No oscillations in the combustion front propagation were observed. However, 30 wt% MgO was the maximum concentration of this diluent that allowed a self-sustained reaction for mixtures that were milled for 1 min (see the top images in Fig. 4.3.4), whereas mixtures that were milled for 10 min were easily ignited even at 40 wt% MgO, as shown in the bottom images of that figure. Similarly to the observations for combustion of stoichiometric mixtures without any inert diluent, the combustion products were fragile and porous.

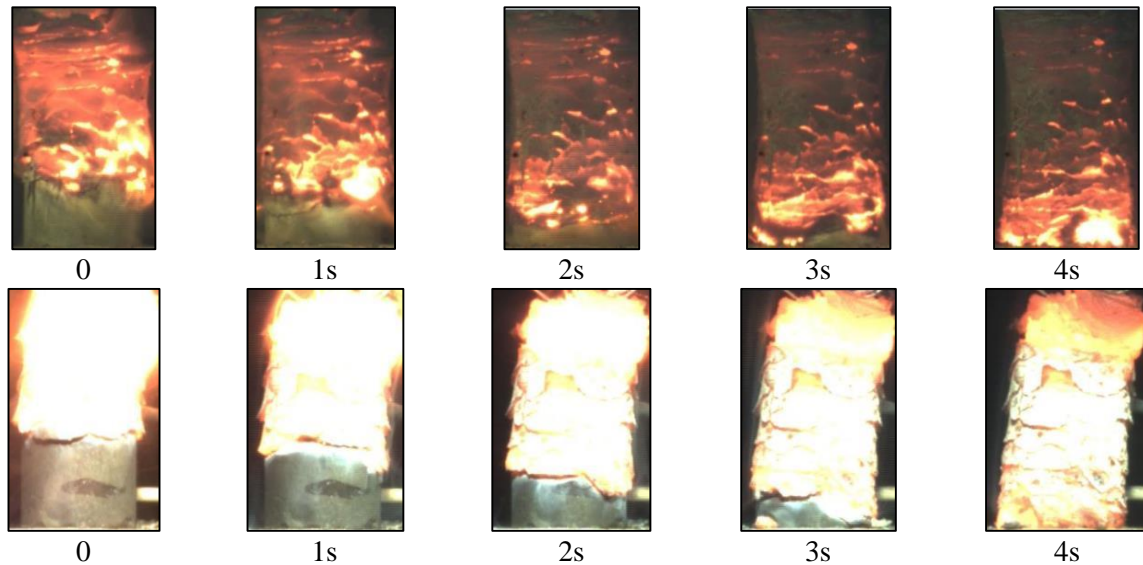


Figure 4.3.4: Combustion propagation over a pellet of stoichiometric  $\text{ZrO}_2/\text{B}_2\text{O}_3/\text{Mg}/\text{MgO}$  mixtures. The top images are for 30 wt% MgO and 1 min milling, the bottom images are for 40 wt% MgO and 10 min milling. Time zero was selected 4 s before the end of the combustion process.

The XRD patterns of the stoichiometric  $\text{ZrO}_2/\text{B}_2\text{O}_3/\text{Mg}/\text{MgO}$  mixture with 40 wt% MgO after milling for 1 min (a), after combustion (b), and after leaching (c) are shown in Fig. 4.3.5. It is seen that after combustion,  $\text{ZrB}_2$  and MgO are the dominant phases, but  $\text{ZrO}_2$  and  $\text{Mg}_3(\text{BO}_3)_2$  are present in the products. Note that because of the lower combustion temperatures when MgO is added to the mixtures,  $\text{ZrO}_2$  was encountered in two phases, monoclinic and cubic. After combustion, Mg was not detected by XRD. The peaks of MgO pattern after milling are broad, which indicate a small crystallite size, but after combustion MgO peaks become sharper, due to a possible increase of the grains. After leaching, most of the MgO was dissolved, however, a small peak is visible in the XRD pattern. Also, the peaks of  $\text{ZrB}_2$  pattern are broader than those observed in the combustion products of the stoichiometric mixture without diluent (Fig. 4.3.3). This observation indicates that MgO could prevent the growth of  $\text{ZrB}_2$  grains during combustion.



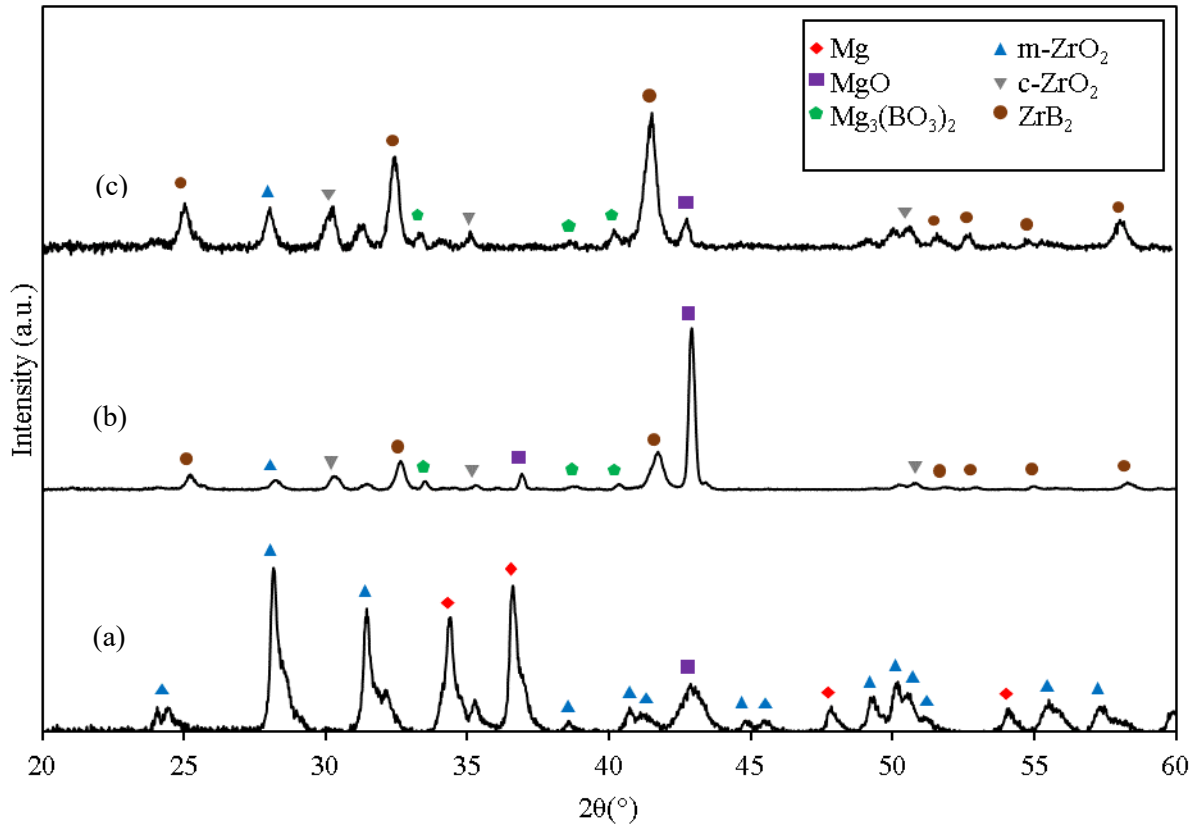


Figure 4.3.5: XRD patterns of stoichiometric  $\text{ZrO}_2/\text{B}_2\text{O}_3/\text{Mg}$  mixture with 40wt% MgO (a) after milling for 10 min, (b) after combustion, and (c) after leaching.

To explore the effect of MgO as an additive in the conversion of  $\text{ZrO}_2$  to  $\text{ZrB}_2$ , the XRD patterns of the combustion products were analyzed. The highest peak for m- $\text{ZrO}_2$  (plane  $(\bar{1}11)$ ,  $2\theta = 28.2^\circ$ ), c- $\text{ZrO}_2$  (plane  $(111)$ ,  $2\theta = 30.5^\circ$ ), and  $\text{ZrB}_2$  (plane  $(101)$ ,  $2\theta = 41.6^\circ$ ) phases was considered in the analysis. The peak intensity ratio of  $\text{ZrO}_2$  peaks (for each phase) to peak of  $\text{ZrB}_2$  were determined and served for characterization of the oxide-to-boride conversion degree (A value 0 in the ratio corresponds to full conversion). Figure 4.3.6 shows the calculated peak intensity ratio of each  $\text{ZrO}_2$  phase vs. MgO concentration. It is seen that at 0 wt% MgO, the ratio for monoclinic zirconia is 0, but the ratio of cubic zirconia is around 0.2. Note that 0 wt% MgO corresponds to the XRD pattern shown in Fig. 4.3.3. With increasing MgO content, the m- $\text{ZrO}_2$  increases

exponentially. Cubic  $\text{ZrO}_2$  increases from 0 to 20 wt% MgO, and it remains approximately constant from 20 to 30 wt%. In general, these results indicate that MgO has an adverse effect on the conversion of oxides to borides.

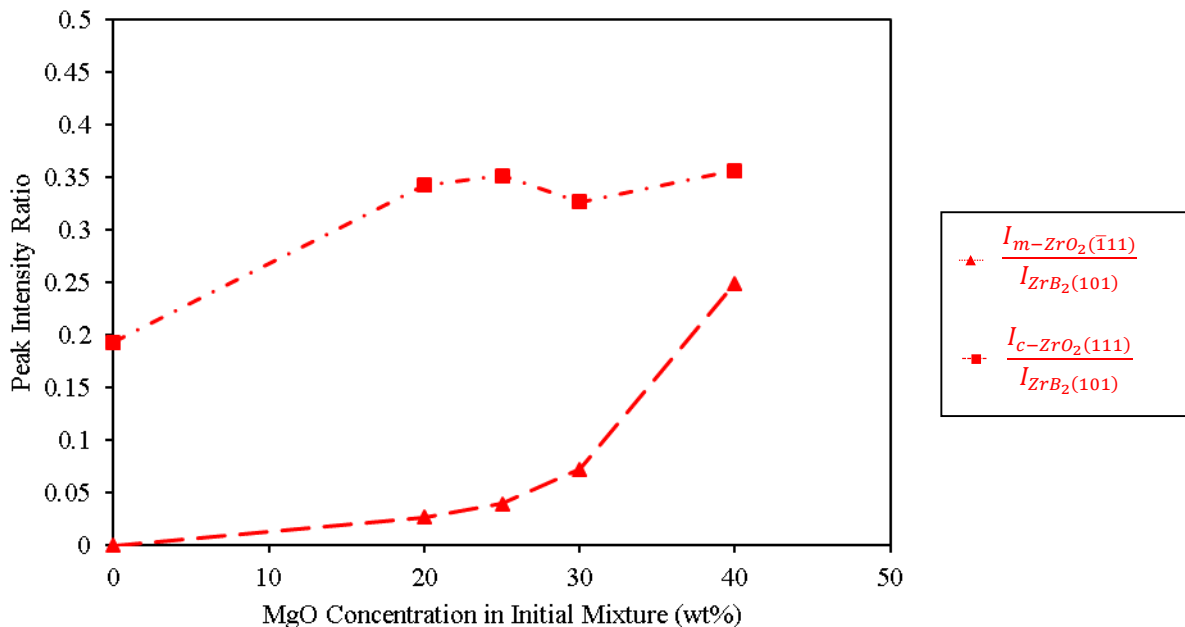


Figure 4.3.6: Intensity ratios of the m- $\text{ZrO}_2$  and c- $\text{ZrO}_2$  XRD peaks (planes  $\bar{1}11$  and  $111$ ) to the  $\text{ZrB}_2$  peak (plane 101) vs. MgO concentration in the initial mixture with the stoichiometric ( $\text{ZrO}_2:\text{B}_2\text{O}_3:\text{Mg} = 1:1:5$ ) composition.

#### 4.3.1.2. Effect of Sodium Chloride

Stoichiometric  $\text{ZrO}_2/\text{B}_2\text{O}_3/\text{Mg}/\text{NaCl}$  mixtures were ignited in NaCl concentration range of 5 to 55 wt%. After milling for 1 minute, the mixtures with up to 35 wt% NaCl became ignitable, but the mixtures with 35-50 wt% NaCl required 10 minutes of milling for combustion to occur. To ignite mixtures with more than 50 wt% NaCl, the required milling time was 30 minutes. Figure 4.3.7 shows the combustion process of the stoichiometric  $\text{ZrO}_2\text{-B}_2\text{O}_3\text{-Mg-NaCl}$  mixture milled for 10 min with 47 wt% NaCl. It is seen that the combustion front moves steadily and has a uniform structure. This was observed for all samples milled for 10 minutes with NaCl, but for the samples milled for 1 minute with NaCl, the combustion front was oscillatory. After cooling down, the

products were dense and hard, due to melting of NaCl during combustion and subsequent solidification after the temperature drop.

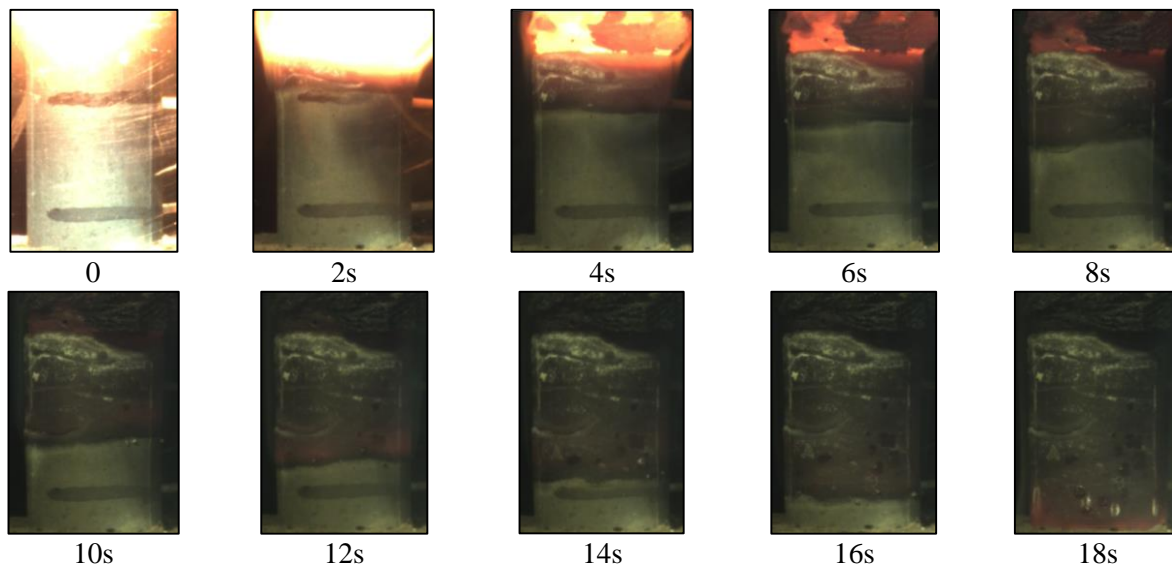


Figure 4.3.7: Combustion propagation over a pellet of stoichiometric  $\text{ZrO}_2/\text{B}_2\text{O}_3/\text{Mg}/\text{NaCl}$  mixture with 47wt% NaCl. Time zero was selected arbitrarily.

The C-type thermocouple recordings of the combustion process of the stoichiometric  $\text{ZrO}_2/\text{B}_2\text{O}_3/\text{Mg}$  mixture with 47 wt% NaCl are shown in Fig.4.3.8. This record corresponds to the experiment shown above (Fig. 4.3.7). It is seen that the maximum recorded temperatures are about the same (approx. 1200 °C) for both thermocouples. In all samples, the time variation of temperature follows the same profile: a sharp temperature rise as the wave front reaches the thermocouple followed by a gradual cooling down. The combustion front velocity is determined from the time lag between the temperature rises of the two thermocouples, which is the time that takes the front to travel 10 mm.

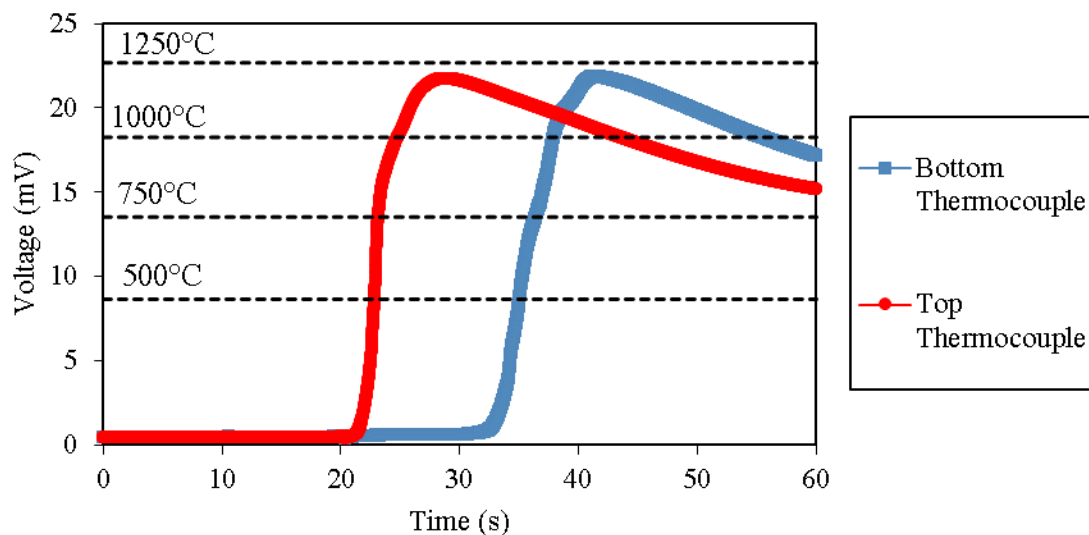


Figure 4.3.8: Thermocouples recordings for stoichiometric  $\text{ZrO}_2/\text{B}_2\text{O}_3/\text{Mg}/\text{NaCl}$  mixture with 47 wt% NaCl. Time zero was selected arbitrarily.

Figure 4.3.9 shows the combustion front velocity with respect to NaCl concentration for stoichiometric  $\text{ZrO}_2/\text{B}_2\text{O}_3/\text{Mg}/\text{NaCl}$  mixtures milled for 10 minutes. The velocities are in the range of 0.6 to 2.6 mm/s. It is observed that the front velocity decreases with increasing the concentration of NaCl.

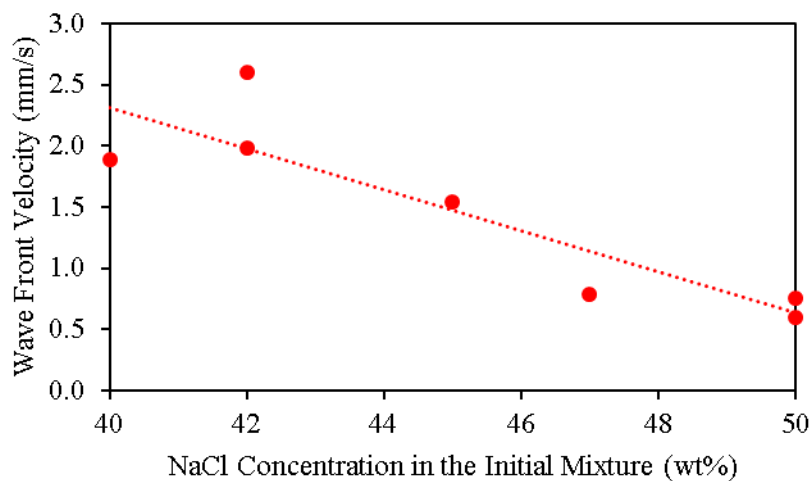


Figure 4.3.9: Combustion front velocity vs. NaCl concentration in the initial mixture.

The XRD pattern of the combustion products of stoichiometric  $\text{ZrO}_2/\text{B}_2\text{O}_3/\text{Mg}/\text{NaCl}$  mixture with 40 wt% NaCl milled for 10 minutes is shown in 4.3.10. It is observed that  $\text{ZrB}_2$  is the most prominent phase. The impurities found in the products were  $\text{Mg}_3(\text{BO}_3)_2$ , m- $\text{ZrO}_2$ , and c- $\text{ZrO}_2$ .

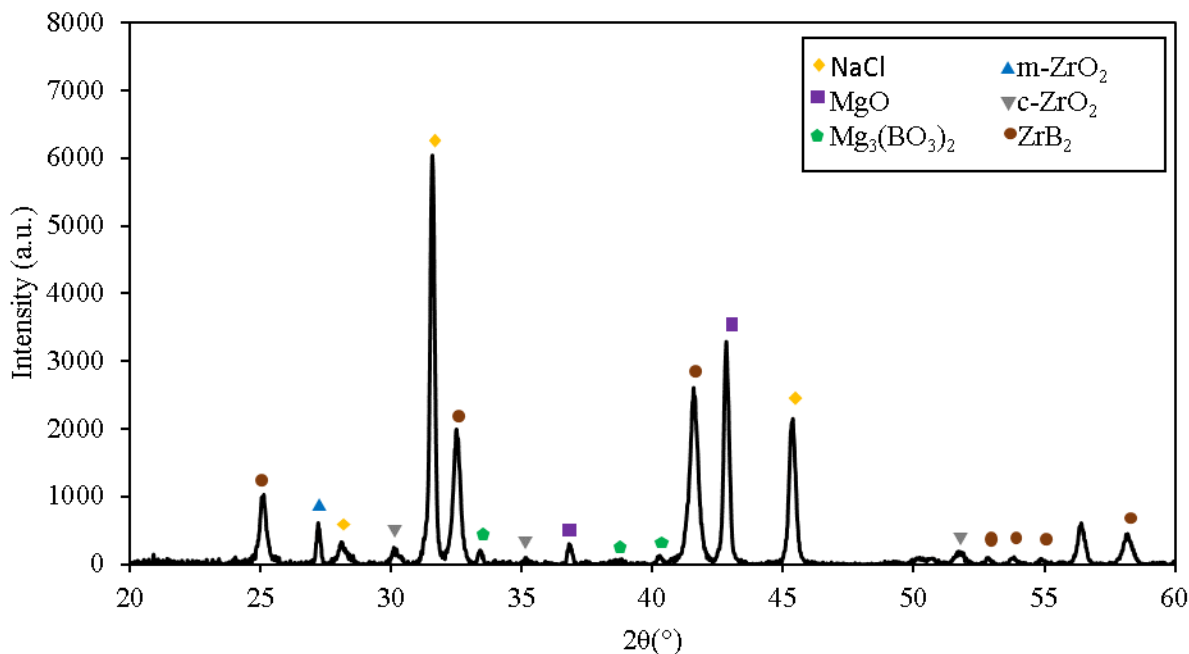


Figure 4.3.10: XRD pattern of stoichiometric  $\text{ZrO}_2/\text{B}_2\text{O}_3/\text{Mg}$  mixture with 40wt% NaCl after combustion.

As in the  $\text{ZrO}_2/\text{B}_2\text{O}_3/\text{Mg}/\text{MgO}$  system experiments (topic 4.3.1.1), the XRD peak ratio analysis was conducted for the  $\text{ZrO}_2/\text{B}_2\text{O}_3/\text{Mg}/\text{NaCl}$  system. The determined peak intensities ratios for both  $\text{ZrO}_2$  phases with respect to  $\text{ZrB}_2$  and maximum measured temperatures vs. NaCl concentration are shown in Fig. 4.3.11. It is seen that with increasing NaCl concentration, the peak intensity ratio of monoclinic  $\text{ZrO}_2$  (plane  $(\bar{1}11)$ ,  $2\theta = 28.2^\circ$ ) gradually increases, whereas that of the cubic  $\text{ZrO}_2$  phase (plane  $(111)$ ,  $2\theta = 30.5^\circ$ ) decreases. At the same time, the increase in NaCl content decreases the combustion temperature. The  $\text{ZrO}_2$ - $\text{MgO}$  phase diagram shows that monoclinic  $\text{ZrO}_2$  forms at lower temperatures, while the cubic  $\text{ZrO}_2$  phase forms at higher temperatures [60]. Thus, the obtained results are in good agreement with the phase diagram.

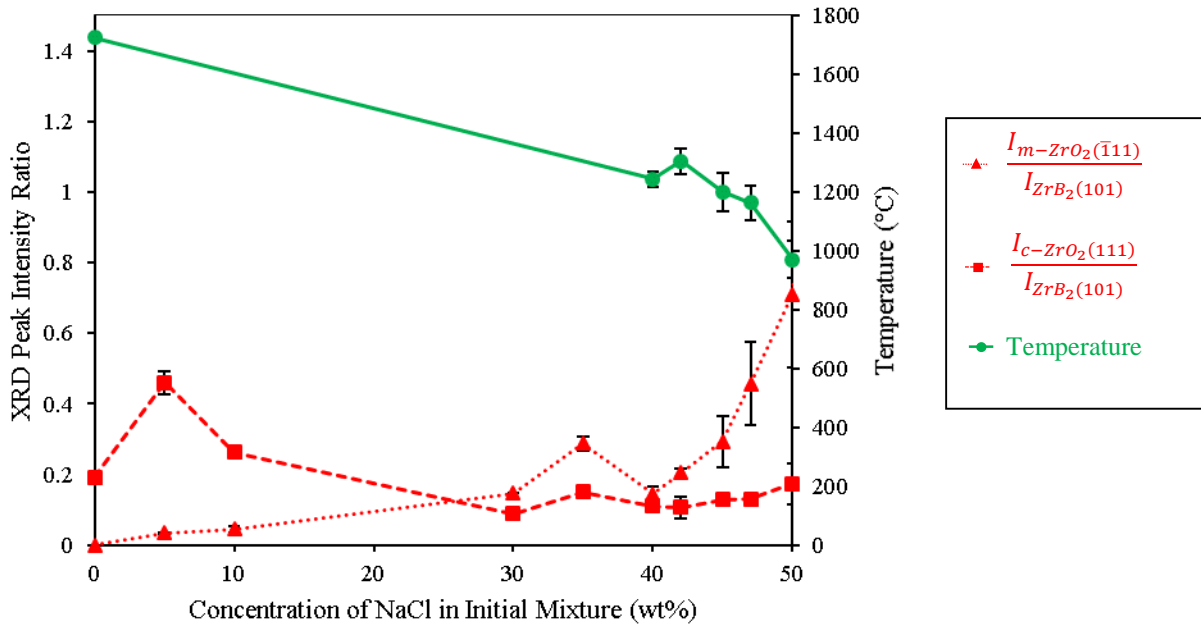


Figure 4.3.11: Intensity ratios of the m-ZrO<sub>2</sub> and c-ZrO<sub>2</sub> XRD peaks (planes  $\bar{1}11$ ) and (111)) to the ZrB<sub>2</sub> peak (plane 101) and maximum recorded temperature vs. NaCl concentration in the initial mixture with the stoichiometric (ZrO<sub>2</sub>:B<sub>2</sub>O<sub>3</sub>:Mg = 1:1:5) composition.

Figure 4.3.12 shows the scanning electron microscopy (SEM) images of the leached combustion products of stoichiometric ZrO<sub>2</sub>/B<sub>2</sub>O<sub>3</sub>/Mg mixture (a) with no NaCl and (b) with 30wt% NaCl. The magnification in both images is 30 k. It is seen that the particle size of the leached combustion products with no inert diluent is much larger than that of the leached products of the mixtures with 30 wt% NaCl. The effect of NaCl on particle size was previously reported [15] [61]. Note that a smaller particle size usually leads to a lower sintering temperature, which is highly desired [62] [63].

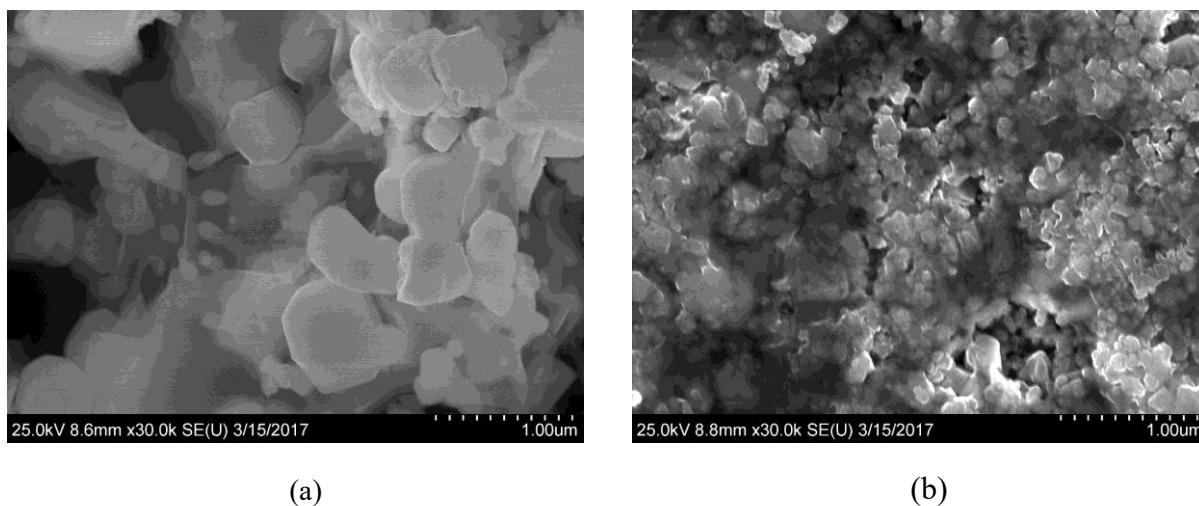


Figure 4.3.12: Scanning electron microscopy images of the leached combustion products of stoichiometric  $\text{ZrO}_2/\text{B}_2\text{O}_3/\text{Mg}$  mixture (a) with no NaCl and (b) with 30 wt% NaCl.

#### 4.3.1.3. Effect of Excess Magnesium

Since in all the experiments conducted with the stoichiometric  $\text{ZrO}_2\text{-B}_2\text{O}_3\text{-Mg}$  mixtures with and without diluents, unreacted  $\text{ZrO}_2$  was encountered in the products, it has been hypothesized that adding extra Mg could further reduce the oxides. Combustion experiments of  $\text{ZrO}_2:\text{B}_2\text{O}_3:\text{Mg} = 1:1:6$  (20% excess Mg) were conducted with 10 to 40 wt% NaCl. To ignite, the mixtures required 5 minutes of milling. Figure 4.3.13 shows the calculated peak intensity ratio of the  $\text{ZrO}_2$  phases and maximum measured temperatures vs. NaCl concentration for the  $\text{ZrO}_2:\text{B}_2\text{O}_3:\text{Mg} = 1:1:6$  system. Also, the stoichiometric mixture results ( $\text{ZrO}_2:\text{B}_2\text{O}_3:\text{Mg} = 1:1:5$ ), which are also shown in Fig. 4.3.11, are included in Fig. 4.3.13 for reference. The peak intensity ratio for c- $\text{ZrO}_2$  initially increases from 10 to 20% NaCl, but then decreases from 20 to 30 wt% NaCl and remains approximately constant from 30 to 40 wt%. The m- $\text{ZrO}_2$  peak intensity ratio increases gradually from 10 to 40 wt% NaCl. The temperature measurements during combustion of mixtures with 20% excess Mg provided unclear results. Apparently, the observed drop in the

temperature at 30 wt% NaCl was caused by an experimental error. In general, the conversion for the experiments with 20% excess Mg appears to be better than that for the stoichiometric mixture.

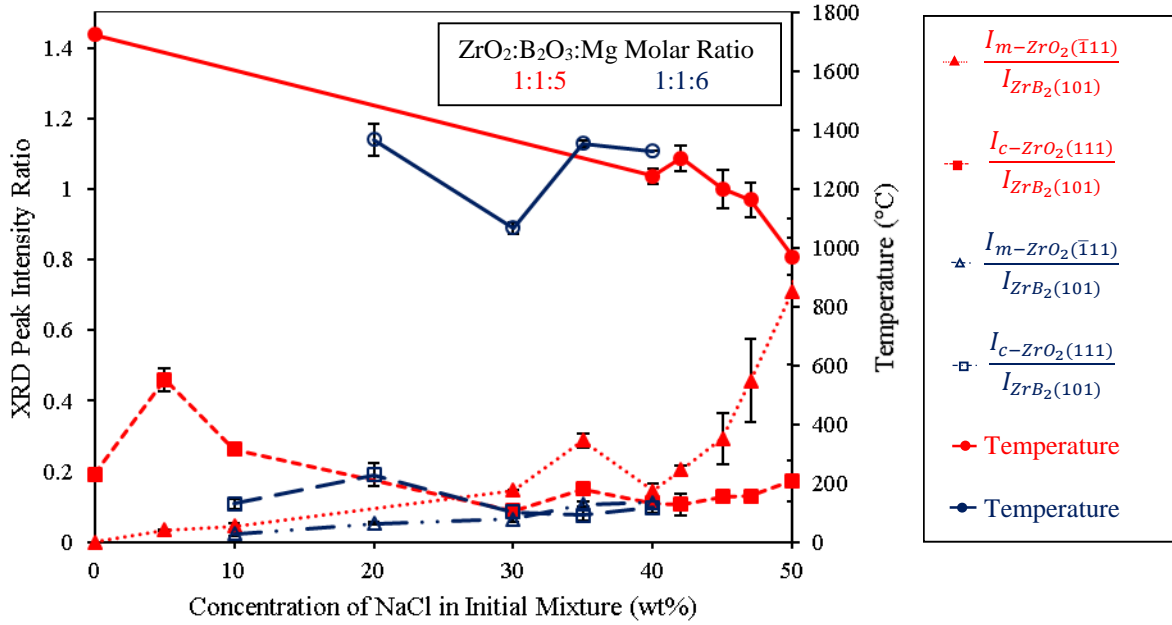


Figure 4.3.13: Intensity ratios of the m-ZrO<sub>2</sub> and c-ZrO<sub>2</sub> XRD peaks (planes  $\bar{1}11$ ) and (111)) to the ZrB<sub>2</sub> peak (plane 101) and maximum recorded temperature vs. NaCl concentration in the initial mixture with the ZrO<sub>2</sub>:B<sub>2</sub>O<sub>3</sub>:Mg = 1:1:5 and ZrO<sub>2</sub>:B<sub>2</sub>O<sub>3</sub>:Mg = 1:1:6 compositions.

Figure 4.3.14 shows a SEM image of the leached products of ZrO<sub>2</sub>/B<sub>2</sub>O<sub>3</sub>/Mg mixture with 20% excess Mg and 30 wt% NaCl (magnification: 180k). The image shows that the obtained ZrB<sub>2</sub> powder is composed of nanoscale polycrystalline particles. Note that polycrystalline particles sinter faster than single-crystal particles [64].



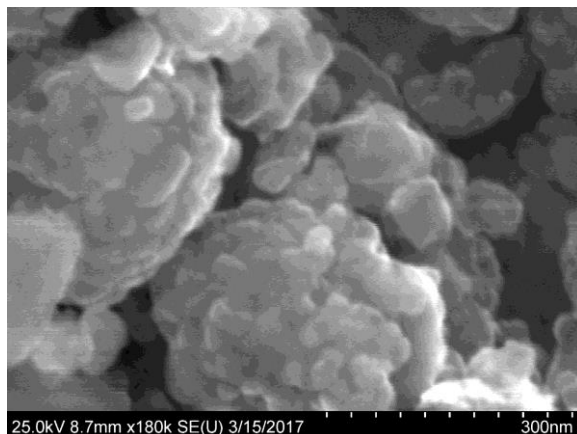


Figure 4.3.14: Scanning electron microscopy images of the combustion products of stoichiometric  $\text{ZrO}_2/\text{B}_2\text{O}_3/\text{Mg}$  mixture with 20% excess Mg and 30 wt% NaCl.

#### 4.3.1.4. *Effect of Leaching on the Products*

Figure 4.3.15 shows the XRD pattern of the leached products for  $\text{ZrO}_2/\text{B}_2\text{O}_3/\text{Mg}/\text{NaCl}$  mixture with 20% excess Mg and 30 wt% NaCl. It is seen that  $\text{MgO}$  and  $\text{Mg}_3(\text{BO}_3)_2$  were fully removed from the products. However, in the products obtained by combustion of  $\text{ZrO}_2/\text{B}_2\text{O}_3/\text{Mg}$  and  $\text{ZrO}_2/\text{B}_2\text{O}_3/\text{Mg}/\text{MgO}$  mixtures,  $\text{MgO}$  and  $\text{Mg}_3(\text{BO}_3)_2$  were only partially dissolved. This could happen because the total mass of  $\text{MgO}$  in the  $\text{ZrO}_2/\text{B}_2\text{O}_3/\text{Mg}$  and  $\text{ZrO}_2/\text{B}_2\text{O}_3/\text{Mg}/\text{MgO}$  mixtures was higher than in the  $\text{ZrO}_2/\text{B}_2\text{O}_3/\text{Mg}/\text{NaCl}$  mixture, and the total used volume of 1M HCl in the leaching process was the same for all mixtures.

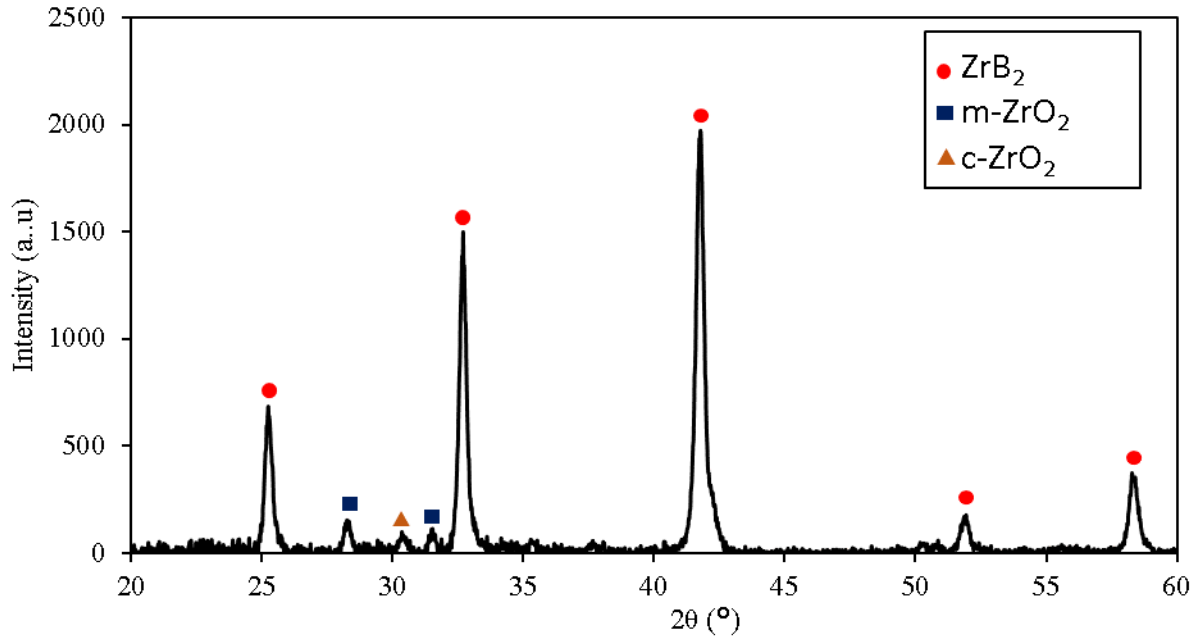


Figure 4.3.15: XRD pattern of stoichiometric  $\text{ZrO}_2/\text{B}_2\text{O}_3/\text{Mg}$  mixture with 30wt% NaCl after leaching.

It was previously reported that leaching may corrode  $\text{ZrB}_2$ , thus increasing the content of  $\text{ZrO}_2$  [18]. To explore the effect of leaching and NaCl concentration on the combustion products, the peak intensity analysis of m- $\text{ZrO}_2$  (plane  $(\bar{1}11)$ ,  $2\theta = 28.2^\circ$ ) and c- $\text{ZrO}_2$  (plane  $(111)$ ,  $2\theta = 30.5^\circ$ ) to  $\text{ZrB}_2$  (plane  $(101)$ ,  $2\theta = 41.6^\circ$ ) was conducted for the leached products of stoichiometric mixture ( $\text{ZrO}_2:\text{B}_2\text{O}_3:\text{Mg} = 1:1:5$ ) and the mixture with 20% excess Mg ( $\text{ZrO}_2:\text{B}_2\text{O}_3:\text{Mg} = 1:1:7$ ). Figure 4.3.16 shows the peak ratios of both  $\text{ZrO}_2$  phases and the maximum recorded temperature vs. NaCl concentration for the combustion products before and after leaching. It is seen that after leaching, m- $\text{ZrO}_2$  (plane  $(\bar{1}11)$ ) peak intensity ratio gradually increases with increasing NaCl concentration from 0 to 35 wt%, then decreases, and after 40 wt% increases sharply. This increase indicates that  $\text{ZrB}_2$  is oxidized during leaching. Since NaCl prevents particle growth, in products

with larger NaCl concentrations the smaller particle size may accelerate the  $\text{ZrB}_2$  oxidation rate. However, the c- $\text{ZrO}_2$  phase intensity remains practically unchanged.

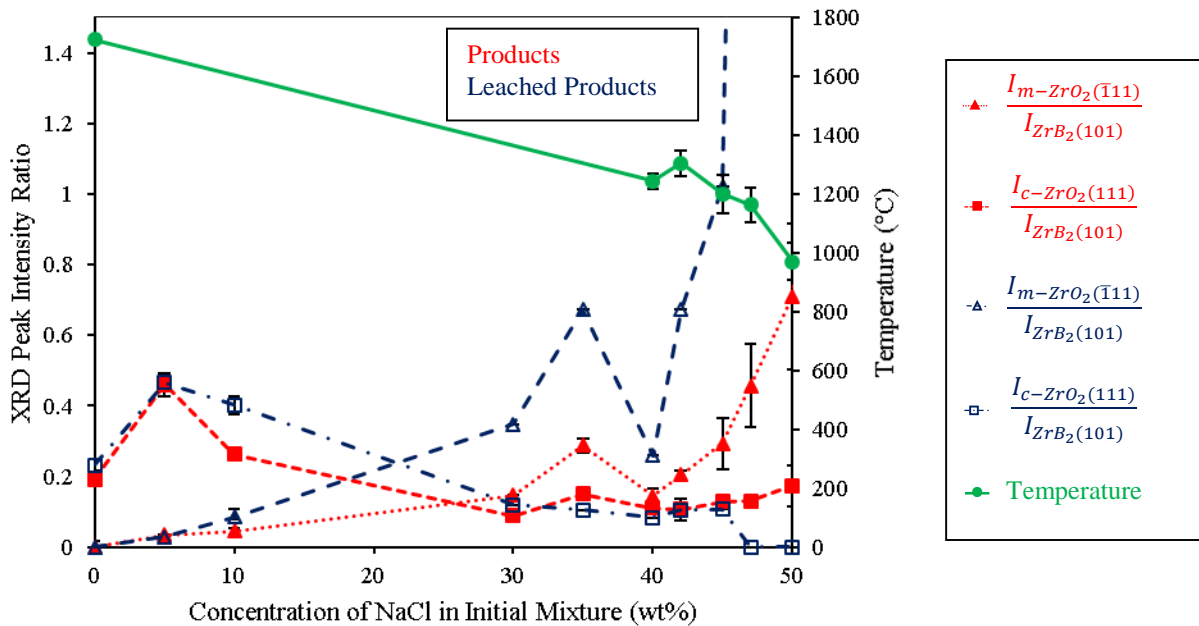


Figure 4.3.16: Intensity ratios of the m- $\text{ZrO}_2$  and c- $\text{ZrO}_2$  XRD peaks (planes  $\bar{1}11$  and  $111$ ) to the  $\text{ZrB}_2$  peak (plane 101) and maximum recorded temperature vs. NaCl concentration in the initial mixture with the stoichiometric ( $\text{ZrO}_2\text{:B}_2\text{O}_3\text{:Mg} = 1\text{:}1\text{:}5$ ) composition, before and after leaching.

Figure 4.3.17 shows the results for the products obtained by combustion of mixtures with 20% excess Mg ( $\text{ZrO}_2\text{:B}_2\text{O}_3\text{:Mg} = 1\text{:}1\text{:}6$ ). Like in the stoichiometric experiments, the content of m- $\text{ZrO}$  phase increases after leaching, which indicates oxidation of  $\text{ZrB}_2$ . Also, the content of m- $\text{ZrO}_2$  phase increases with increasing NaCl concentration. Leaching, however, does not affect c- $\text{ZrO}_2$  peak intensity ratio.

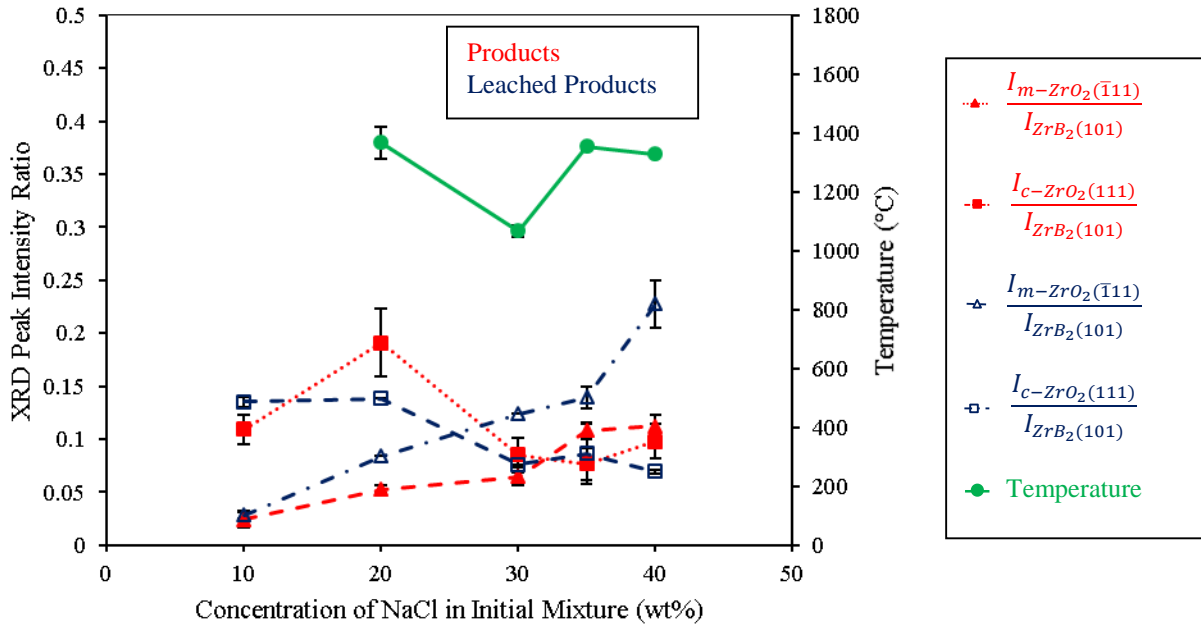


Figure 4.3.17: Intensity ratios of the m-ZrO<sub>2</sub> and c-ZrO<sub>2</sub> XRD peaks (planes  $\bar{1}11$ ) and (111)) to the ZrB<sub>2</sub> peak (plane 101) and maximum recorded temperature vs. NaCl concentration in the initial mixture with the ZrO<sub>2</sub>:B<sub>2</sub>O<sub>3</sub>:Mg = 1:1:6 composition, before and after leaching.

#### 4.3.2. Magnesiothermic MASHS of Hafnium Diboride

Preliminary results of studies on magnesiothermic MASHS of hafnium diboride were obtained. Figure 4.3.18 shows the XRD pattern of the combustion products of HfO<sub>2</sub>:B<sub>2</sub>O<sub>3</sub>:Mg = 1:1:5 mixture with 30 wt% NaCl. Similarly to the results obtained with ZrO<sub>2</sub>, the main phase in the products is HfB<sub>2</sub>, but HfO<sub>2</sub> and Mg<sub>3</sub>(BO<sub>3</sub>)<sub>2</sub> are found as impurities. It is expected that adding excess Mg could improve the conversion of HfO<sub>2</sub> and B<sub>2</sub>O<sub>3</sub> to HfB<sub>2</sub>.

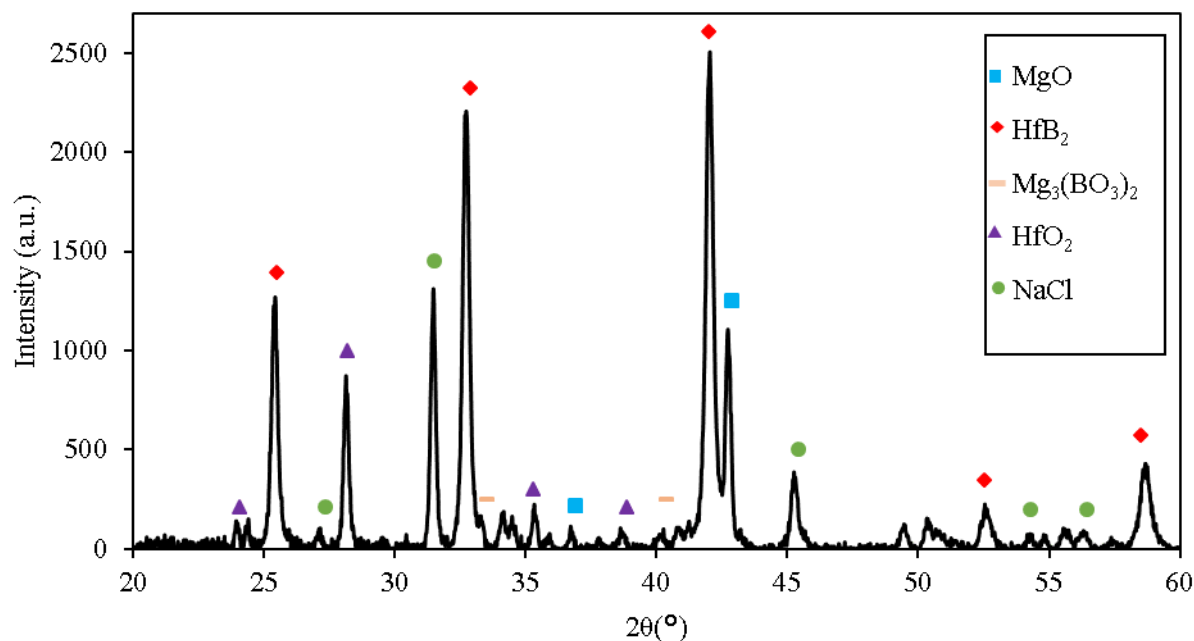


Figure 4.3.18: XRD pattern of stoichiometric  $\text{HfO}_2/\text{B}_2\text{O}_3/\text{Mg}$  mixture with 30 wt% NaCl after combustion.

#### 4.3.3. Magnesiothermic MASHS of Zirconium Diboride and Hafnium Diboride Composites

Previously, it has been demonstrated that solid solutions of  $\text{ZrB}_2$  and  $\text{HfB}_2$  can be obtained by aluminothermic reduction of oxides *via* mechanically induced self-sustained reaction [Ref?]. We have explored the possibility of using Mg as a reducing agent in SHS of a solid solution of  $\text{ZrB}_2$  and  $\text{HfB}_2$  from  $\text{ZrO}_2$ ,  $\text{HfO}_2$ , and  $\text{B}_2\text{O}_3$ . Figure 4.3.19 shows the XRD pattern of the combustion products for the mixture with  $\text{ZrO}_2:\text{HfO}_2:\text{B}_2\text{O}_3:\text{Mg}$  mole ratio of 0.5:0.5:1:6 milled for 5 min. It is seen that a solid solution of  $(\text{Zr}_{0.5}\text{Hf}_{0.5})\text{B}_2$  has been formed though it is overlapped with  $\text{ZrB}_2$ . Also, the XRD pattern shows the presence of  $\text{HfO}_2$  and  $\text{ZrO}_2$  impurities in the combustion products. It is expected that by making the mixture more exothermic, a full solid solution will form.

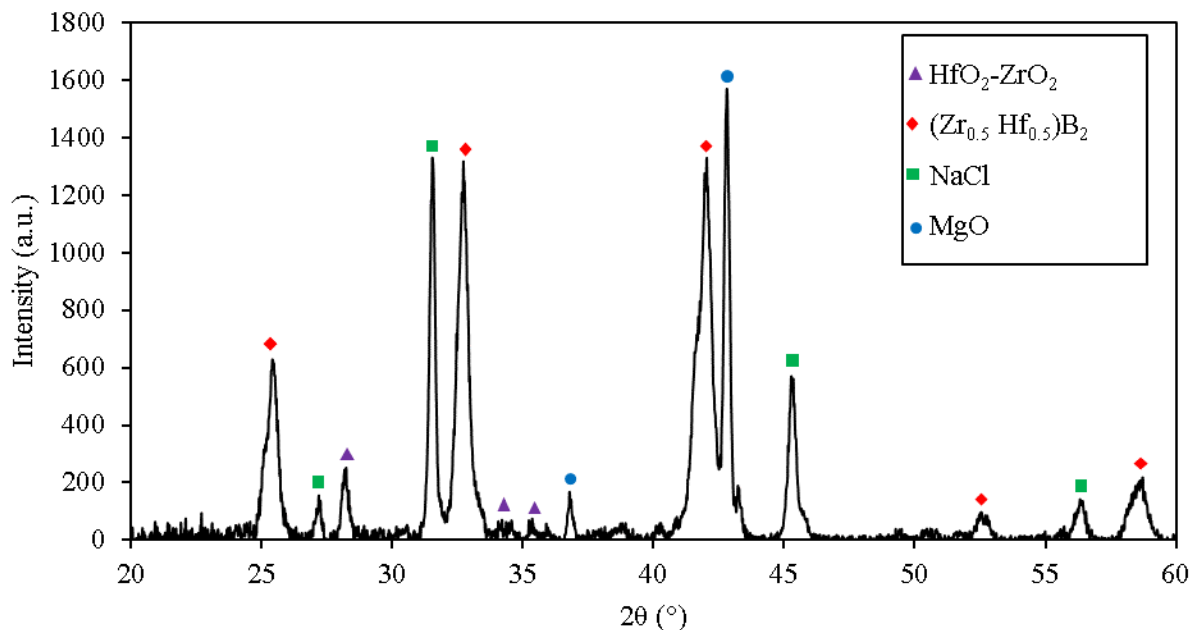


Figure 4.3.19: XRD pattern of  $\text{ZrO}_2/\text{HfO}_2/\text{B}_2\text{O}_3/\text{Mg}$  mixture with 30 wt% NaCl after combustion

#### 4.4. Reaction Mechanisms

Reaction mechanisms of stoichiometric  $\text{ZrO}_2\text{-B}_2\text{O}_3\text{-Mg}$  and  $\text{ZrO}_2\text{-B}_2\text{O}_3\text{-Mg-NaCl}$  mixtures before and after milling were studied using a differential scanning calorimeter (Netzsch DSC 404 F1 Pegasus) and a thermogravimetric analyzer (Netzsch TGA 209 F1 Iris). Figure 4.4.1 shows the DSC and TGA curves for the stoichiometric  $\text{ZrO}_2\text{-B}_2\text{O}_3\text{-Mg}$  mixture before milling. The DSC curve shows a small exothermic peak at 574 °C, then an endothermic peak at melting of Mg (650 °C), and finally an exothermic peak at 770 °C. The TGA curve shows a rapid mass loss of 18% of the sample mass. The mass loss is initiated by melting of Mg and stops at the start of the second exothermic peak. This result implies that mass loss is caused by vaporization of Mg.

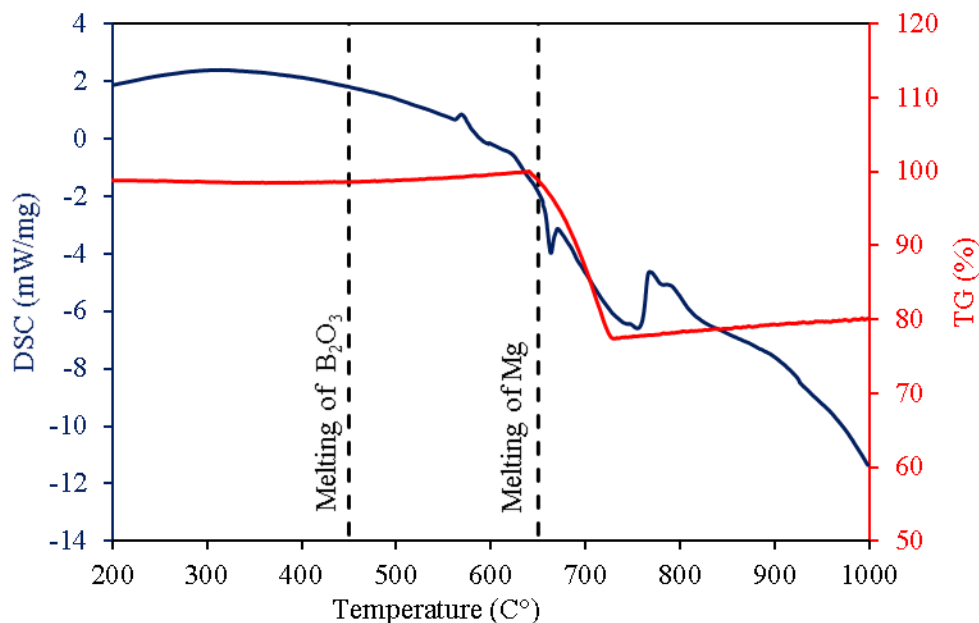


Figure 4.4.1: DSC and TG curves of stoichiometric  $\text{ZrO}_2\text{-B}_2\text{O}_3\text{-Mg}$ .

Figure 4.4.2 shows the DSC and TG curves of the milled mixture  $\text{ZrO}_2\text{-B}_2\text{O}_3\text{-Mg}$  with 45 wt% of NaCl. It is seen that the DSC curve has two exothermic and three endothermic peaks. Two relatively small endothermic peaks indicate melting of  $\text{B}_2\text{O}_3$  and Mg (450 °C and 650 °C, respectively). The first exothermic peak (470 °C) follows melting of  $\text{B}_2\text{O}_3$ , indicating that the first reaction is triggered by the melting of  $\text{B}_2\text{O}_3$ . Similarly, the second exothermic peak (670 °C) follows melting of Mg. A significant drop in the heat flow commences at temperatures close to the melting point of NaCl (801 °C). Also, the TGA curve shows a catastrophic mass loss that begins at around 800 °C. Apparently, the drop in heat flow and the mass loss were caused by the volatilization of liquid NaCl. This was confirmed by a TGA of NaCl.

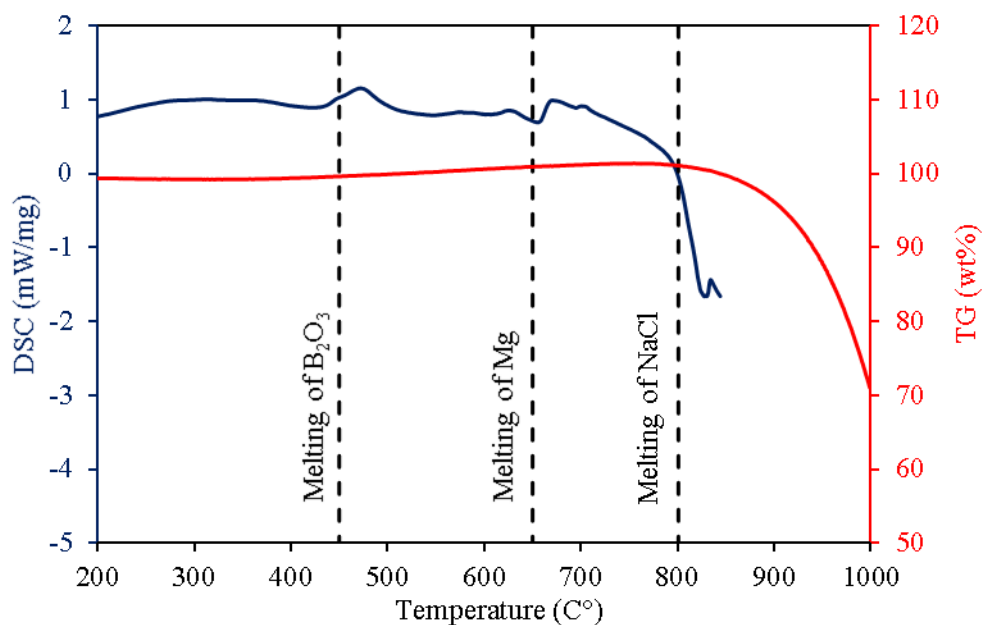


Figure 4.4.2: DSC and TG curves of stoichiometric  $\text{ZrO}_2\text{-B}_2\text{O}_3\text{-Mg}$  with 45 wt% NaCl.

To better understand the reaction mechanisms, Figure 4.4.3 shows the XRD patterns of samples at different stages of the DSC test of the mixture  $\text{ZrO}_2\text{-B}_2\text{O}_3\text{-Mg}$  with 45 wt% of NaCl. The test that was stopped at 550 °C shows a decrease in the content of Mg and a small peak of MgO, which confirms that the first exothermic peak in Fig. 4.4.2 is caused by the reaction between Mg and  $\text{B}_2\text{O}_3$ . The test stopped at 750 °C shows a larger conversion of Mg to MgO, with no visible change in the  $\text{ZrO}_2$  peak (located at  $2\theta = 28^\circ$ ) compared to the milled mixture pattern.  $\text{ZrB}_2$  phase appears in the test stopped at 1000 °C, accompanied by a decrease of  $\text{ZrO}_2$  peak, a decrease in NaCl peaks (due to NaCl vaporization), and the appearance of the undesirable phase  $\text{Mg}_3(\text{BO}_3)_2$ . From these observations, it can be concluded that Mg reacts with  $\text{ZrO}_2$  at higher temperatures than with  $\text{B}_2\text{O}_3$ . It is expected that higher temperatures than 1000 °C may be needed for a better conversion of  $\text{ZrO}_2$  to  $\text{ZrB}_2$ .



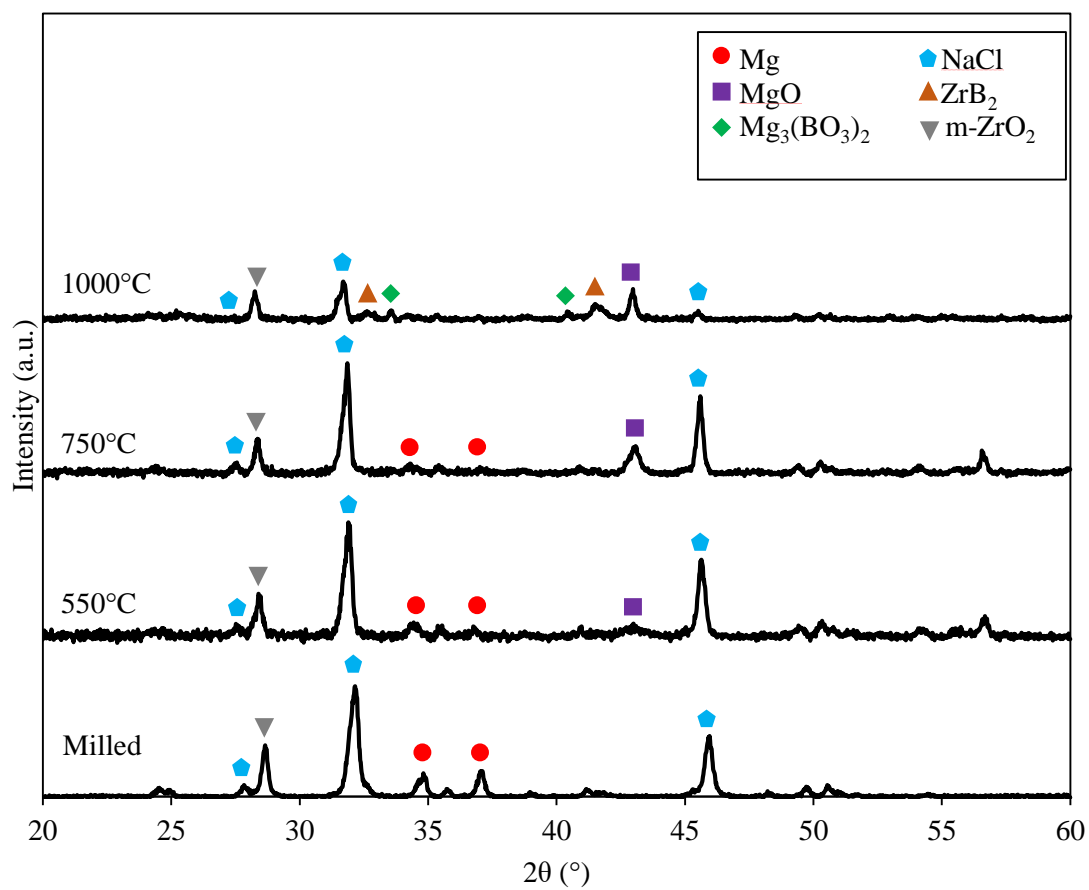


Figure 4.4.3: XRD patterns of the milled mixture and of the products obtained after quenching the DSC test of  $ZrO_2$ - $B_2O_3$ -Mg with 45 wt% of NaCl at different temperatures.

## Chapter 5: Conclusions

Thermodynamic calculations for combustion of  $\text{ZrO}_2/\text{B}_2\text{O}_3/\text{Mg}$  and  $\text{HfO}_2/\text{B}_2\text{O}_3/\text{Mg}$  mixtures revealed that at stoichiometry part of magnesium remains unreacted, but by lowering the combustion temperature full conversion can be achieved. To decrease the combustion temperature in the experiments, two inert diluents,  $\text{MgO}$  and  $\text{NaCl}$ , were used. The effects of the diluents on the high-energy ball milling process and on the particle size of the products were investigated.

After milling the stoichiometric  $\text{ZrO}_2/\text{B}_2\text{O}_3/\text{Mg}$  mixture (1:1:5, molar ratio), only 76% of the mixture was recovered from the grinding media. Conducting milling with  $\text{MgO}$  as an additive did not facilitate the milling process. However, by adding 10 wt%  $\text{NaCl}$  to the mixture, the amount of material lost during milling was decreased from 24% to 5%.

The XRD patterns of the combustion products of  $\text{ZrO}_2/\text{B}_2\text{O}_3/\text{Mg}$  mixtures showed that the main product is  $\text{ZrB}_2$ , but cubic  $\text{ZrO}_2$  (stabilized by  $\text{MgO}$ ) and  $\text{Mg}_3(\text{BO}_3)_2$  are present in the products. By adding excess  $\text{Mg}$  to the stoichiometric  $\text{ZrO}_2:\text{B}_2\text{O}_3:\text{Mg}$  mixture, the conversion of oxides to borides was significantly improved.

Contrary to the thermodynamic calculations, the addition of magnesium oxide to the initial mixture had an adverse effect to the conversion of oxides to borides; both cubic  $\text{ZrO}_2$  and monoclinic  $\text{ZrO}_2$  were found in the products. Their content increased with increasing  $\text{MgO}$  concentration in the initial mixture.

The effect of  $\text{NaCl}$  on the conversion degree was more complex. As  $\text{NaCl}$  content was increased in the initial mixture, the monoclinic  $\text{ZrO}_2$  content increased, but the cubic  $\text{ZrO}_2$  content decreased. This finding is explained by the temperature effect on the stability of these two phases, shown in the phase diagram of  $\text{MgO}-\text{ZrO}_2$  system. SEM images showed that the addition of  $\text{NaCl}$  decreased the particle size of the obtained products to the nanometric scale, which is expected to facilitate pressureless sintering.

Thermoanalytical (DSC and TGA) experiments revealed that the reaction of  $\text{ZrO}_2:\text{B}_2\text{O}_3:\text{Mg}$  mixtures is a multi-step process. For unmilled mixtures, an initial reaction occurs

at 571 °C and after melting, Mg starts to vaporize, triggering the second reaction at 770 °C. In the mixtures milled with NaCl, the first exothermic peak appeared at a lower temperature (470 °C), i.e. immediately after melting of B<sub>2</sub>O<sub>3</sub>, and the second exothermic peak (670 °C) appeared immediately after melting of Mg.

XRD analysis of samples obtained in DSC tests stopped at different temperatures further clarified the reaction mechanism for milled mixtures. Specifically, they confirmed that the first exothermic peak was caused by an initial reaction of Mg with molten B<sub>2</sub>O<sub>3</sub>, but this reaction stopped and then reinitiated after melting of Mg, leading to the second exothermic peak. They also revealed that the reaction of Mg with ZrO<sub>2</sub> and the subsequent formation of ZrB<sub>2</sub> occur at temperatures as high as 1000 °C.

After leaching MgO and NaCl from the products, XRD analysis showed that the content of m-ZrO<sub>2</sub> in the products increased though the content of c-ZrO<sub>2</sub> did not change. This effect was amplified with increasing NaCl content in the initial mixture. One explanation of the observed oxidation is that the smaller particle size of ZrB<sub>2</sub> obtained by combustion with a large concentration of NaCl increased the oxidation rate during leaching.

Experiments on magnesiothermic MASHS of HfB<sub>2</sub> and ZrB<sub>2</sub>-HfB<sub>2</sub> solid solution were also conducted. XRD showed that HfB<sub>2</sub> was obtained as the main phase with HfO<sub>2</sub> impurities. The solid solution of (Zr<sub>0.05</sub>Hf<sub>0.95</sub>)B<sub>2</sub> was produced, but single phase ZrB<sub>2</sub> was also found in the products.

In summary, borides of zirconium and hafnium have been obtained by magnesiothermic mechanical activation-assisted self-propagating high-temperature synthesis (MASHS) using oxides ZrO<sub>2</sub>, HfO<sub>2</sub>, and B<sub>2</sub>O<sub>3</sub> as the precursors though 100% conversion of oxides to borides was not achieved. It has been demonstrated that mechanical activation of ZrO<sub>2</sub>/B<sub>2</sub>O<sub>3</sub>/Mg and HfO<sub>2</sub>/B<sub>2</sub>O<sub>3</sub>/Mg mixtures decreases the ignition temperature and enables a self-sustained combustion. The addition of excess Mg increased the oxide-to-boride conversion degree. The use of NaCl additive was quite effective for reducing the loss of material during milling. Also, combustion of mixtures containing NaCl produced nanoscale particles of ZrB<sub>2</sub>, which may enhance pressureless sintering.

## References

- [1] R. J. Rosa, *Magnetohydrodynamic Energy Conversion*, New York, Ny: McGraw-Hill, 1968.
- [2] N. Kayukawa, "Open-Cycle Magnetohydrodynamic Electrical Power: a Review and Future Perspectives," *Progress in Energy and Combustion Science*, vol. 30, pp. 33-60, 2004.
- [3] G. Rudins, "U.S. and USSR MHD Electrode Materials Development," Rand, Santa Monica, Ca, 1974.
- [4] V. K. Rihatgi, "High Temperature Materials for Magnetohydrodynamic Channels," *Bulletin of Materials Science*, vol. 6, no. 1, pp. 71-82, 1984.
- [5] S. R. Levine, E. J. Opila, M. C. Halbig, J. D. Kiser, S. Mrityunjay and J. A. Salem, "Evaluation of Ultra-High Temperature Ceramics for Aeropropulsion Use," *Journal of the European Ceramic Society*, vol. 22, pp. 2757-2767, 2002.
- [6] M. Gasch, D. Ellerby, E. Irby, S. Beckman and M. Gusman, "Processing, Properties and Arc Jet Oxidation of Hafnium Diboride/Silicon Carbide Ultra High Temperature Ceramics," *Journal of Materials Science*, vol. 39, pp. 5925-5937, 2004.
- [7] M. M. Opeka, I. G. Talmy, E. J. Wuchina, J. A. Zaykoski and S. J. Causey, "Mechanical, Thermal, and Oxidation Properties of Refractory Hafnium and Zirconium Compounds," *Journal of the European Ceramic Society*, vol. 19, p. 2405, 1999.
- [8] W. G. Fahrenholtz and G. E. Hilmas, "Refractory Diborides of Zirconium and Hafnium," *Journal of the American Ceramic Society*, vol. 90, no. 5, pp. 1347-1364, 2007.
- [9] A. Delgado, S. Cordova and E. Shafirovich, "Thermite Reactions with Oxides of Iron and Silicon during Combustion of Magnesium with Lunar and Martian Regolith Simulants," *Combustion and Flame*, vol. 162, no. 9, pp. 3333-3340, 2015.
- [10] A. Delgado, S. Cordova, I. Lopez, D. Nemir and E. Shafirovich, "Mechanically Activated Combustion Synthesis and Shockwave Consolidation of Magnesium Silicide," *Journal of Alloys and Compounds*, vol. 658, pp. 422-429, 2016.
- [11] J. J. Moore and H. J. Feng, "Combustion of Advanced Materials: Part I. Reaction Parameters," *Progress on Materials Science*, vol. 39, pp. 243-273, 1995.
- [12] J. J. Moore and H. J. Feng, "Combustion Synthesis of Advanced Materials: Part II. Classification, Applications, and Modeling," *Progress on Materials Science*, vol. 39, pp. 275-316, 1995.
- [13] K. Morsi, "The Diversity of Combustion Synthesis Processing: a Review," *Journal of Materials Science*, vol. 47, pp. 68-92, 2012.
- [14] I. P. Borovinskaya, A. G. Merzhanov, N. P. Novikov and A. K. Filonenko, "Gasless Combustion of Mixtures of Powdered Transition Metals with Boron," *Fizika Goreniya i Vzryva*, vol. 10, no. 1, pp. 4-15, 1974.
- [15] H. E. Çamurlu and F. Maglia, "Preparation of Nano-Size ZrB<sub>2</sub> Powder by Self-Propagating High-Temperature Synthesis," *Journal of the European Ceramic Society*, vol. 29, pp. 1501-1506, 2009.
- [16] J. K. Sonber and A. K. Suri, "Synthesis and Consolidation of Zirconium Diboride: Review," *Advances in Applied Ceramics*, vol. 110, no. 6, pp. 321-334, 2011.

- [17] B. Akgün, E. H. Çamurlu, Y. Topkaya and N. Sevinç, "Mechanochemical and Volume Combustion Synthesis of ZrB<sub>2</sub>," *International Journal of Refractory Metals and Hard Materials*, vol. 29, pp. 601-607, 2011.
- [18] B. Akkas, M. Alkan, B. Derin and Yucel, "Effect of HCl Concentration on ZrB<sub>2</sub> Separation from a Self-Propagating High-Temperature Synthesis (SHS) Product," in *TMS (The Minerals, Metals & Materials Society)*, San Diego, 2011.
- [19] M. Jalaly, M. S. Bafghi, M. Tamizifar and F. J. Gotor, "An Investigation on the Formation Mechanism of Nano ZrB<sub>2</sub> Powder by a Magnesiothermic Reaction," *Journal of Alloys and Compounds*, vol. 588, pp. 36-41, 2014.
- [20] A. K. Khanra , L. C. Pathak and M. M. Godkhinhi, "Double SHS of ZrB<sub>2</sub> Powder," *Journal of Materials Processing Technology*, vol. 202, pp. 386-390, 2008.
- [21] M. A. Korchagin, T. F. Grigor'eva, B. B. Bokhonov, M. R. Sharafutdinov, A. P. Barinova and N. Z. Lyakhov, "Solid-State Combustion in Mechanically Activated SHS Systems. I. Effect of Activation Time on Process Parameters and Combustion Product Composition," *Combustion, Explosion, and Shock Waves*, vol. 39, no. 1, pp. 43-50, 2003.
- [22] D. P. Riley, E. H. Kisi and D. Phelan, "SHS of Ti<sub>3</sub>SiC<sub>2</sub>: Ignition Temperature Depression by Mechanical Activation," *Journal of the European Ceramic Society*, vol. 26, pp. 1051-1058, 2006.
- [23] F. J. Gotor, M. Achimovicova, C. Real and P. Balaz, "Influence of the Milling Parameters on the Mechanical Work Intensity in Planetary Mills," *Powder Technology*, vol. 233, pp. 1-7, 2013.
- [24] H. Pastor, "Metallic Borides: Preparation of Solid Bodies. Sintering Methods and Properties of Solid Bodies," *Boron and Refractory Borides*, pp. 457-493, 1977.
- [25] A. Balbo and D. Sciti, "Spark Plasma Sintering and Hot Pressing of ZrB<sub>2</sub>-MoSi<sub>2</sub> Ultra-High-Temperature Ceramics," *Materials Science and Engineering A*, vol. 475, pp. 108-112, 2008.
- [26] A. Rezaie, W. G. Fahrenholtz and G. E. Hilmas, "Effect of Hot Pressing Time and Temperature on the Microstructure and Mechanical Properties of ZrB<sub>2</sub>-SiC," *Journal of Materials Science* , vol. 42, pp. 2735-2744, 2007.
- [27] D. Sciti, F. Monteverde, S. Guicciardi, G. Pezzotti and A. Bellosi, "Microstructure and Mechanical Properties of ZrB<sub>2</sub>-MoSi<sub>2</sub> Ceramic Composites Produced by Different Sintering Techniques," *Materials Science and Engineering A*, vol. 434, pp. 303-309, 2006.
- [28] S. C. Zhang, G. E. Hilmas and W. G. Farenholtz, "Pressureless Sintering of ZrB<sub>2</sub>-SiC Ceramics," *Journal of the American Ceramic Society*, vol. 91, no. 1, pp. 26-32, 2008.
- [29] W. G. Fahrenholtz, G. E. Hilmas, S. C. Zhang and S. Zhu, "Pressureless Sintering of Zirconium Diboride: Particle Size and Additive Effects," *Journal of the American Ceramic Society*, vol. 91, no. 5, pp. 1398-1404, 2008.
- [30] L. Silvestroni and D. Sciti, "Effects of MoSi<sub>2</sub> Additions on the Properties of Hf- and Zr-B<sub>2</sub> Composites Produced by Pressureless Sintering," *Scripta Materialia* , vol. 57, pp. 165-168, 2007.
- [31] S. K. Mishra, S. K. Das, A. K. Ray and P. Ramachandrarao, "Effect of Fe and Cr Addition on the Sintering Behavior of ZrB<sub>2</sub> Produced by Self-Propagating High-Temperature Synthesis," *Journal of the American Ceramic Society*, vol. 85, no. 11, pp. 2846-2848, 2002.

- [32] S. C. Zhang, G. E. Hilmas and W. G. Fahrenholtz, "Pressureless Densification of Zirconium Diboride with Boron Carbide Additions," *Journal of the American Ceramic Society*, vol. 89, no. 5, pp. 1544-1550, 2006.
- [33] A. K. Khanra, L. C. Pathak, S. K. Mishra and M. M. Godkhindi, "Self-Propagating-High-Temperature Synthesis (SHS) of Ultrafine ZrB<sub>2</sub> Powder," *Journal of Materials Science Letters*, vol. 22, pp. 1189-1191, 2003.
- [34] A. K. Narayana Swamy and E. Shafirovich, "Conversion of Aluminum Foil to Powders that React and burn with Water," *Combustion and Flame*, vol. 161, pp. 322-331, 2014.
- [35] I. R. Shein and A. L. Ivanoskii, "Band Structure of ZrB<sub>2</sub>, VB<sub>2</sub>, NbB<sub>2</sub>, and TaB<sub>2</sub> Hexagonal Diborides: Comparison with Superconducting MgB<sub>2</sub>," *Physics of the Solid State*, vol. 44, no. 10, pp. 1833-1839, 2002.
- [36] M.-M. Zhong, X.-Y. Kuang, P. Shao and L.-P. Ding, "Phase Stability, Physical Properties, and Hardness of Transition Metal Diborides MB<sub>2</sub> (M = Tc, W, Re, and Os): First-Principles Investigations," *The Journal of Physical Chemistry*, vol. 117, pp. 10643-10652, 2013.
- [37] P. Vajeeston, P. Ravindran, C. Ravi and R. Asokamani, "Electronic Structure, Bonding, and Ground-State Properties of AlB<sub>2</sub>-Type Transition-Metal Diborides," *Physical Review B*, vol. 4, p. 045115, 2001.
- [38] G. P. Shveikin and A. L. Ivanovskii, "The Chemical Bonding and Electronic Properties of Metal Borides," *Russian Chemical Reviews*, vol. 63, no. 9, pp. 711-734, 1994.
- [39] J. K. Sonber, T. C. Murthy, C. Subramanian, S. Kumar, R. K. Fotedar and R. K. Suri, "Investigation on Synthesis of ZrB<sub>2</sub> and Development of New Composites with HfB<sub>2</sub> and TiSi<sub>2</sub>," *International Journal of Refractory Metals and Hard Materials*, vol. 29, pp. 21-30, 2011.
- [40] P. Millet and T. Hwang, "Preparation of TiB<sub>2</sub> and ZrB<sub>2</sub>. Influence of a Mechano-Chemical Treatment on the Borothermic Reduction of Titania and Zirconia," *Journal of Materials Science*, vol. 31, pp. 351-355, 1996.
- [41] S. K. Mishra, S. Das and L. C. Pathak, "Defect Structure in Zirconium Diboride Powder Prepared by Self-Propagating High-Temperature Synthesis," *Materials Science and Engineering*, vol. A364, pp. 249-255, 2004.
- [42] I. P. Borovinskaya, T. V. Barinova, V. I. Vershinnikov and T. I. Ignat'eva, "SHS of Ultrafine and Nanosized Refractory Powders: An Autoreview," *International Journal of Self-Propagating High-Temperature Synthesis*, vol. 19, no. 2, pp. 114-119, 2010.
- [43] M. Alkan, M. S. Sonmez, B. Derin and O. Yucel, "Effect of Initial Composition on Boron Carbide Production by SHS Process Followed by Acid Leaching," *Solid State Sciences*, vol. 14, pp. 1688-1691, 2012.
- [44] A. Hoseinpour, M. Jalaly, M. S. Bafghi, J. Vahdati Khaki and M. Sakaki, "The Effect of Preliminary Mechanical Activation on the Zinc Loss Control in Combustive Reaction of MoO<sub>3</sub> by Zn," *International Journal of Refractory Metals and Hard Materials*, vol. 54, pp. 251-259, 2016.
- [45] J. Guojian, X. Jiayue, Z. Hanrui and L. Wenlan, "Fabrication of B<sub>4</sub>C from Na<sub>2</sub>B<sub>4</sub>O<sub>7</sub> + Mg + C by SHS Method," *Ceramics International*, vol. 37, pp. 1689-1691, 2011.
- [46] J. Guojian, X. Jiayue, Z. Hanrui and L. Wenlan, "Combustion of Na<sub>2</sub>B<sub>4</sub>O<sub>7</sub> + Mg + C to Synthesis B<sub>4</sub>C Powders," *Journal of Nuclear Materials*, vol. 393, pp. 487-491, 2009.

- [47] M. Jalaly, M. Tamizifar, M. S. Bafghi and F. J. Gotor, "Mechanicochemical Synthesis of ZrB<sub>2</sub>-SiC-ZrC Nanocomposite Powder by Metallothermic Reduction of Zircon," *Journal of Alloys and Compounds*, vol. 581, pp. 782-787, 2013.
- [48] J. B. Abbasi, M. Zakeri and S. A. Tayebifard, "High Frequency Induction Heated Sintering of Nanostructures Al<sub>2</sub>O<sub>3</sub>-ZrB<sub>2</sub> Composited Produced by MASHS Technique," *Ceramic International*, vol. 40, pp. 9217-9224, 2014.
- [49] L. Deris, S. Sharafi and G. H. Akbari, "Effect of Milling Speed on Mechanical Activation of Al/ZrO<sub>2</sub>/H<sub>3</sub>BO<sub>3</sub> System to Prepare Al<sub>2</sub>O<sub>3</sub>-ZrB<sub>2</sub> Composite Powder," *Journal of Thermal Analysis and Calorimetry*, vol. 115, pp. 401-407, 2014.
- [50] M. J. Sayagués, M. A. Avilés, J. M. Córdoba and F. J. Gotor, "Self-Propagating Combustion Synthesis via an MSR Process: An Efficient and Simple Method to Prepare (Ti,Zr,Hf)B<sub>2</sub>-Al<sub>2</sub>O<sub>3</sub>) Powder Nanocomposites," *Powder Technology*, vol. 256, pp. 244-250, 2014.
- [51] N. Setoudeh and N. J. Welham, "Formation of Zirconium Diboride (ZrB<sub>2</sub>) by Room Temperature Mechanochemical Reaction Between ZrO<sub>2</sub>, B<sub>2</sub>O<sub>3</sub>, and Mg," *Journal of Alloys and Compounds*, vol. 420, pp. 225-228, 2006.
- [52] M. Jalaly, M. S. Bafghi, M. Tamizifar and F. J. Gotor, "The Role of Boron Oxide and Carbon Amounts in the Mechanochemical Synthesis of ZrB<sub>2</sub>-SiC-ZrC Nanocomposite via Self-Sustaining Reaction in the Zircon/Magnesium/Boron Oxide/Graphite System," *Journal of Alloys and Compounds*, vol. 598, pp. 113-119, 2014.
- [53] K. Nishiyama, T. Nakamura, S. Utsumi and H. Sakai, "Preparation of Ultrafine Borides Powders by Metallothermic Reduction Method," *Journal of Physics: Conference Series*, vol. 176, 2009.
- [54] A. K. Khanra, "Reaction Chemistry During Self-Propagating High-Temperature Synthesis (SHS) of H<sub>3</sub>BO<sub>3</sub>-ZrO<sub>2</sub>-Mg System," *Materials Research Bulletin*, vol. 42, pp. 2224-2229, 2007.
- [55] Y.-T. Zheng, H.-B. Li, Z.-H. Xu, J. Zhao and P. Yang, "Reaction Mechanism of Self-Propagating Magnesiothermic Reduction of ZrB<sub>2</sub> Powders," *Rare Metals*, vol. 32, no. 4, pp. 408-413, 2013.
- [56] P. Raschman and A. Fedorčková, "Study of Inhibiting Effect of Acid Concentration on the Dissolution Rate of Magnesium Oxide During the Leaching of Dead-Burned Magnesite," *Hydrometallurgy*, vol. 71, pp. 403-412, 2004.
- [57] S. Zhang, M. Khanghamano, H. Zhang and H. A. Yeprem, "Novel Synthesis of ZrB<sub>2</sub> Powder Via Molten-Salt-Mediated Magnesiothermic Reduction," *Journal of the American Ceramic Society*, vol. 97, no. 6, pp. 1686-1688, 2014.
- [58] A. A. Shiryaev, "Thermodynamics of SHS Process: Advanced Approach," *Journal of Physical and Chemical Reference*, vol. 14, no. 1, p. 1856, 1985.
- [59] R. R. Asamoto and P. E. Novak, "Tungsten-Rhenium Thermocouples for Use at High Temperatures," *Review of Scientific Instruments*, vol. 39, p. 1233, 1968.
- [60] C. F. Grain, "Phase Relations in the ZrO<sub>2</sub>-MgO System," *The Journal of the American Ceramic Society*, vol. 50, pp. 288-290, 1967.

- [61] A. K. Khanra, L. C. Pathak, S. K. Mishra and M. M. Godkhindi, "Sintering of Ultrafine Zirconium Diboride Powder Prepared by Modified SHS Technique," *Advances in Applied Ceramics*, vol. 104, no. 6, pp. 282-284, 2005.
- [62] A. L. Chamberlain, W. G. Fahrenholtz and G. E. Hilmas, "Pressureless Sintering of Zirconium Diboride," *Journal of the American Ceramic Society*, vol. 89, no. 2, pp. 450-456, 2006.
- [63] M. N. Rahaman, *Sintering of Ceramics*, Boca Raton, FL: Taylor & Francis Group, LLC, 2008.
- [64] E. B. Slamovich and F. F. Lange, "Densification Behaviour of Single-Crystal and Polycrystalline Spherical Particles of Zirconia," *Journal of the American Ceramic Society*, vol. 73, p. 3368, 1990.



## Vita

Sergio Cordova obtained his degree of Bachelor of Science in Mechanical Engineering from the University of Texas at El Paso in May 2015. He was enrolled in the Master's Program in Mechanical Engineering in July 2015.

In 2013, he formed a team and wrote a proposal to the NASA Microgravity Education Flight Program, which was selected. The team designed and built a magnetic device for cleaning spacesuits from lunar dust, which was tested onboard a reduced-gravity research aircraft in 2014.

As undergraduate, Sergio conducted research on the combustion of lunar and Martian regolith simulants with magnesium and on combustion synthesis of magnesium silicide. This work resulted in two peer-reviewed journal articles in *Combustion and Flame* and *Journal of Alloys and Compounds*. He also presented this work at the 5<sup>th</sup> Southwest Energy Science and Engineering Symposium and the 2015 Lunar Exploration Analysis Group Meeting.

At the beginning of his graduate studies, Sergio conducted research on the oxidation mechanisms of tin and iron powders. In October 2015, he started studying the magnesiothermic combustion synthesis of zirconium and hafnium diborides for the project sponsored by the National Energy Technology Laboratory of the U.S. Department of Energy. This research has been presented by Sergio at six conferences: 2016 and 2017 NETL Crosscutting Research Portfolios Review meetings, 2016 and 2017 Southwest Emerging Technology Symposia, Material Science and Technology 2016, and 10<sup>th</sup> U.S. National Combustion Meeting in April 2017. He will also present his results at the National Space & Missile Materials Symposium in June 2017.

Permanent address: 1701 N Piedras

El Paso, Texas, 79930

This thesis/dissertation was typed by the author.